DGR File
WVU College of Eng.
1978

FRACTURE MECHANICS INVESTIGATIONS ASSOCIATED WITH CORING AND HYDRAULIC INDUCED FRACTURES

Submitted by

S.H. Advani and H.V.S. GangaRao
Principal Investigators

College of Engineering
West Virginia University
Morgantown, West Virginia 26506

Prepared for

Morgantown Energy Technology Center
U.S. Department of Energy
Morgantown, West Virginia 26505

Under Contract No. EY-C-21-8087

UGR File #.25
WVU College of Eng.
1978

FOREWORD

This report describes the results from a study on fracture mechanics and stress response stimulations associated with coring and hydraulic induced fractures. The research was sponsored by the Morgantown Energy Technology Center (METC) under Contract No. EY-C-21-8087 and was performed in support of the Eastern Gas Shales Project. Mr. Charles A. Komar and Dr. Claude S. Dean served as Technical Monitors for METC.

The report is comprised of two parts. Part I deals with the hydraulic fracture modeling and characterization of the coupled formation structural and fracturing fluid flow responses. In Part II, elasticity theory and finite element model analysis of coring induced stresses and resulting fractures are presented along with an evaluation of possible *in situ* stress magnitudes.

This study was performed by the College of Engineering, West Virginia University, WV. Dr. Sunder H. Advani and Dr. Hota V. S. GangaRao served as Principal Investigators. Contributions to this program were made by H-Y Chang, S. Khan, P. Chang, and S. Lee.

WVU College of Eng.
1978

TABLE OF CONTENTS

Page

PART I HYDRAULIC FRACTURE MODELING FOR THE EASTERN GAS SHALES PROGRAM 1- 1

ABSTRACT 1- 1

1.0 INTRODUCTION 1- 2

2.0 HYDRAULIC FRACTURE MODEL SIMULATIONS 1- 3

2.1 STRUCTURAL MODEL SIMULATIONS 1- 3

2.2 FRACTURING FLUID RESPONSE SIMULATIONS 1- 9

2.2.1 One Dimensional Flow Model Simulation 1-13
2.2.2 Two Dimensional Flow Model Simulation 1-22

2.3 FOAM FRACTURE MODELING 1-24

3.0 DESIGN APPLICATIONS 1-30

4.0 DISCUSSION AND CONCLUSIONS 1-33

5.0 REFERENCES 1-34

APPENDIX A 1-36

PART II IN-SITU STRESS DETERMINATION BASED ON FRACTURE RESPONSE ASSOCIATED WITH CORING OPERATIONS 2- 1

1.0 INTRODUCTION 2- 3

2.0 IN-SITU STRESS DETERMINATION BASED ON THEORIES OF ELASTICITY AND FRACTURE 2- 6

2.1 STRESS ANALYSIS OF CORES UNDER DIFFERENT LOADS 2- 6

2.1.1 Drill Bit Loading 2- 6
2.1.2 Foam Pressure 2- 6
2.1.3 Overburden Pressure 2- 7
2.1.4 Tectonic Stresses 2- 7
2.1.5 Resultant State of Stress 2- 8
2.1.6 Effect of Pore Pressure 2-10

2.2 CORING-INDUCED FRACTURES 2-11

2.2.1 Fracture Angle Measurements 2-11
2.2.2 Fracture Extension 2-14
2.2.3 Idealization of Fracture Patterns 2-17

UGR File #125
WVU College of Eng.
1978

TABLE OF CONTENTS (Continued)

Page

3.0 IN-SITU STRESS DETERMINATION BASED ON FINITE ELEMENT METHODS AND FRACTURE THEORY 2-18

3.1 FINITE ELEMENT MODELING 2-18

3.2 DETERMINATION OF INITIAL FRACTURE ANGLE 2-26

3.3 DETERMINATION OF PROPAGATION ANGLE 2-33

4.0 DISCUSSION 2-35

4.1 IN-SITU STRESSES BASED ON ELASTIC ANALYSIS 2-35

4.2 IN-SITU STRESSES BASED ON FINITE ELEMENT METHODS 2-43

4.2.1 Effect of Different Loadings on In-Situ Stresses . . 2-43
4.2.2 First Stage Failure 2-45
4.2.3 Second Stage Failure 2-46

5.0 CONCLUSIONS AND RECOMMENDATIONS 2-46

5.1 CONCLUSIONS 2-47

5.2 RECOMMENDATIONS 2-49

6.0 REFERENCES 2-50

APPENDIX A 2-52

APPENDIX B 2-62

WVU College of Eng.
1978

PART I

HYDRAULIC FRACTURE MODELING FOR THE EASTERN GAS SHALES PROGRAM

By

S. H. Advani, H.V.S. GangaRao and H-Y Chang

College of Engineering
West Virginia University
Morgantown, WV 26506

PART I

HYDRAULIC FRACTURE MODELING FOR THE EASTERN GAS SHALES PROGRAM

ABSTRACT

Results from a Morgantown Energy Technology Center research contract on the simulation of hydraulic fracture models are presented. These models include the characterization of the coupled formation structural and fracturing fluid flow responses. The structural model is represented by layered linear elastic media subjected to *in situ* stress fields and fluid pressure on the vertical crack surface. The flow model includes the effects of flow rate, pumping pressure, fluid viscosity, fluid compressibility and formation reservoir properties.

Predictive results for the estimation of the fracture width and area for selected Devonian shale formation properties and hydraulic fracturing treatment parameters are illustrated. In addition, design considerations related to penetration of cracks across layered media, bottom hole treatment pressure control, *in situ* stress effects, fluid leak-offs in the formation, and foam fracturing are discussed.

1.0 INTRODUCTION

With the rapid dwindling of the gas resources in the United States coupled with an increased demand and potentially higher well head prices, the Department of Energy has initiated several research and development programs for tapping unconventional gas reservoirs. As an integral part of these programs, the Eastern Gas Shales Project (EGSP) is currently investigating methods for stimulating increased gas production from the Eastern Petroliferous basins. Innovative stimulation techniques for the EGSP, based on resource evaluations and geological considerations, are being designed with specific design objectives [1,2]. The advanced fracture treatments include MHF-Foam, MHF-Water, MHF-Foam/Water, Dendriditic, Foam, Explosive, and Cryogenic stimulations [3]. The supplementary predictive mathematical modeling studies provide a rational basis for site selection, treatment design, and well production flow characteristics.

The earliest rigorous effort on hydraulic fracture modeling is due to Zheltov and Khristianovitch [4]. Subsequent models by Haimson and Fairhurst [5,6], Geertsma and de Klerk [7], Daneshy [8,9], Shuck and Advani [10], and Simonsen, et al. [11] have addressed specific aspects such as fracture initiation, in situ and induced stress responses, fracture width determination, and effects of layering. This report presents results obtained from the simulation of comprehensive structural and fracturing fluid models which are coupled by the crack surface pressure. Fracture width and area estimates for prescribed Devonian Shale formation properties and hydraulic fracture treatment parameters are illustrated. Also, design considerations pertaining to fracture containment and optimum selection of stimulation variables are discussed.

2.0 HYDRAULIC FRACTURE MODEL SIMULATIONS

Results from the multi-layered finite element structural and finite difference fluid flow simulations conducted for the EGSP are described in this section. The basic hydraulic fracture model idealizations are also given.

2.1 STRUCTURAL MODEL SIMULATIONS

Computed stress responses for various two and three dimensional models representing the fluid induced crack extension in a hydraulic fracturing process have been presented by Shuck and Advani [10]. Corresponding finite element simulations and experimental work have been detailed in previous work [10, 12, 13] performed under contract with Sandia laboratories. For example, field stress simulations and crack intensity factors for the crack model illustrated in Figure 1 have been previously reported [13]. Figure 2 illustrates the layered plane strain model idealization of the formation with the vertical hydraulic fracture in the pay zone. Each layer is assumed to be linear, elastic, homogeneous, isotropic and perfectly bonded at the interface, i.e., appropriate displacement and traction continuity is assumed. For fracture propagation in the adjacent barrier layers subjected to different in situ stresses, the basic superposition concept for finite element analysis is illustrated in Figure 3. Figures 4a, b, c reveal the non-dimensionalized average half widths for different crack penetrations pertaining to crack width estimation in terms of the fracture geometry forcing fluid parameters, and formation modulus are presented in the text. The crack width computations will be utilized for fracture extent determinations.

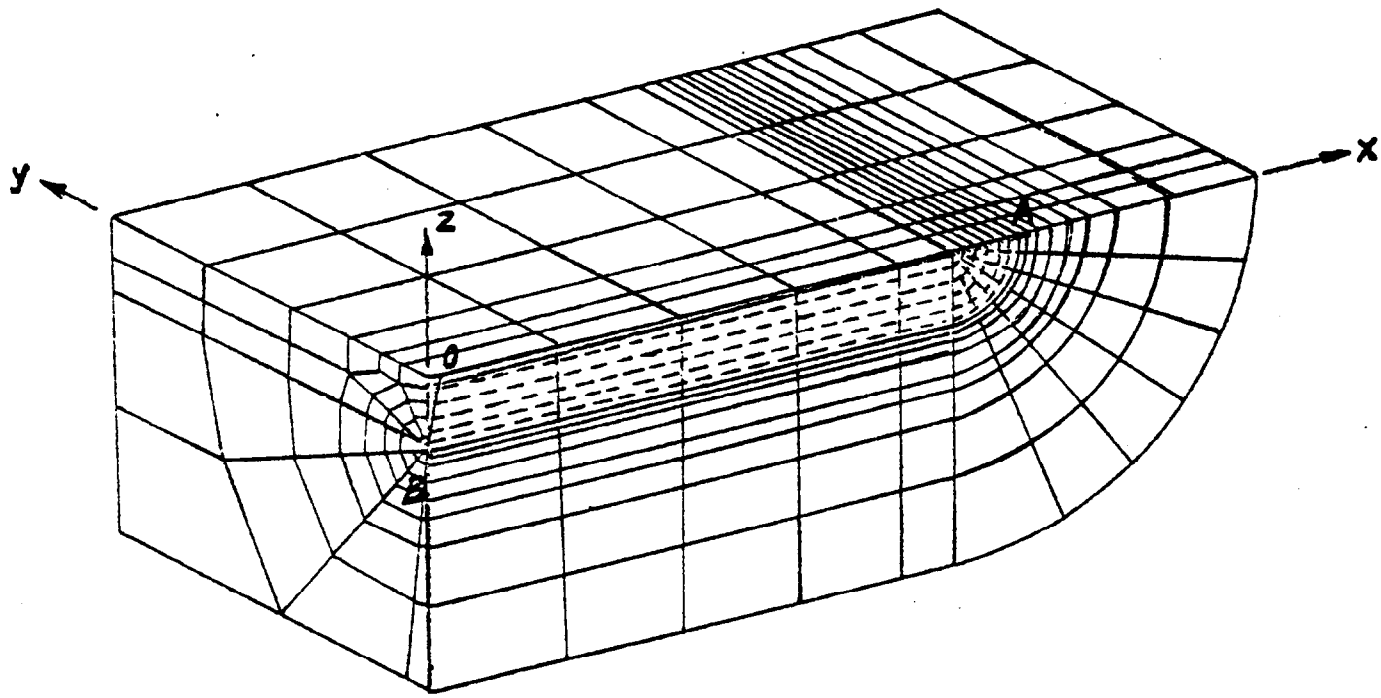

Figure 1. Three-dimensional Finite Element Crack Model

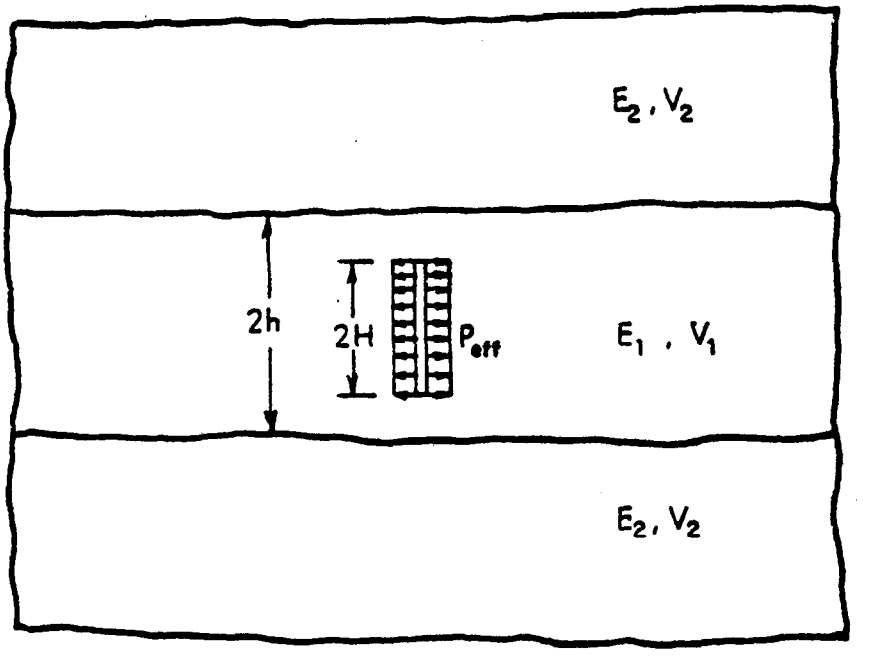

Figure 2. Layered Plane Strain Model Idealization

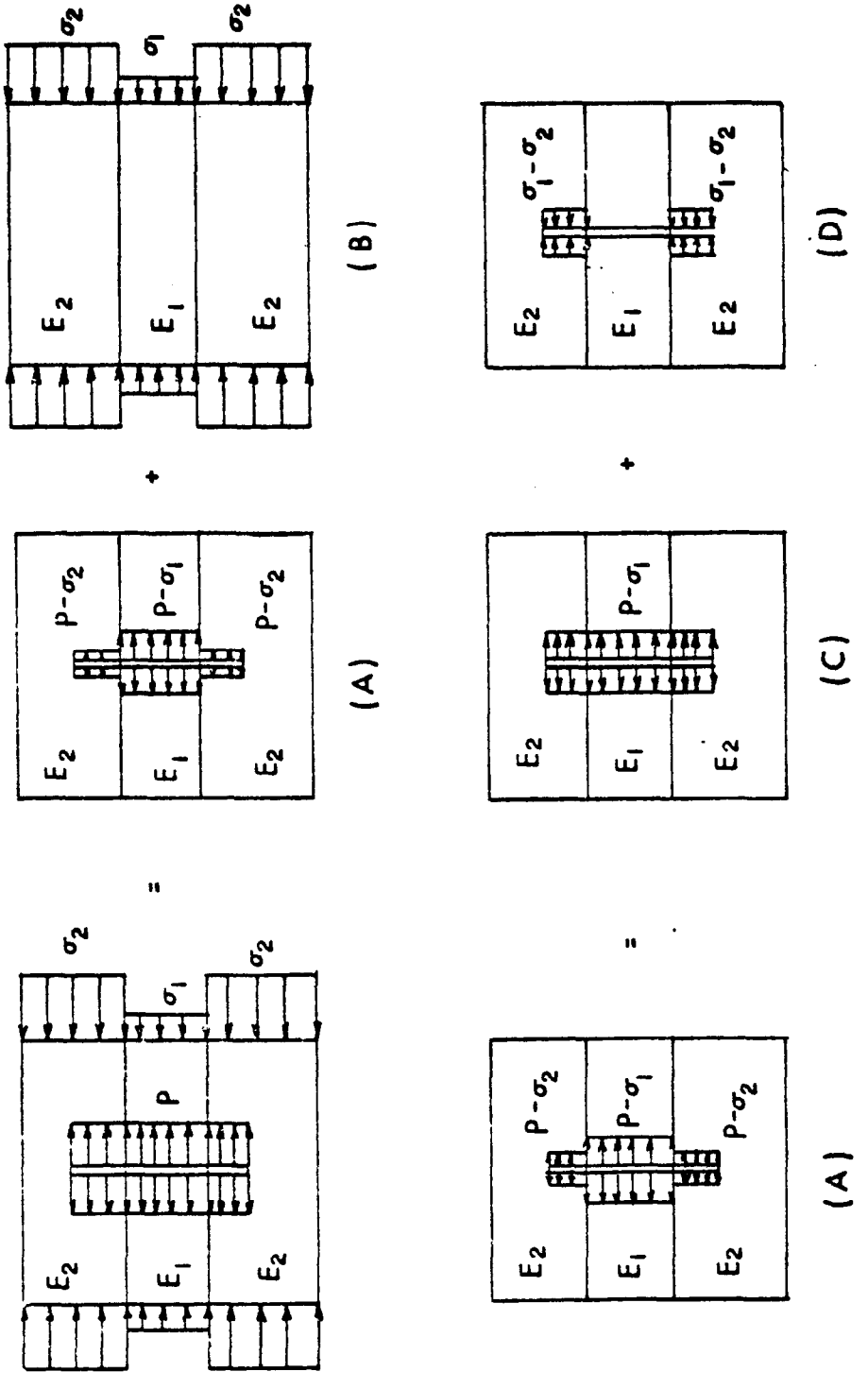

Figure 3. Superposition Concepts Relating to the Internal Pressure and Horizontal Minimum In-Situ Stresses

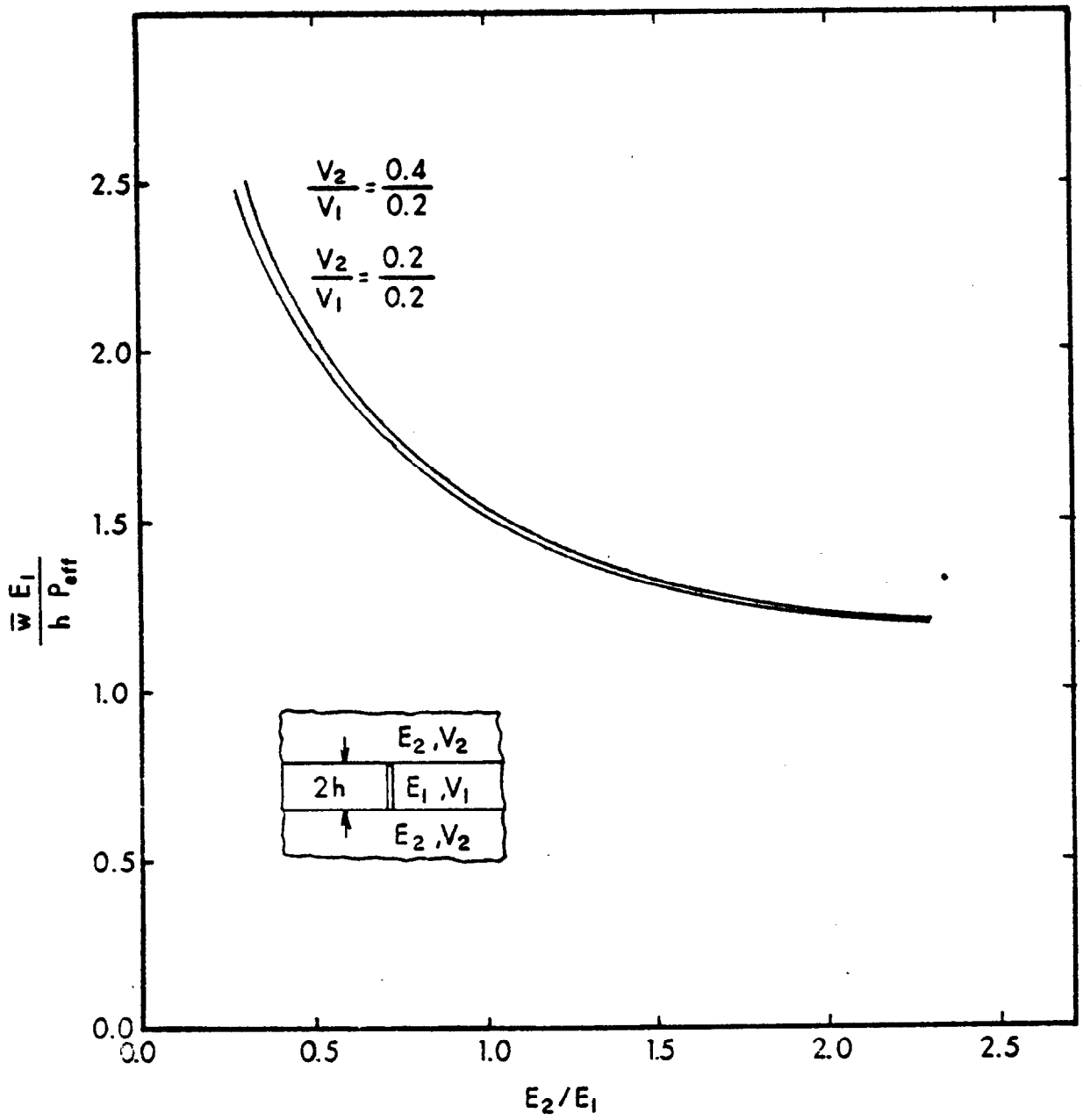

Figure 4a. Average Half Fracture Widths for Different Stratigraphic Distributions

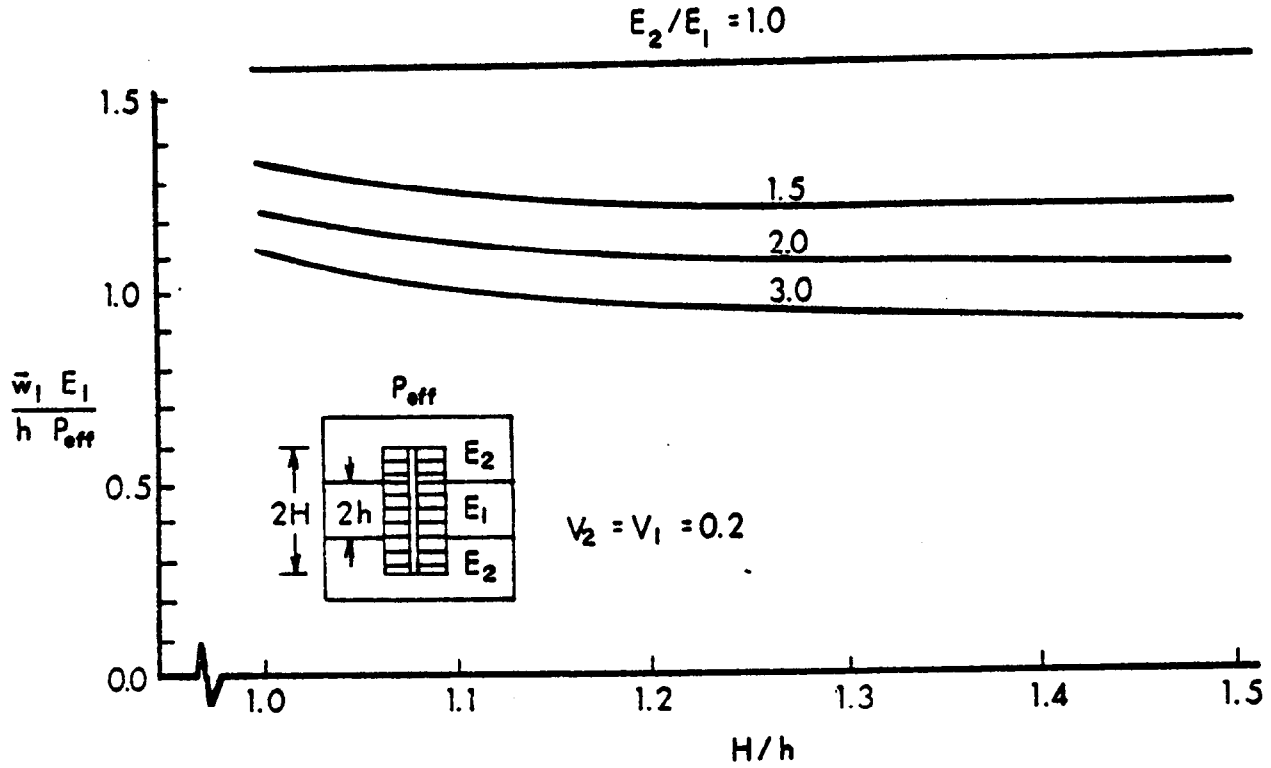

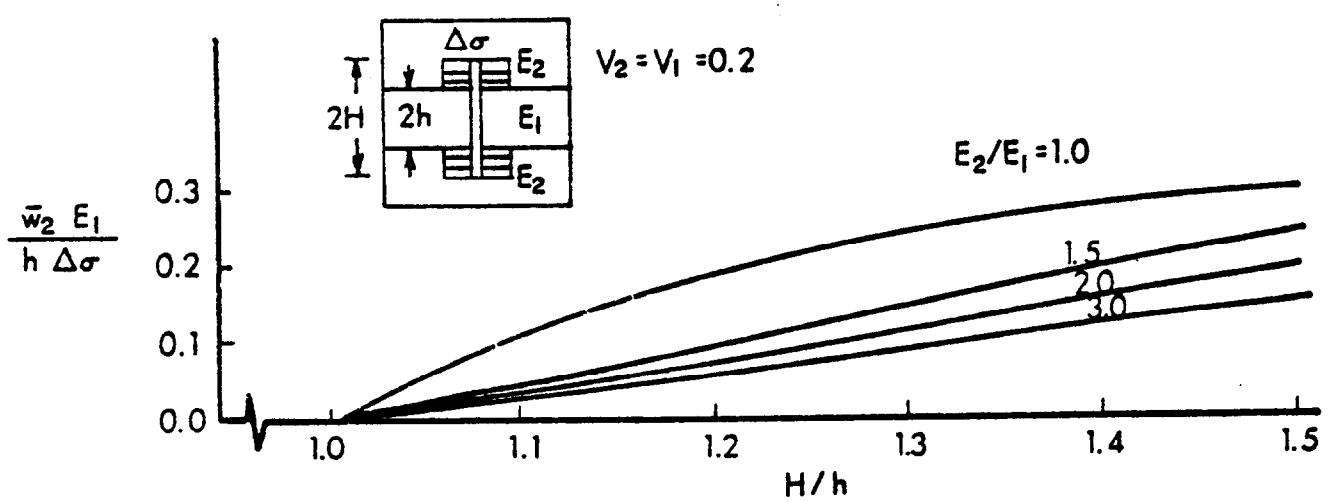

Figures 4b & 4c. Average Half Fracture Width as a Function of $\Delta\sigma$, E_2/E_1 Ratio and Fracture Containment H/h

To investigate the crack interface penetration characteristics, the associated through opening model stress intensity factor k_1 is examined during vertical fracture propagation. The containment of the fracture in the pay zone is primarily influenced by the elastic modulus ratio of the pay zone and barrier formation, the existing in situ stresses, the fracture toughness constants of the layers, and the effective bottom hole treatment pressure. The calculated nondimensional stress intensity factor variation, using a finite model representation [14], as a function of fracture height and elastic modulus ratio is illustrated in Figures 5a and b for the chosen loadings. It is noteworthy that when a/h approaches the limiting value of 1 (i.e., the interface), the "stress intensity factor" increases or decreases rapidly depending on the ratio of E_2/E_1. These finite element solutions have been validated using the integral formulation of Erdogen and Gupta [15]. However, the conventional definition of stress intensity factor no longer applies for the case of the crack approaching the interface since the stress singularity is governed r^{-w} with $w \neq 1/2$. The nondimensionalized stress intensity plots with specified bottom hole treatment pressures, layer in situ stresses, material moduli and fracture toughness values will be used for evaluating the vertical fracture height. Figure 6 illustrates a typical design curve for the case $E_2/E_1 = 1.5$ and different values of formation in situ stresses. The applicability of these results will be discussed in a subsequent section.

2.2 FRACTURING FLUID RESPONSE SIMULATIONS

The problems associated with modeling of the fracturing fluid flow behavior entail (i) determination of the pressure profile in the vertical crack, (ii) computation of flow velocities in the crack, formation, and fluid leakoffs, (iii) evaluation of fracture geometry, and (iv) development

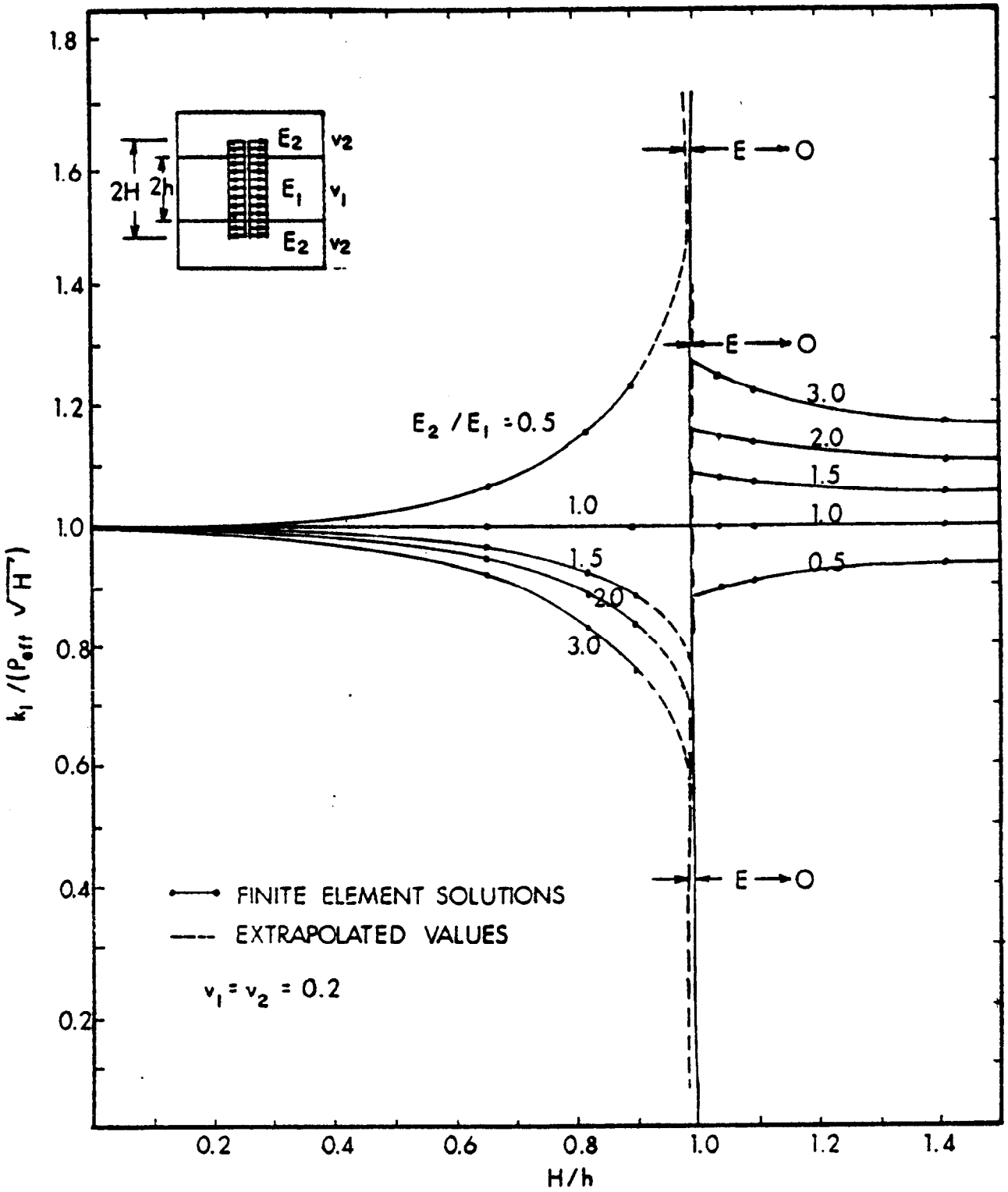

Figure 5a. Variation in the Stress Intensity Factor K_1 as a Function of Fracture Containment H/h and Layering Condition E_2/E_1

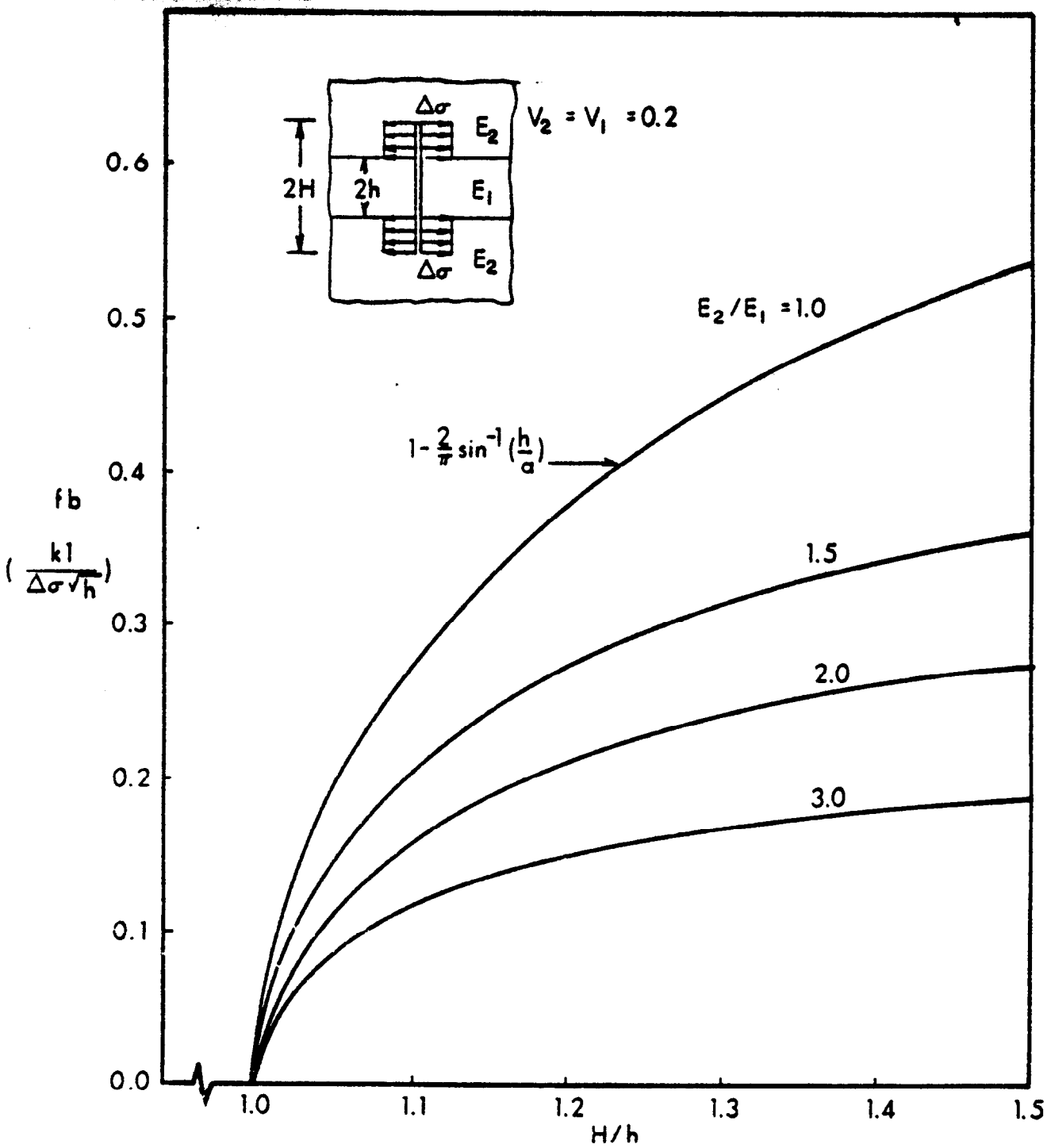

Figure 5b. Variation in the Stress Intensity Factor K_1 as a Function of Fracture Containment H/h and Layering Condition E_2/E_1

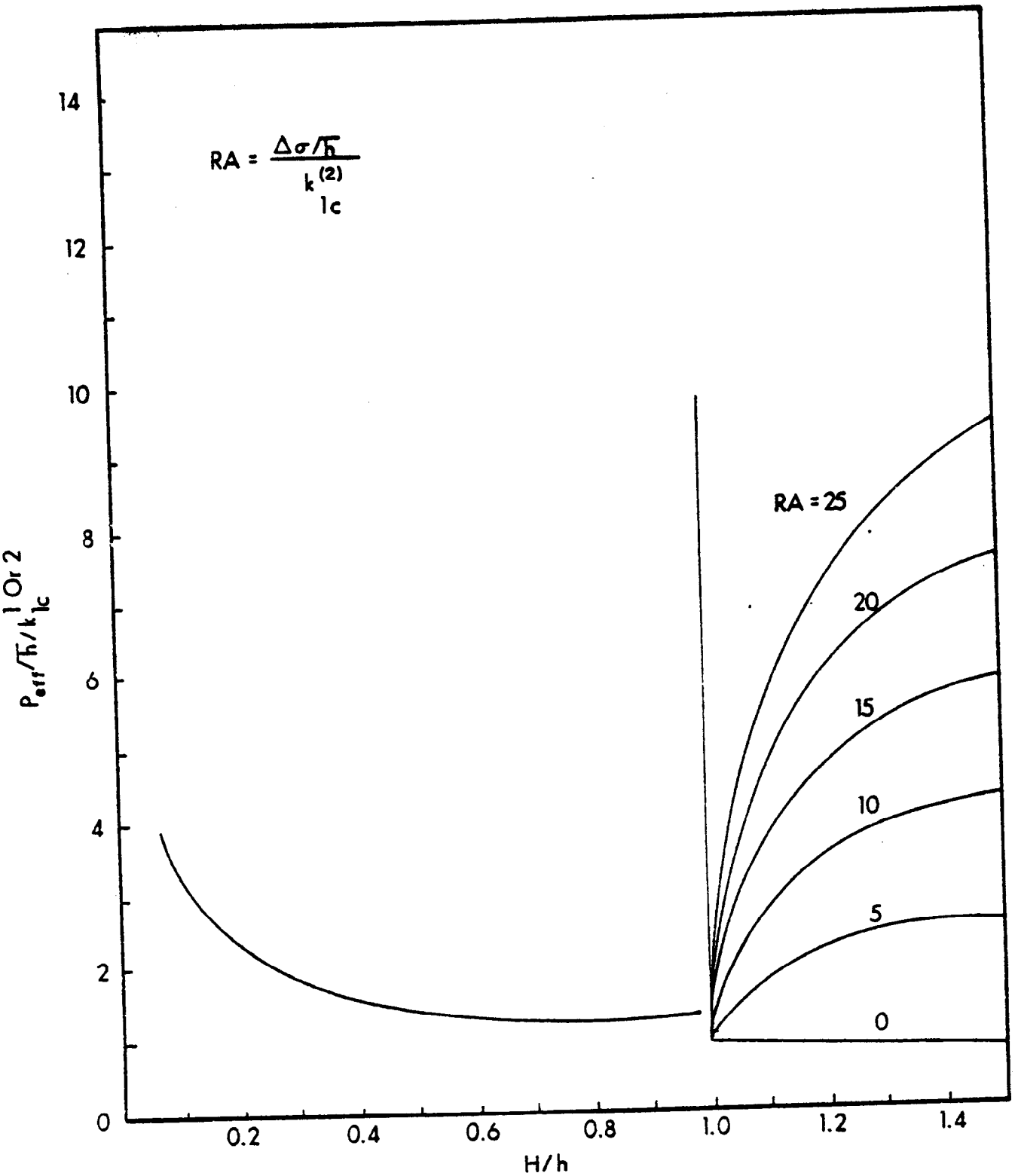

Figure 6. Allowable Effective Treatment Pressure P_{eff} versus Fracture Containment H/h for $E_2/E_1 = 2.0$

of guidelines for the optimization of fluid properties for maximizing fracture volume in the pay zone. Computations of flow velocity and fracture extent, based on a simplified one dimensional model, have been conducted by Carter [16]. Several design charts based on this analysis are detailed by Howard and Fast [17] and Halliburton Services Co. [18]. No effort to couple the structural response parameters is, however, made in these monographs.

Two time dependent flow model simulations are employed here. These two distinctly different models relate to the (i) one dimensional and (ii) two dimensional flow simulations in the crack and porous/permeable formation. The model parameters associated with the fluid response analysis are defined by: pay zone thickness (2h), fracture height (2H), average fracture width (2w), bottom hole treatment pressure (P), formation pore pressure (p_o), injection flow rate (Q), fracture cross sectional area (A), formation porosity (ϕ), formation permeabilities to fracturing fluids (k_x,k_y) fracturing fluid viscosity (μ), and effective fluid compressibility (c). The following subsections describe the investigated fluid flow models, associated assumptions, and related results.

2.2.1 <u>One Dimensional Flow Model Simulation</u>: The assumptions relating to this model include the applicability of Darcy's flow equation for the formation and Bernoulli's equation with appropriate viscous friction losses (governed by Reynolds number) in the vertical fracture. The formation pore pressure, pumping pressure, and fluid injection rate are selected to be constant. Two basic conditions, namely the conservation of mass and the no backflow condition are applied in the finite difference formulations. Detailed equations and computer programs for the relationships between fluid pressure, flow rate, leak-off rate, and other parameters are given

by Chang [14]. The iterative time step computations initially involve the determination of the total time duration for which each specified point on the fracture surface is exposed to the fracturing fluid with the cumulative leak-off effects included. Both incompressible and compressible fluids are modeled.

The predicted half fracture length-time curves for several different values of the above parameters have been evaluated. Figures 7a, b, and c reveal the computed fracture areas, for various flow indices FI, as a function of the flow rate Q and the injection time t for fracture widths of 0.2, 0.4, and 0.6 inch respectively. Relative fracture areas for scaling to different fracture widths are illustrated in Figure 8. For specific reservoir conditions (K, ϕ, and p_o) and treatment parameter values (μ, c, P, and Q), the flow index FI or loss coefficient is calculated from

$$FI = 0.00001913 \quad (k\ \phi\ \Delta P)/\mu \quad (ft/\ sec) \text{ for incompressible fluids}$$

and

$$FI = 0.00001526 \quad (k\ \phi\ c/\mu) \quad \Delta P(ft/\ sec) \text{ for compressible fluids}$$

where k is expressed in millidarcies, ϕ is the percentage porosity, μ is in centipoise units, c is the reciprocal of the bulk modulus (1/psi) and ΔP is in psi.

Following specification of the flow index, the fracture area corresponding to the prescribed injection rate and elapsed time can be obtained from Figures 7. The leak-off ratios as a function of the flow index and fracture width are shown in Figures 9a, b, and c. Design examples based on the results in Figures 7 through 9 are provided in the section on Applications. It should be emphasized that this simulation provides preliminary guidelines for obtaining fracture areas with fracture widths and constant vertical heights computed from the preceding structural

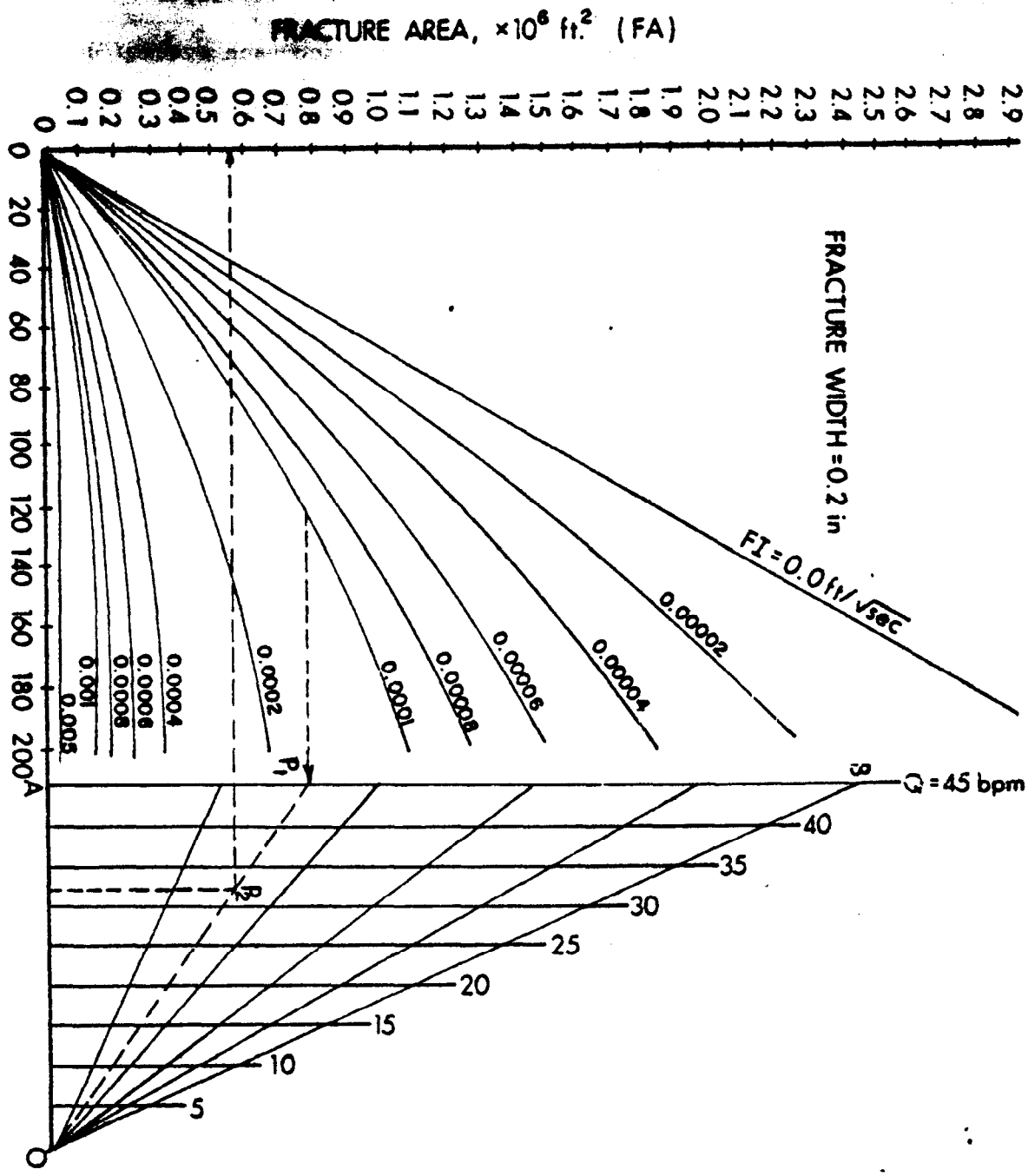

Figure 7a. Computed Fracture Area versus Treatment Time Plots for Different Flow Rates and Flow Indices

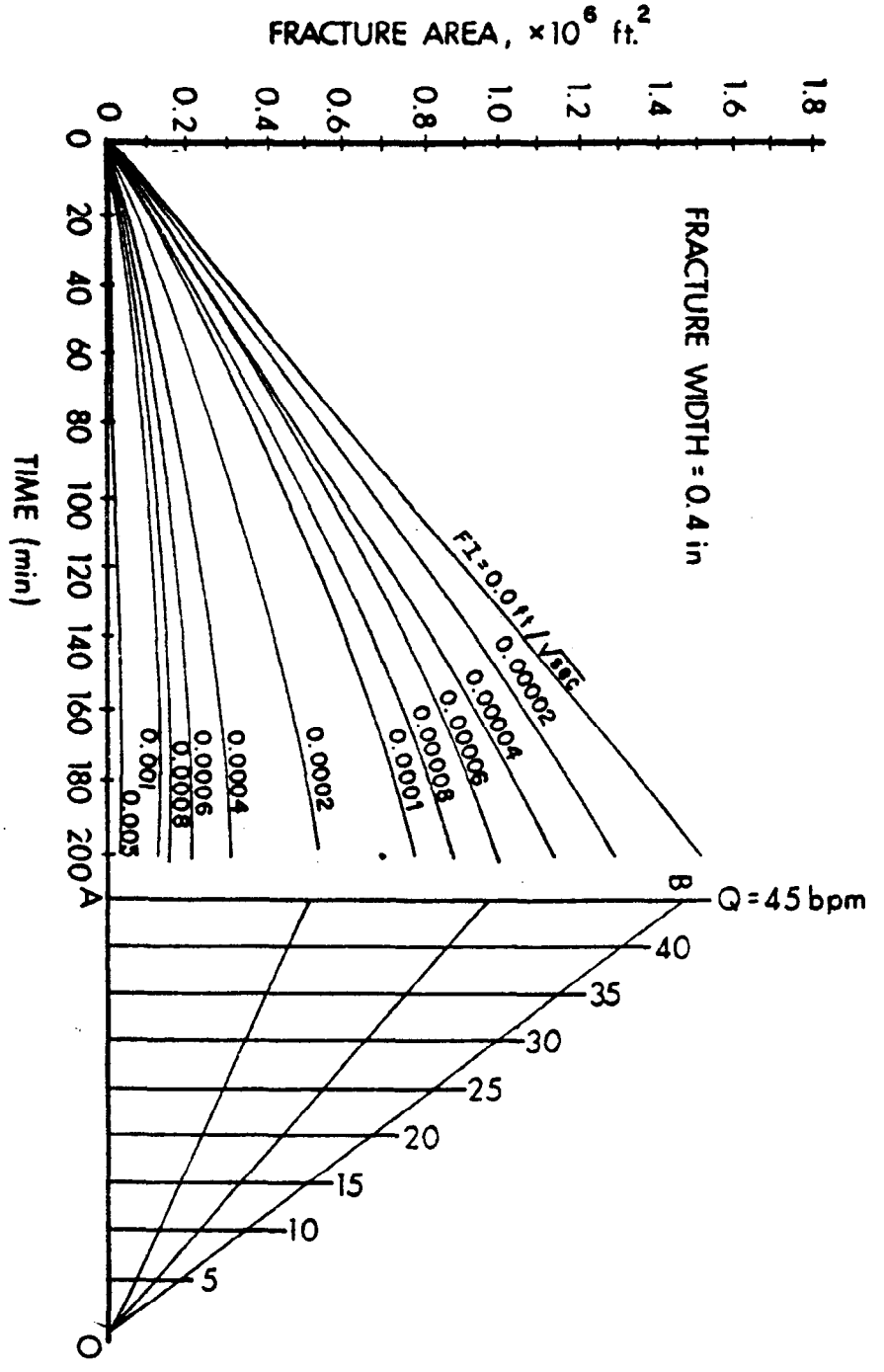

Figure 7b. Computed Fracture Area versus Treatment Time Plots for Different Flow Rates and Flow Indices

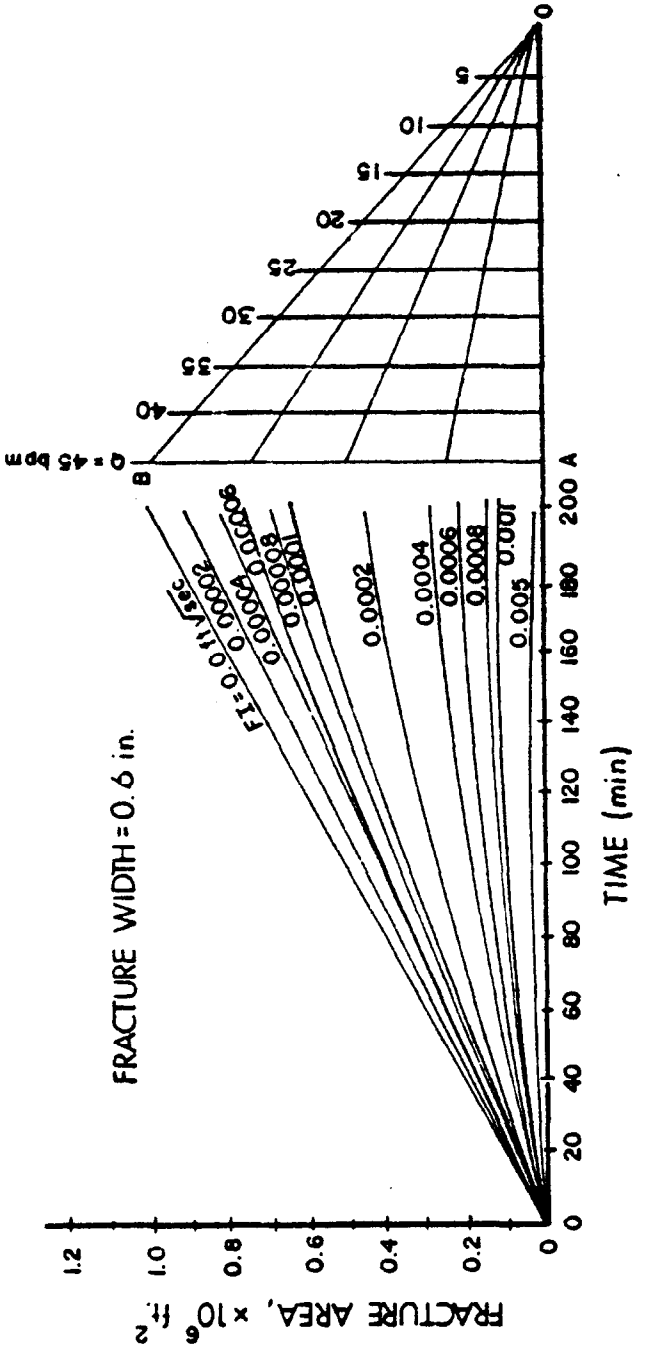

Figure 7c. Computed Fracture Area versus Treatment Time Plots for Different Flow Rates and Flow Indices

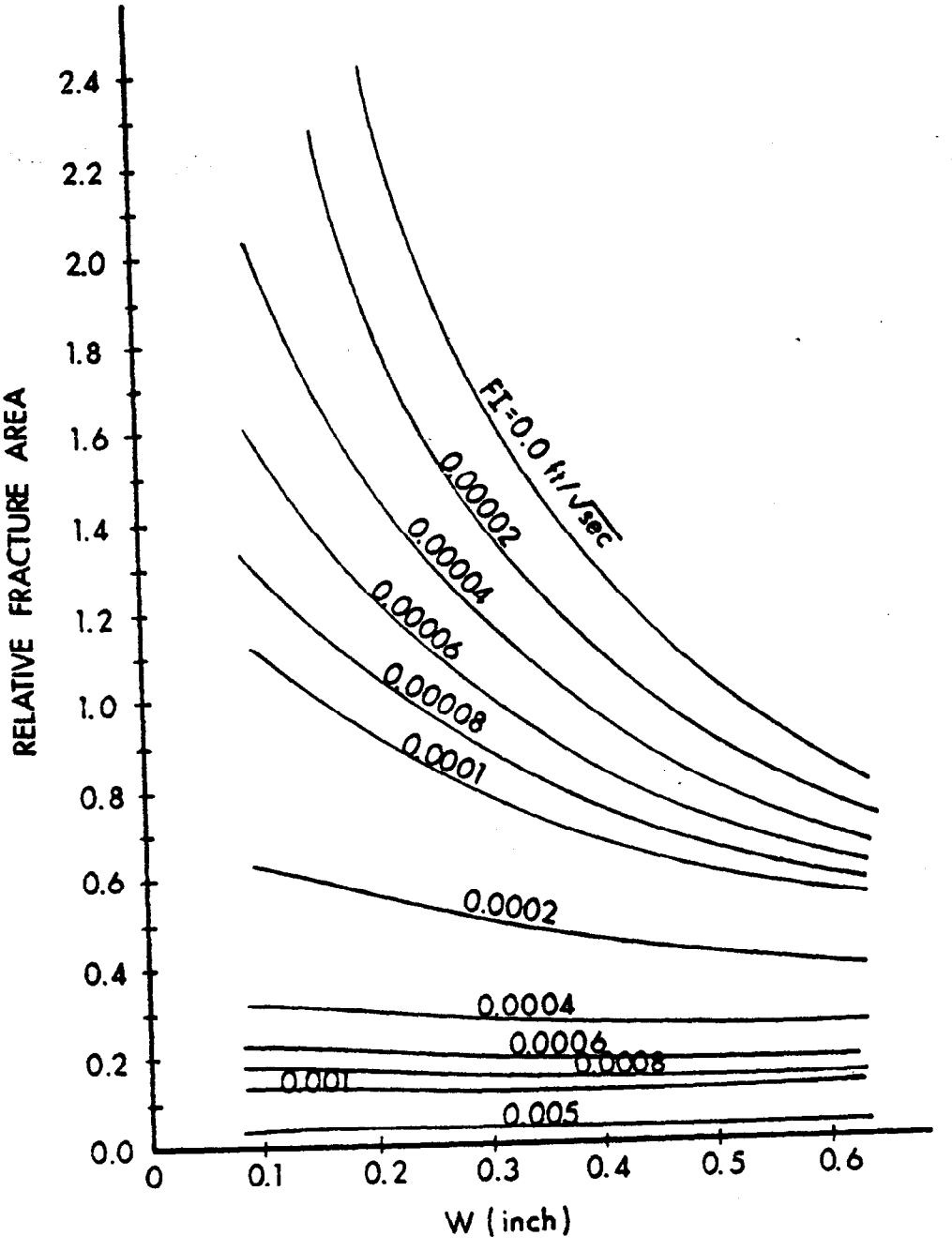

Figure 8. Fracture Area versus Width Scaling Plots for Different Flow Indices

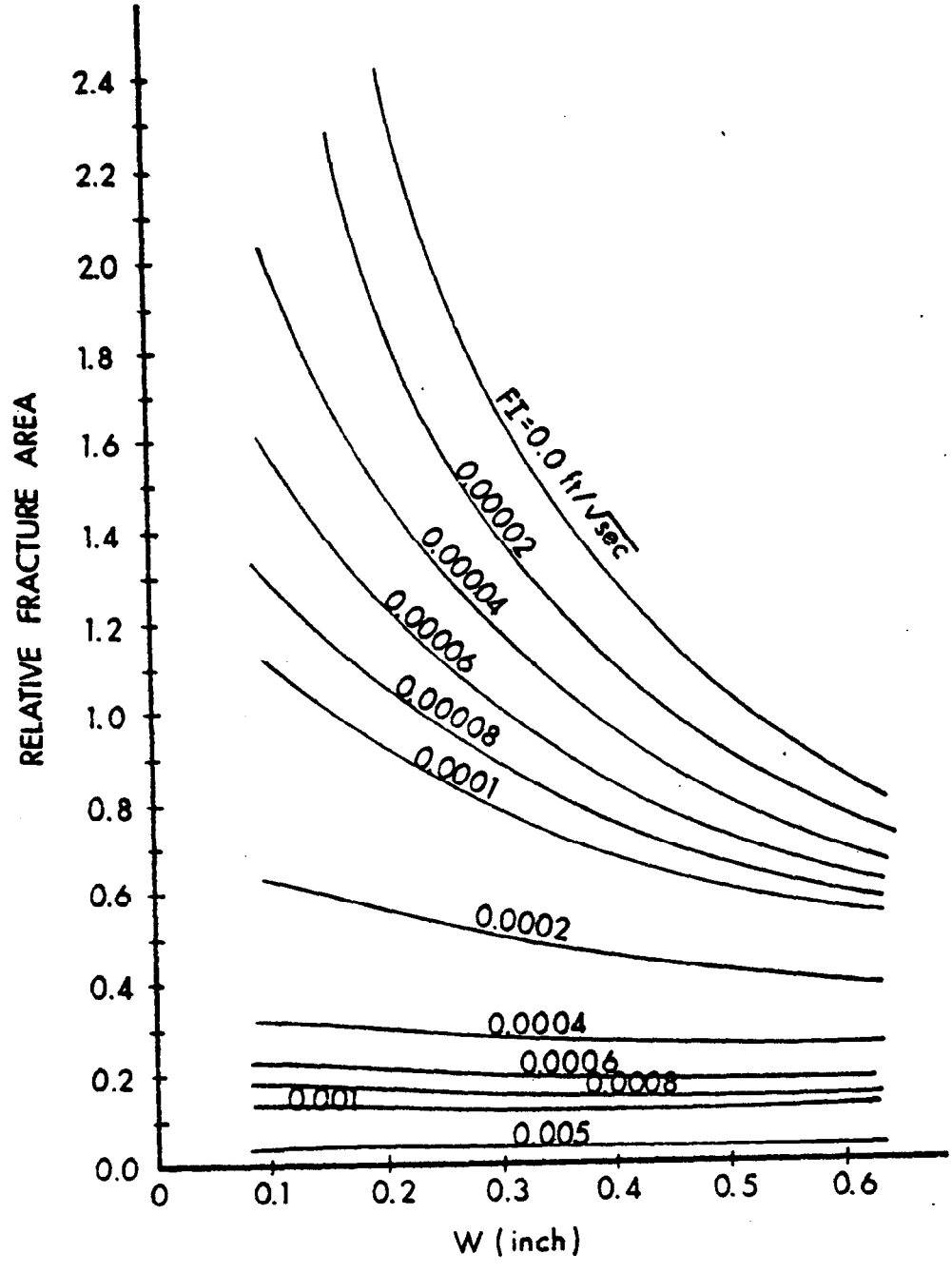

Figure 8. Fracture Area versus Width Scaling Plots for Different Flow Indices

Fracture Width = 0.2 in.

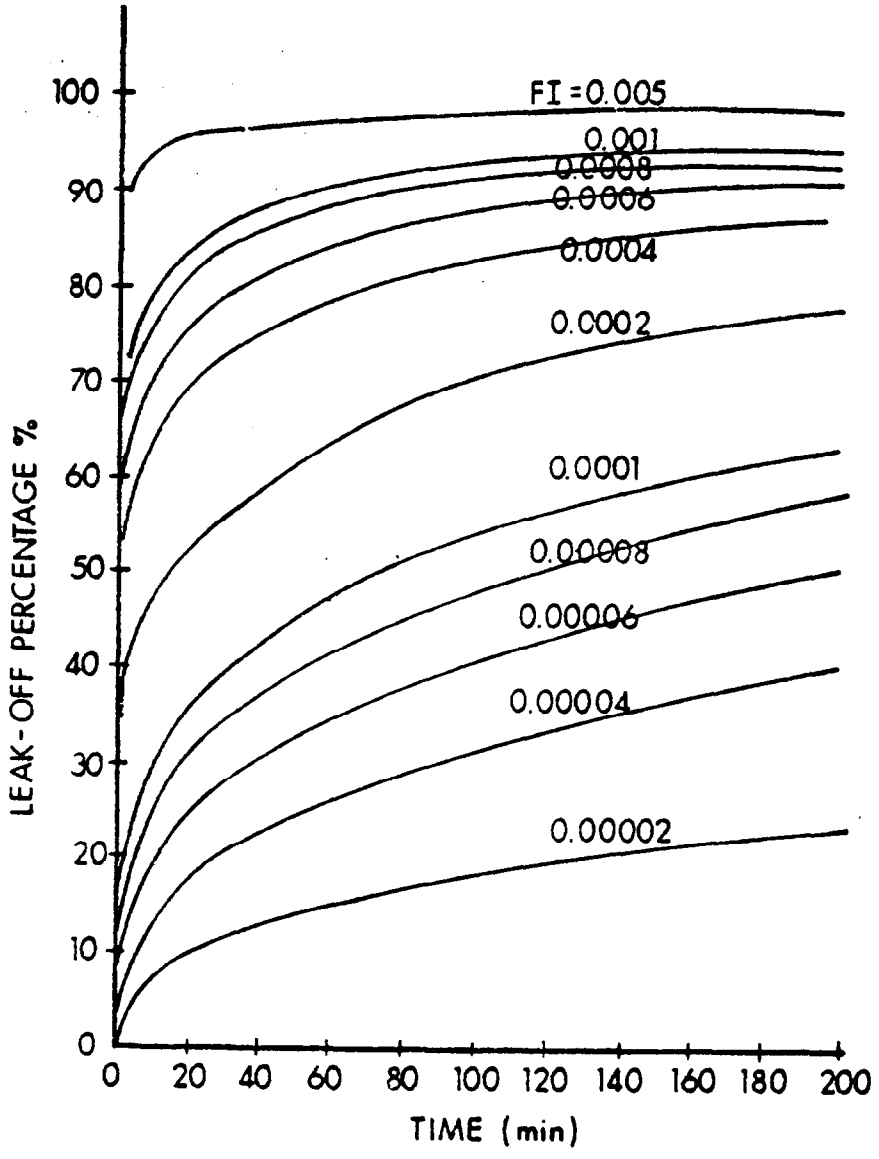

Figure 9a. Percentage Fluid Leak-off versus Treatment Time Plots for Different Flow Indices

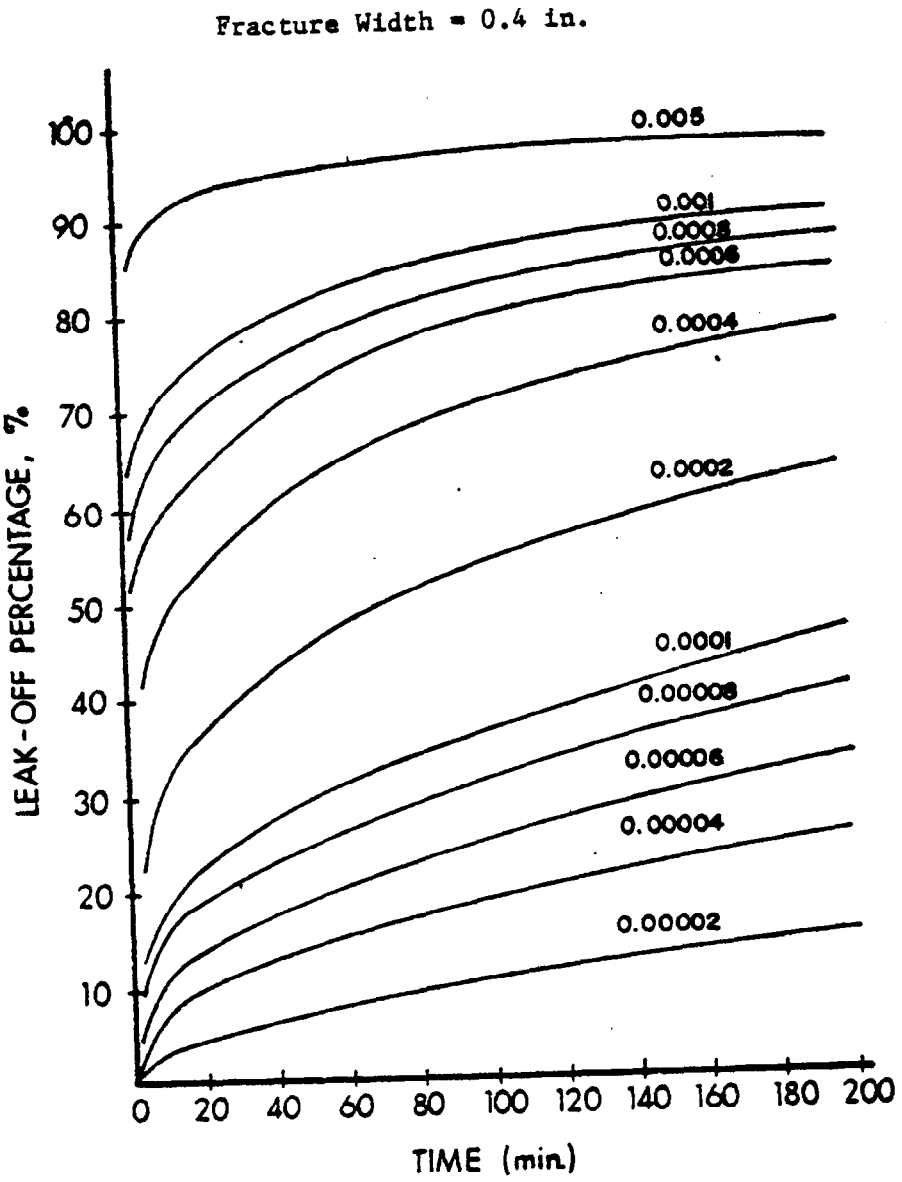

Figure 9b. Percentage Fluid Leak-off versus Treatment Time Plots for Different Flow Indices

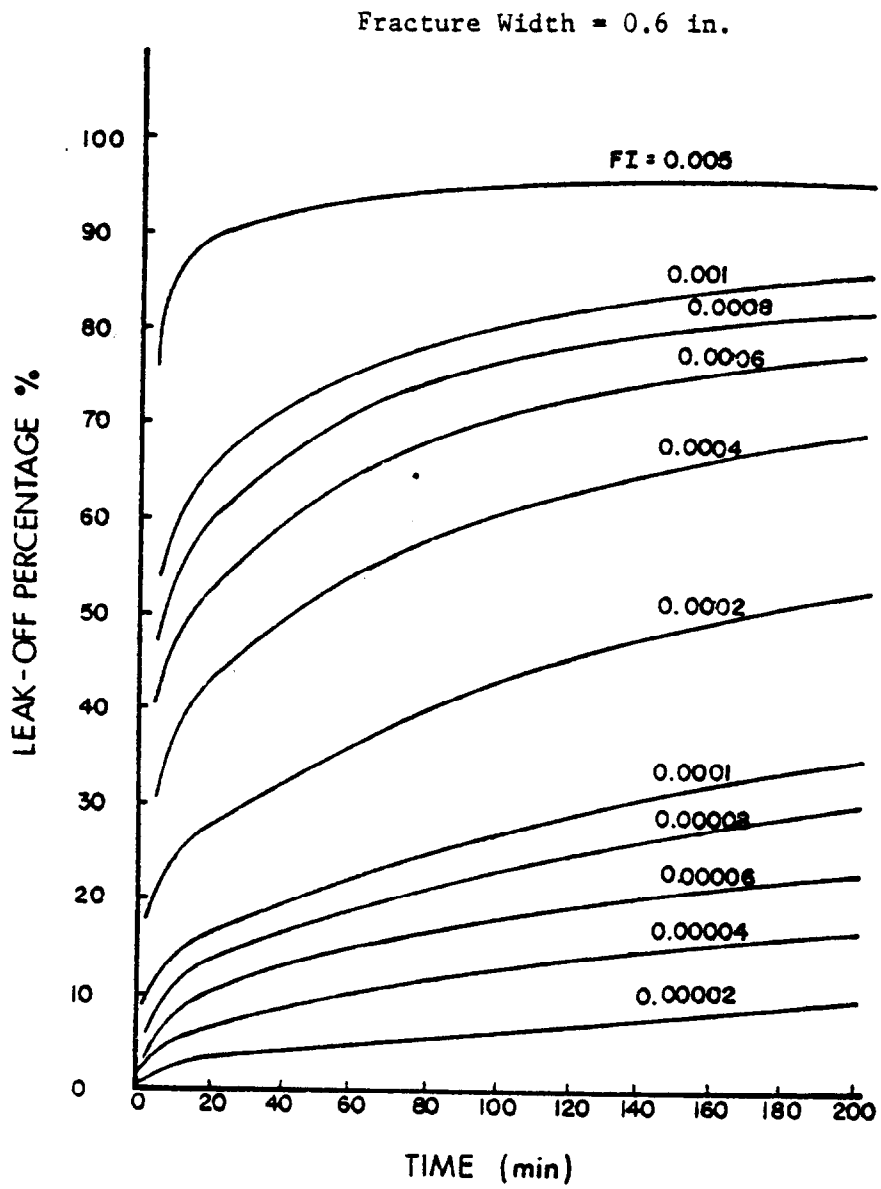

Figure 9c. Percentage Fluid Leak-off versus Treatment Time Plots for Different Flow Indices

modeling section. A more sophisticated approach for estimating fracture widths and resulting fracture extents as a function of fracture geometry, material properties, and flow parameters is presented in the subsequent text.

2.2.2 Two Dimensional Flow Model Simulation: The assumptions pertinent to this simulation entail investigation of the flow in the horizontal plane (Figure 10). The cross-sections of the symmetric crack in the horizontal (x-y) and vertical (y-z) plane are selected to be elliptical while the vertical crack cross-section (x-z plane) is taken to be rectangular. The fluid flow in the formation is analyzed from Darcy's flow considerations, i.e.,

$$Kx \frac{\partial^2 p}{\partial x^2} + Ky \frac{\partial^2 p}{\partial y^2} = (\phi C_f + C_m) \mu \frac{\partial p}{\partial t} \tag{1}$$

where Kx, Ky are the formation permeabilities, p is the pressure in the formation, ϕ is the formation porosity, μ is the fluid viscosity, C_f is the fluid compressibility and C_m is the matrix compressibility.

The initial condition and boundary conditions are

$$p\ (x,y,o) = p_o$$

$$p = p_o \text{ at } x = \pm\infty,\ y = \pm\infty \text{ for all } t$$

The fluid flow inside the crack is assumed to be governed by the Navier-Stokes equation and the pressure drop along the crack is computed from the finite difference formulation by using the velocities obtained from the previous line step. The pressure continuity condition is employed to couple the flows in the crack and formation. Equation (1) is numerically solved by converting it to a finite difference form, with the grid pattern

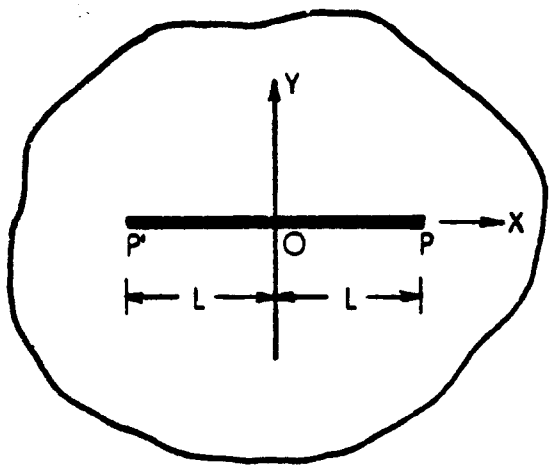

Figure 10. Idealization of Fluid Flow in the Horizontal Plane

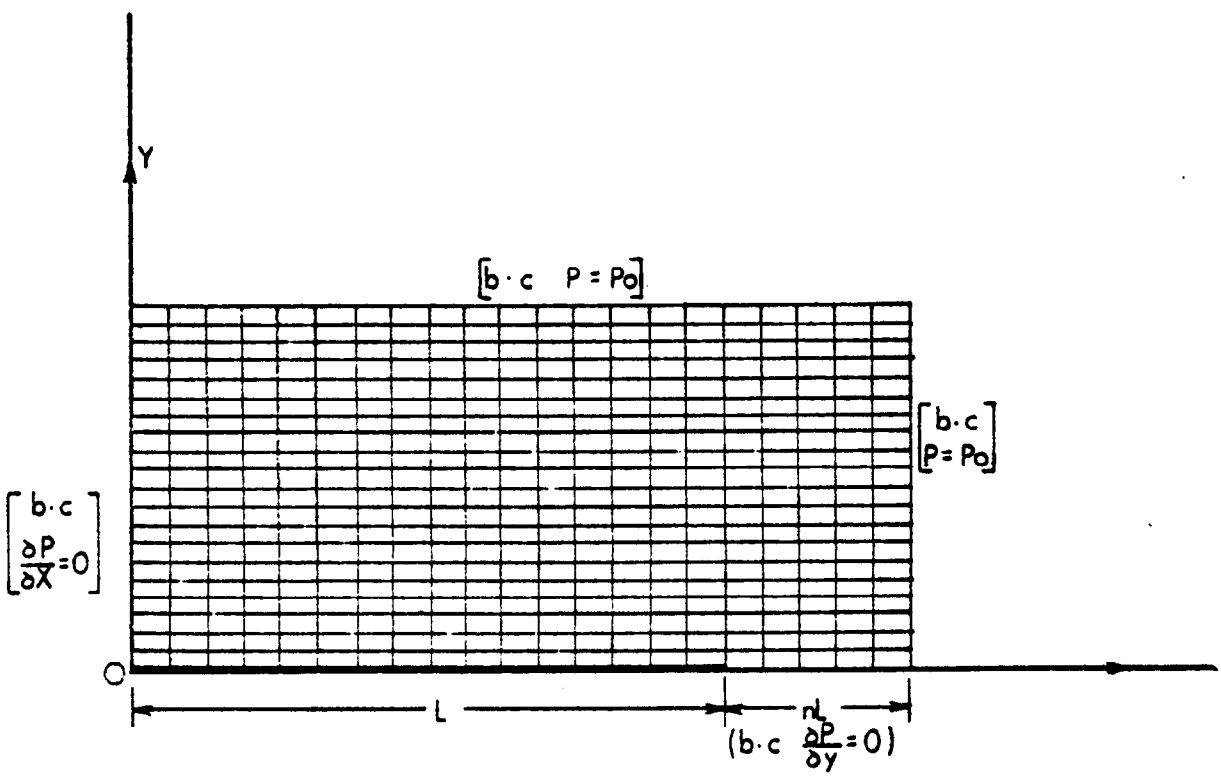

Figure 11. Grid Pattern for the Finite Difference Form of Eq. (1)

illustrated in Figure 11, and using the alternating-direction-implicit-method [19]. The significant steps for the computer simulation are as follows:

(i) A crack length is specified at the initial line step. The corresponding crack width and volume are then calculated.

(ii) The pressure field in the above domain is computed using small time steps and the leak-off velocities through each grid are calculated from the pressure gradient at the crack interface. The fluid leak-off volume is calculated by integrating the velocities over the crack length and elapsed time interval. The overall continuity of mass equation serves as a check for the overall volume.

(iii) Following satisfaction of the continuity equation, within specified error limits, the crack length is suitably increased and the above step is repealed. The computations are terminated when the cumulative value of the time steps equals the time of operation.

The computer programs were initially designed to simulate fracturing fluids with pressure independent responses. Subsequent modifications for foam fracturing studies were made to account for the foam viscosity, compressibility, and hydrostatic column. These considerations along with the investigation of the fracture width are described below.

2.3 FOAM FRACTURE MODELING

Conventional foam fracturing (80% N_2 + 20% H_2O + Surfactant) appears highly desirable for the low temperature, low permeability and low reservoir pressure Devonian shale formations. The advantages of using foam include [20,21,22]: (a) improved fracture efficiency, (b) rapid clean-up due to nitrogen uplift, (c) low leak-off, (d) reduced formation damage

from fluid penetration, (e) good proppant transport because of the high effective viscosities of the Bingham plastic foam, and (f) small friction losses in pipes. The principal disadvantages are the low amount of sand and its slow settling characteristics.

The viscosity of the foam was initially calculated from its shear rate and plastic yield stress [20]. However, it was later assumed that the foam viscosity obeys Hatchek's theory and was defined by

$$\mu_f = \begin{cases} \mu_e\ (1 + 2.5\ \Gamma) & \Gamma \leq 0.52 \\ \mu_e\ (1 + 4.5\ \Gamma) & 0.52 \leq \Gamma \leq 0.75 \\ \mu_e\ [1/(1 - \Gamma^{1/3})] & \Gamma > 0.75 \end{cases}$$

where μ_f is the viscosity of the foam, μ_e is the Bingham plastic viscosity, and Γ is the foam quality.

The foam compressibility is obtained by assuming it to be a homogeneous, immissible mixture of liquid and ideal gas. The overall compressibility c is evaluated from the approximate relation

$$c = c_f\ (1 - \Gamma) + \Gamma/p$$

This expression is introduced in an explicit form in the preceding two dimensional finite difference formulation. The bottom hole treatment pressure is appropriately corrected for the hydrostatic head and friction loss in the pipe.

The crack width is computed by refining the approach of Geerstma and de Klerk [7]. This modification entails the investigation of the crack width in a vertical plane (i.e., corresponding to the plane strain model) rather than the horizontal plane. With this assumption, the resulting derivations are altered and the maximum crack width, W_{max} can be expressed by

$$2W_{max} = \left[\frac{24\mu\ Q\ L(1-\nu)}{\pi G}\right]^{1/4} \tag{2}$$

where μ is the fracturing fluid viscosity, Q is the fluid flow rate, L is the half crack length, ν is the formation Poisson's ratio and G is the shear modulus.

The averaged crack width integrated over the entire length and height of the fracture, for volume calculations, can be obtained to be

$$2W_{average} = \frac{\pi}{5}\left[\frac{24\mu\ Q\ L\ (1-\nu)}{\pi G}\right]^{1/4} \tag{3}$$

To demonstrate the applicability of the foam fracture model, the data from Consolidated Gas Supply Corporation treatment of W. L. Pinnel No. 12041 [23] near Cottageville, Jackson County is used. The selected values employed for the model simulation are detailed in Table I.

TABLE I

Selected Data for W. L. Pinnel Well #12041 Foam Fracture Treatment

Shale Permeability	20/100 μ darcies
Young's Modulus E	5×10^6 psi
Poisson's Ratio ν	0.2
Shale Porosity	0.05
Pore Porosity	564 psi
Average Treatment Depth	3520 ft.
Average Surface Flow Rate	20 BPM
Average Surface Foam Quality	0.75
Average Surface Pressure	1300 psi
Shut in Pressure	400 psi
Pressure Gain - Hydrostatic Column	569 psi

TABLE I (continued)

Friction Loss in Pipe	366 psi
Downhole Treatment Pressure	1503 psi
Downhole Flow Rate	18 BPM
Bottom Hole Foam Density	22.7 lb/ft^3
Effective Pressure on Crack	103 psi
Foam Viscosity	21.24 Centipoise

Figure 12 illustrates the computed total fracture length versus time curves for the four cases presented in Table II. A Tabulation of the fracture geometry and leak-offs for these cases is also given along with fracture length comparisons using the nomographs presented in Figures 7 and 8. Corresponding results for different fracturing treatments are given in Appendix A.

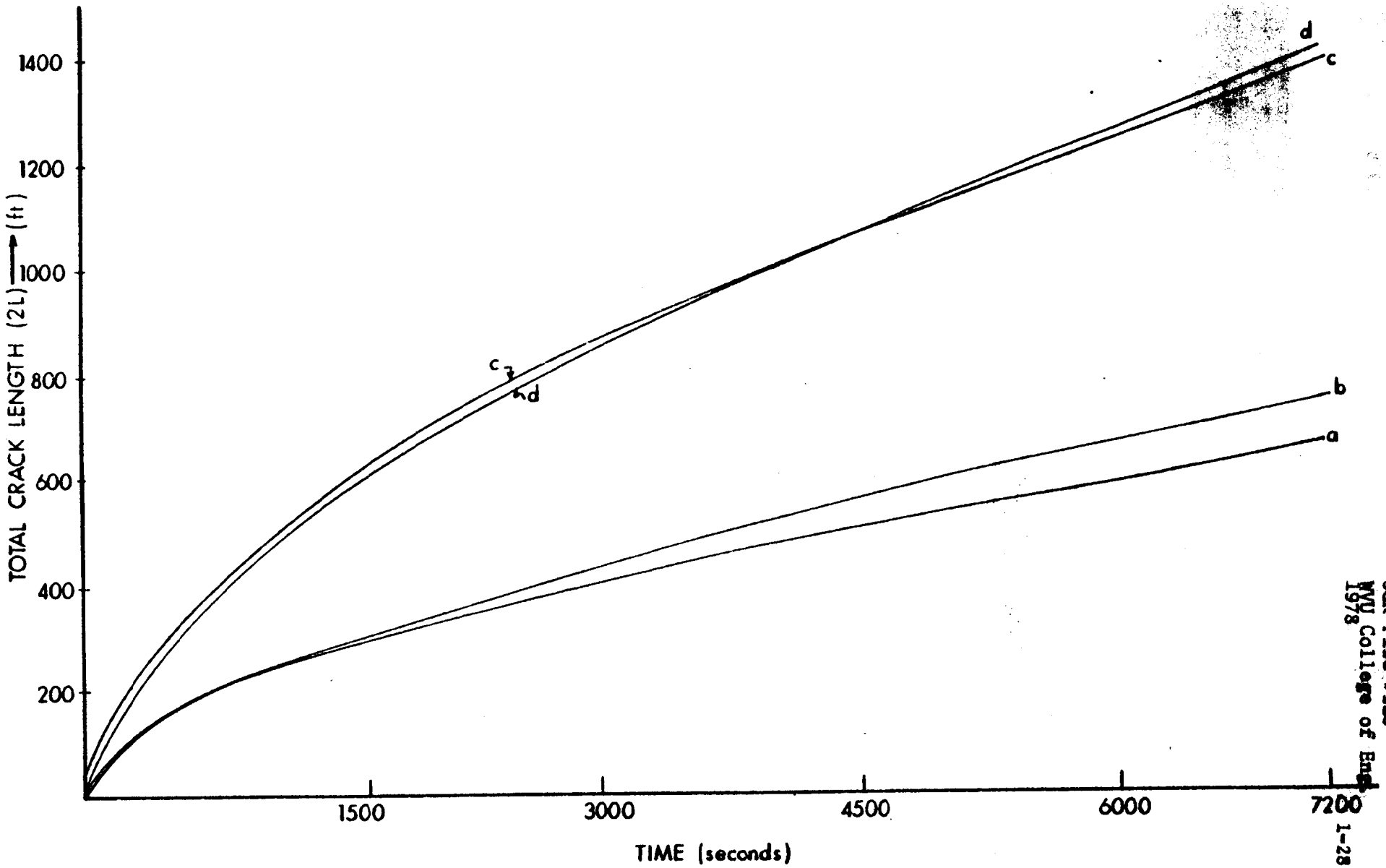

Figure 12. Computed Total Fracture Length versus Time for the Four Cores in Table II

UGR File #125
WVU College of Eng
1978
1-28

TABLE II

Predicted Fracture Geometry, Leak-off, and Fracture Length Comparisons

Case	Formation Permeability	Average Fracture Width	Fracture Height	Total Leak-off %	Total Leak-off Volume	Fracture Length[2]	Fracture Length[3]
a	0.10 md	0.1197 in[1]	159 ft.	93.4	11,591 cu.ft.	660 ft.	531 ft.
b	0.10 md	0.0655 in.	159 ft.	95.0	11,790 cu.ft.	750 ft.	630 ft.
c	0.02 md	0.0765 in.	159 ft.	88.6	10,801 cu.ft.	1390 ft.	1200 ft.
d	0.02 md	0.119 in.	159 ft.	85.8	10,371 cu.ft.	1400 ft.	1205 ft.

[1]Fracture Width from Conventional Calculations

[2]Fracture Length from Two Dimensional Simulation

[3]Fracture Length Using Nomographs (Figures 7 and 8)

UGR File #..45
NVU College of Eng.
1978

3.0 DESIGN APPLICATIONS

The general use of the design charts and specific examples pertaining to hydraulic stimulation of Upper Devonian Shales are presented here.

To illustrate the predictive application of Figures 7 and 8, we examine the case wherein the treatment time is 120 minutes, $Q_{average}$ = 32 BPM, the loss coefficient flow index FI = 0.0001 ft/ sec, and the fracture width is 0.3 in. We first obtain the pseudo fracture area FA = 0.76×10^6 corresponding to FI = 0.0001 ft/ sec and T = 120 min. from Figure 7a and then draw a horizontal line to meet the vertical axis AB at point P_1. The point P_2 on OP_1 is located for Q = 32 BPM and the fracture area corresponding to a fracture width of 0.2 in. is 0.55×10^6 ft^2. This value is adjusted by applying the correction factor ratio of 0.9 obtained in Figure 8 for the relative areas corresponding to the two widths, i.e., (FA) = 0.495×10^6 ft^2.

The structural and fluid flow response curves also serve as a tool for design of hydraulic fracture treatments. We briefly consider here the applicability of the results to the stimulation experiments for the Columbia Gas - DOE three well program in Lincoln County, West Virginia [24]. In this program, three new wells have been drilled in four distinct shale zones to a depth of 4000 ft. Two of the wells (#20401 and #20403) have been independently fractured at different depths with MHF (foam), MHF (Gel/N_2), and NHF (Gel-N_2/Foam) treatments. Wells #20402 and #20403 have been cored and limited mechanical property and <u>in situ</u> stress data for the different zones is available [25]. This data suggests that the minimum horizontal <u>in situ</u> stress in the middle brown layers is lower than

the corresponding value in the gray shale zones. A preliminary prediction for the stimulation of the middle brown layer for Well #20402 is suggested here (2h = 250 ft).

The value of the ratio E_2/E, based on the available Terra Tek data [25] is 1.25. For this ratio, the appropriate fracture containment curve for different in situ stress differences, analogous to Figure 6, is illustrated in Figure 13. The critical stress intensity factor values for the middle gray and middle brown layers are also designated in this figure. The Terra Tek data indicates a minimum in situ stress difference of $\Delta\sigma$ = 800 psi between the middle gray and middle brown zones. Since a precise control of the bottom hole treatment pressure is difficult, we select a value of $P_{effective} = P - \sigma_2$ = 300 psi. This effective pressure causes the fracture to penetrate vertically across the layer interfaces and propagate laterally. The total fracture height for $P_{effective}$ = 300 psi and $\Delta\sigma$ = 800 psi, from Figure 13, is given by 2H = 330 ft. The average fracture width for H/h = 165/125 = 1.32, by subtracting the respective widths obtained from Figures 4b and c, is given by $2w = 2(w_1 - w_2)$ = 0.24 in.

The following data is employed in the foam fracture simulation:

Reservoir Data: Permeability k = 0.1 md, Porosity ϕ = 0.05, Pore Pressure p_o = 250 psi, σ_{HMIN} = 1800 psi.

Fracture Fluid Data: P_{BHTP} = 2100 psi, Foam Viscosity μ = 21.24 centipoise, Foam Quality Γ = 0.8, Flow Rate Q = 30 BPM, and Treatment Duration T = 180 minutes.

The loss coefficient or flow index FI is obtained to be FI = .0000842 ft/ sec. The fracture area from Figure 7a, corresponding to the adjusted bottom hole flow rate of 26.53 BPM, is 0.69×10^6 ft^2. Applying the width correction

factor of 0.96 (Figure 8), the fracture area is 0.66×10^6 ft^2. This value yields a total fracture length given by $0.66 \times 10^6/330 = 2000$ ft.

4.0 DISCUSSION AND CONCLUSIONS

In this paper the formation structural and fracturing fluid response model simulations are detailed from the vantage point of predicting fracture geometry as a function of the reservoir properties (geometry, material properties, pore pressure, permeability/porosity, in situ stresses) and fluid forcing parameters (bottom hole treatment pressure, viscosity, compressibility and density). Design curves and examples pertaining to crack penetration across layered media, fracture width determination, fluid leak-offs, and fracture extent are presented for selected Devonian Shale, properties and fluid treatment parameters. Optimum hydraulic stimulation treatments, based on design objectives, can be specifically site tailored by controlling the forcing fluid parameters. Although the influence of proppant size and concentration have not been explicitly introduced in the model formulations, the fracture width expressions can be empirically modified to account for their effects.

The areas requiring further investigation include work on

(a) Rheological property characterization of foam at different shear rates and temperatures.

(b) Proppant settling properties and crack closure relative to different fracturing fluids in Devonian Shales.

(c) Mechanisms for crack arrest, penetration across multi-layered interfaces, and vertical fracture contour mapping.

(d) In-situ stress determinations.

(e) Laboratory/mine back experiments for studying effects of flow cycling, i.e., dendritic fracturing.

5.0 REFERENCES

1. Overbey, W. K., Jr., "Increasing Eastern U.S. Natural Gas Reserves from Gas Bearing Shales," SPE Paper No. 6364, 1976.

2. Schrider, L. A., Komar, C. A., and Pasini, J., III., "Natural Gas from Eastern U.S. Shales," SPE Paper No. 6841, 1977.

3. Komar, C. A., Frohne, K. H., and Yost, A. B., "Stimulation Technology - A Program Review," Informal METC Report, February 28, 1978.

4. Zheltov, Yu P., and Kristianovitch, S. A., "The Hydraulic Fracturing of an Oil-Producing Formation," Izvest. Akad. Nauk SSSR, Otdel Tekh Nauk, No. 3, 41, 1955.

5. Haimson, B. and Fiarhurst, C., "Initiation and Extension of Hydraulic Fracturing in Rocks," Society of Petroleum Engineers Journal No. 3, 7, 1967.

6. Haimson, B. and Fairhurst, C., "Hydraulic Fracturing in Porous-Permeable Materials," Journal of Petroleum Technology, No. 7, 21, 1969.

7. Geertsma, J. and de Klerk, F., "A Rapid Method of Predicting Width and Extent of Hydraulically Induced Fractures," Journal of Petroleum Technology, No. 12, 7, 1969.

8. Daneshy, A. A., "Rock Properties Controlling Hydraulic Fracture Propagation," SPE Paper No. 5752, 1976.

9. Daneshy, A. A., "Hydraulic Fracture Propagation in Layered Formations," SPE Paper No. 6088, 1976.

10. Shuck, L. A. and S. H. Advani, "Induced Stresses in Hydraulic Fracturing Operations," Proceedings 15th Conference on Rock Mechanics, E. R. Hoskins, Editor, ASCE Publication, 1975.

11. Simonsen, E. R., Abou-Sayed, A. S. and Clifton, R. J., "Containment of Massive Hydraulic Fractures," SPE Paper #6089, 1976.

12. Advani, S. H., Shuck, L. Z., Chang, H-Y, GangaRao, H., "Material and Structural Mechanics Simulations Associated with Hydraulic Fracturing Operations," Proceedings 1976 International Conference on Computer Simulation for Materials Applications, Nuclear Metallurgy Vol. 20, Pet 2, 1976.

13. Advani, S. H., Shuck, L. Z., Chang, H-Y, and GangaRao, H., "Analytical and Experimental Investigations on Induced Fracturing of Reservoir Rock," ASME Paper No. 76-Pet-8, 1976.

14. Chang, H-Y, "Development of Improved Design Criteria for Hydraulic Fracturing Operations," Ph.D. Dissertation, West Virginia University, Morgantown, WV, 1978 Pending.

15. Erdogan, F. and G. D. Gupta, "On the Numerical Solution of Singular Integral Equations, Quarterly of Applied Mathematics," Vol. 29, 1972.

16. Carter, R. D., "Derivation of the General Equation for Estimating the Extent of the Fractured Area," Appendix to Chapter on Optimum Fluid Characteristics for Fracture Extension by Howard, G.C. and Fast, C.R., Drilling and Production Practice, API, 1975.

17. Howard, G. C. and Fast, C. R., "Hydraulic Fracturing," SPE Monograph, Vol. 2, 1970.

18. Anon, "The Fracbook Design/Data Manual," Halliburton Services Co., 1971.

19. Von Rosenberg, D. U., "Methods for the Numerical Solution of Partial Differential Equations," American Elsevier Publishing Co., Inc., New York, 1969.

20. Blauer, R. E., Mitchell, B. J., and Kolhaas, C. A., "Determination of Laminar, Turbulent, and Transitional Foam Flow Losses in Pipes," SPE Paper No. 4885, 1974.

21. Blauer, R. E. and Kolhaas, C. A., "Formation Fracturing with Foam," SPE Paper No. 5003, 1974.

22. Abbot, W. A. and Vaughn, H. F., "Foam Frac Completions for Tight Gas Formations," Petroleum Engineering, 1976.

23. Frohne, K-H, "Large Scale Foam Fracturing in the Devonian Shale - A Field Experiment in West Virginia," MERC/TPR-77/2, April 1977.

24. Creamen, S., "Novel Fracturing Treatment in the Devonian Shale," First Eastern Gas Shales Symposium, MERC/SP-77/5, In Press.

25. Brechtel, C. E., Abou-Sayed, A. S., and Clifton, R. J., "In-Situ Stress Determination in the Devonian Shales (IRA McCoy 20402) Within the Rome Basin," Terra Tek Report TR-77-36, July 1976.

APPENDIX A

Attached are selected crack length vs. time and leak-off vs. time simulations for Wells #1627, Clark #1, and Kentucky Hazard #7239. These plots are obtained from the two dimensional flow orientations described in the text using the finite difference approach.

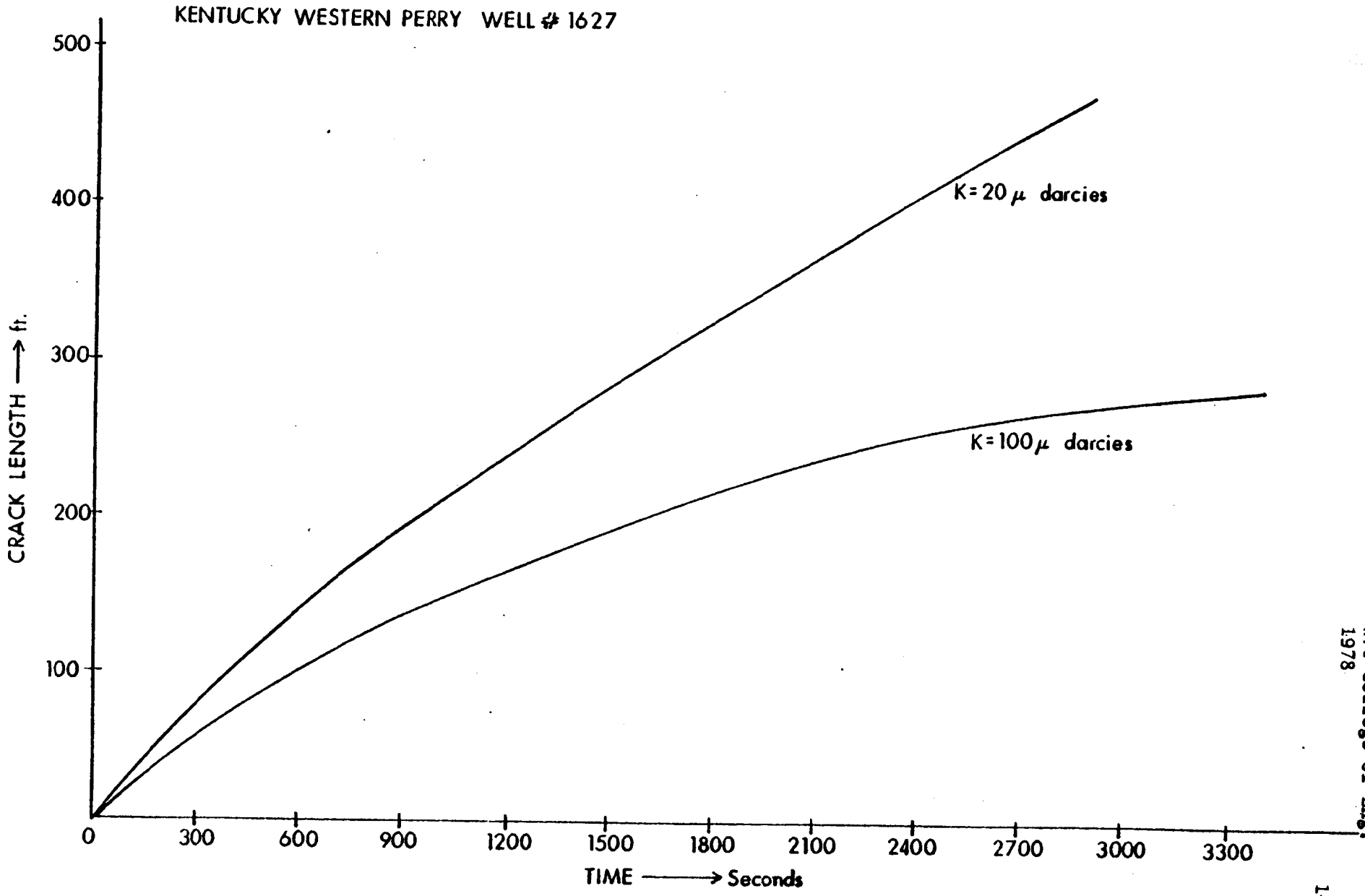

Figure A.1. Crack Length vs. Time of Kentucky Western Perry Well #1627

WVU College of Eng.
1978

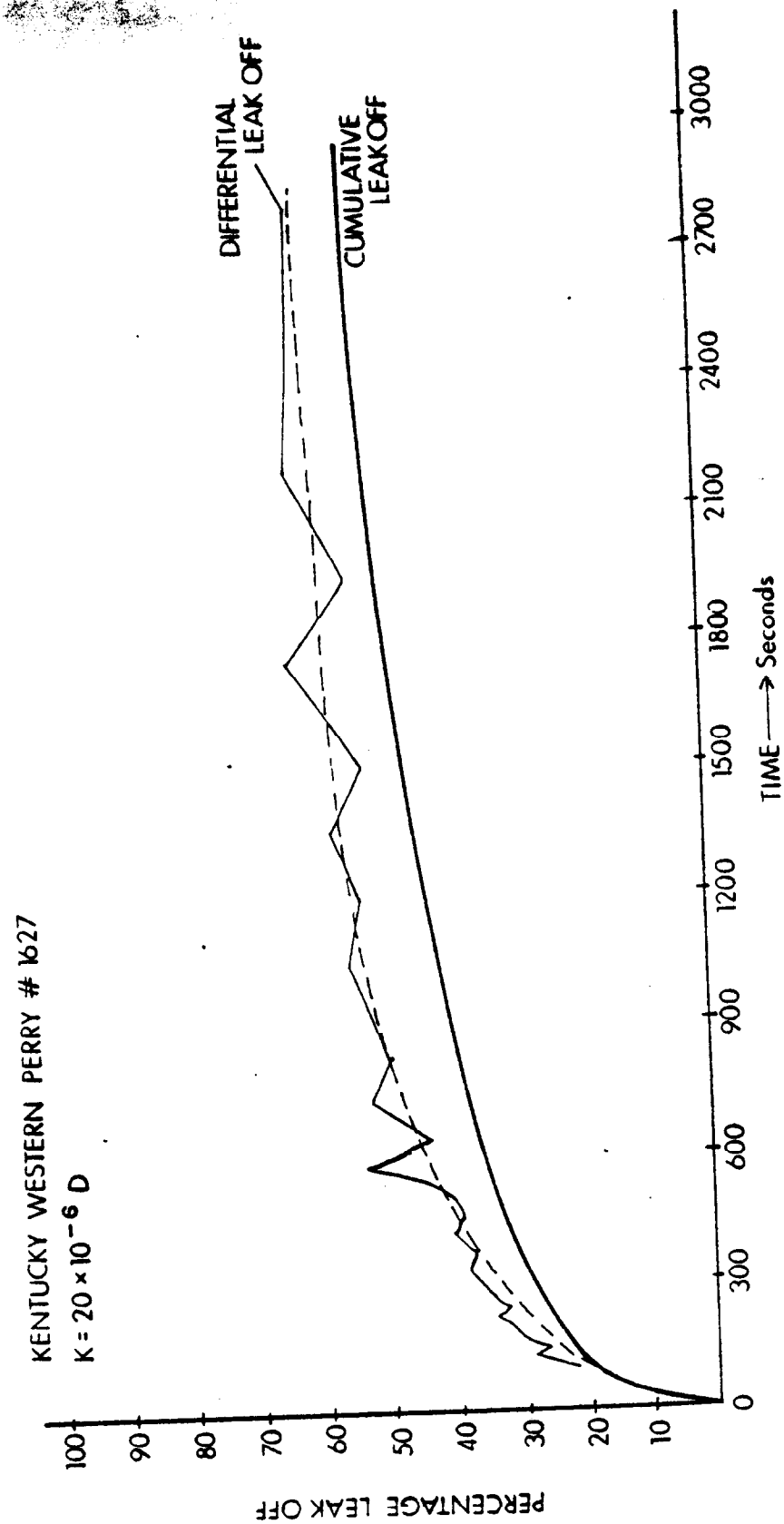

Figure A.2. Percentage Leakoff vs. Time of Kentucky Western Perry #1627

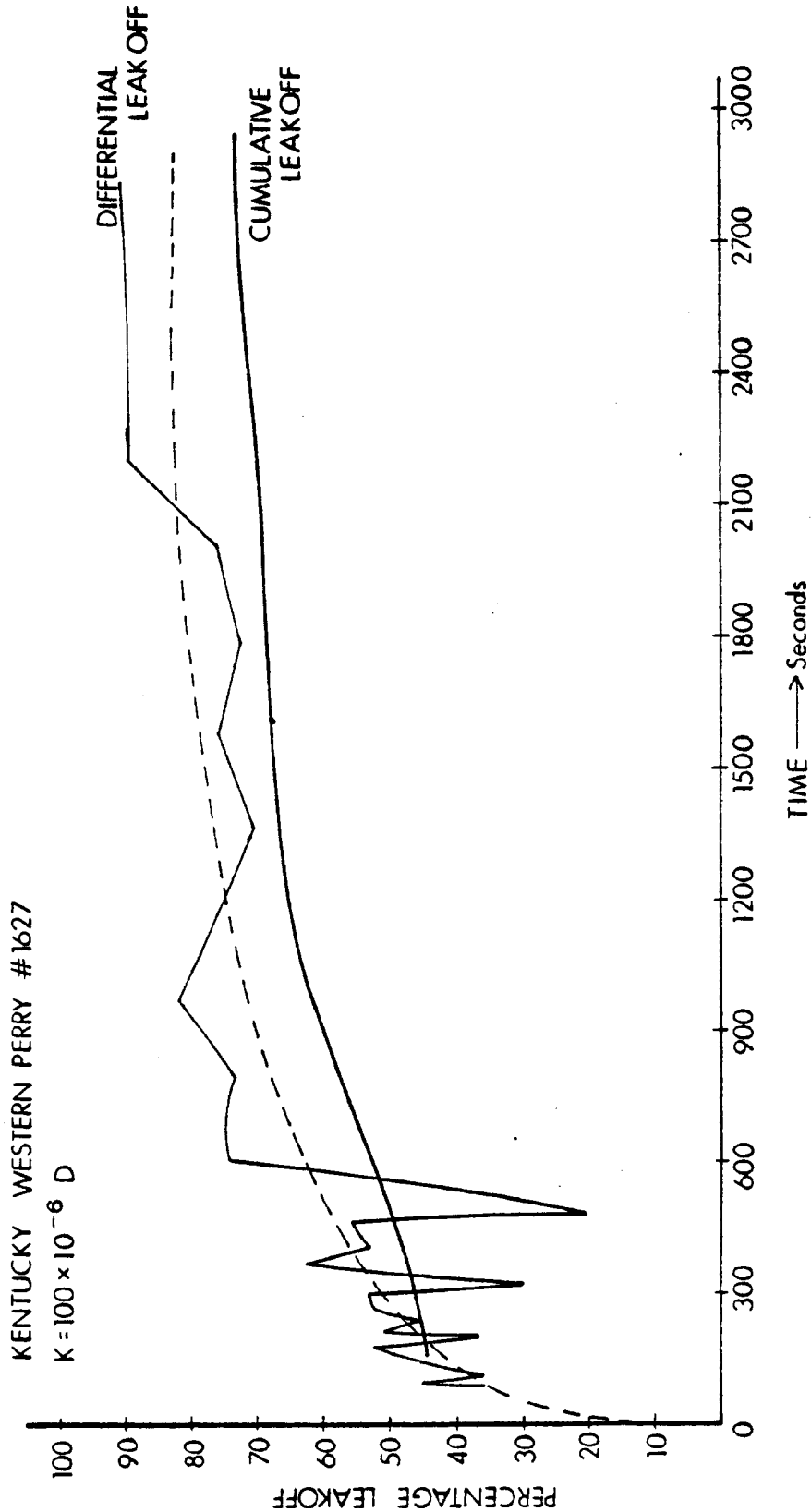

Figure A-2. (Continued)

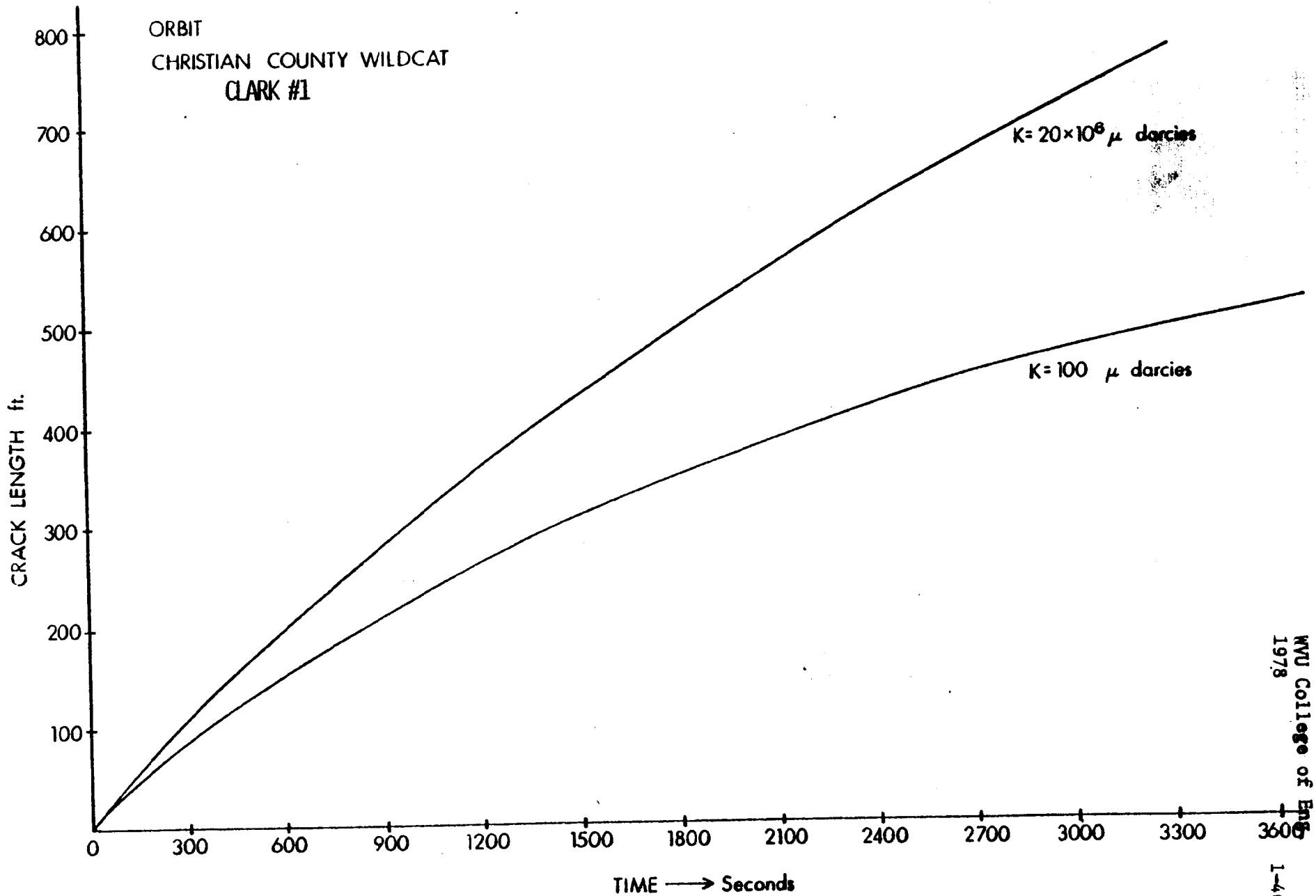

Figure A-3. Crack Length vs. Time of Orbit Christian Wildcat Clark #1

UGR File #125
WVU College of Eng
1978

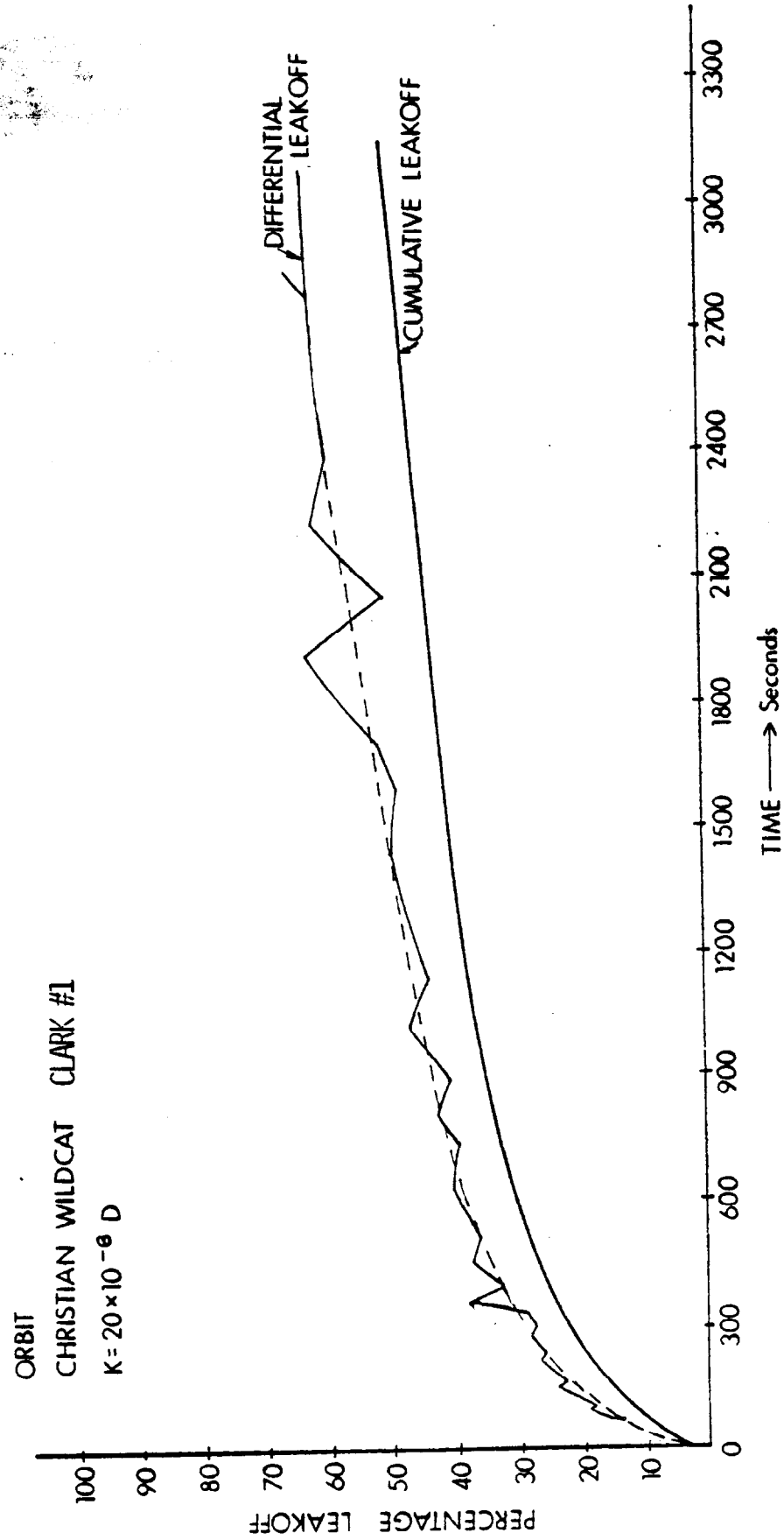

Figure A-4. Percentage Leakoff vs. Time of Orbit Christian Wildcat Clark #1

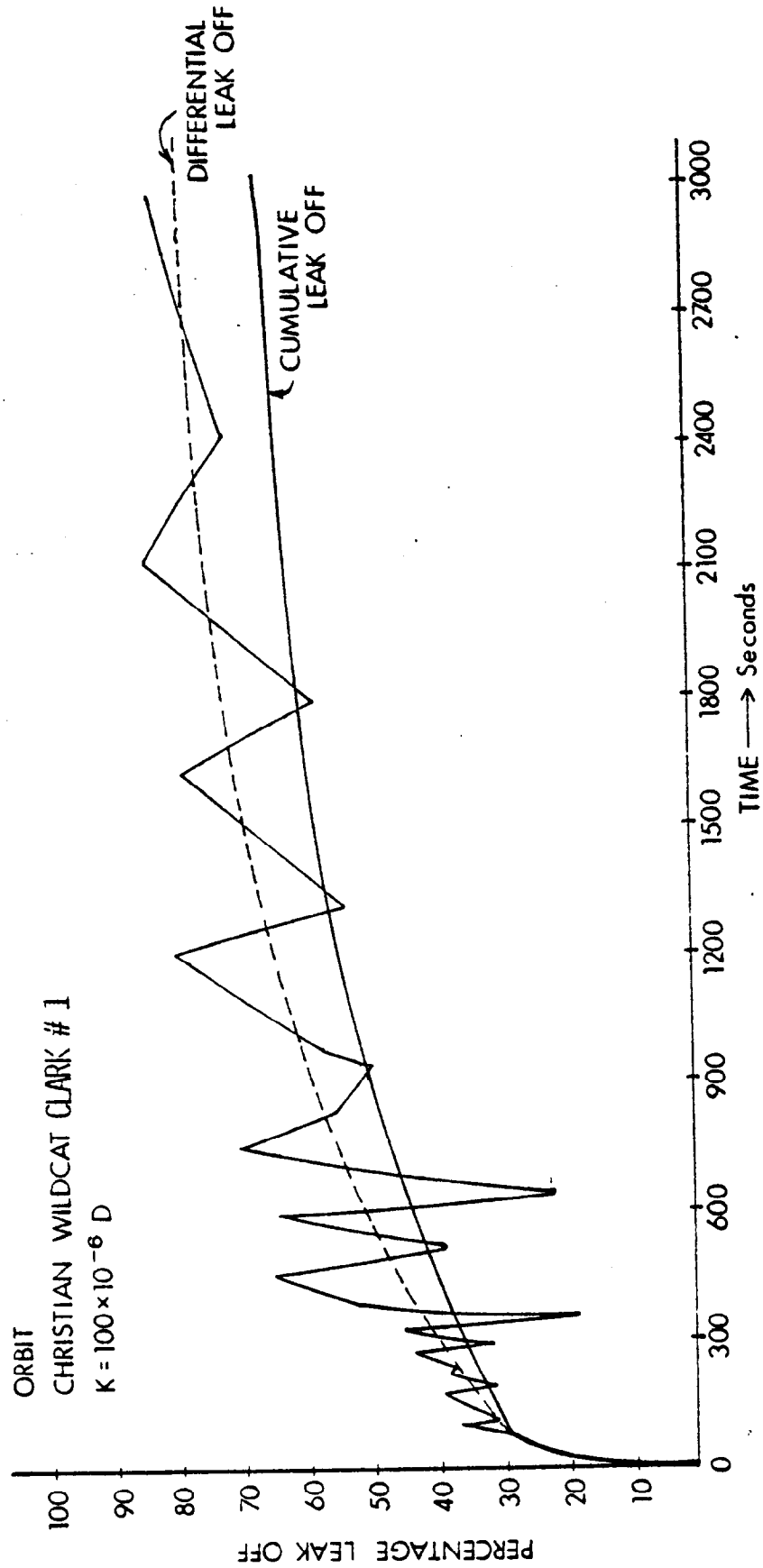

Figure A-4. (Continued)

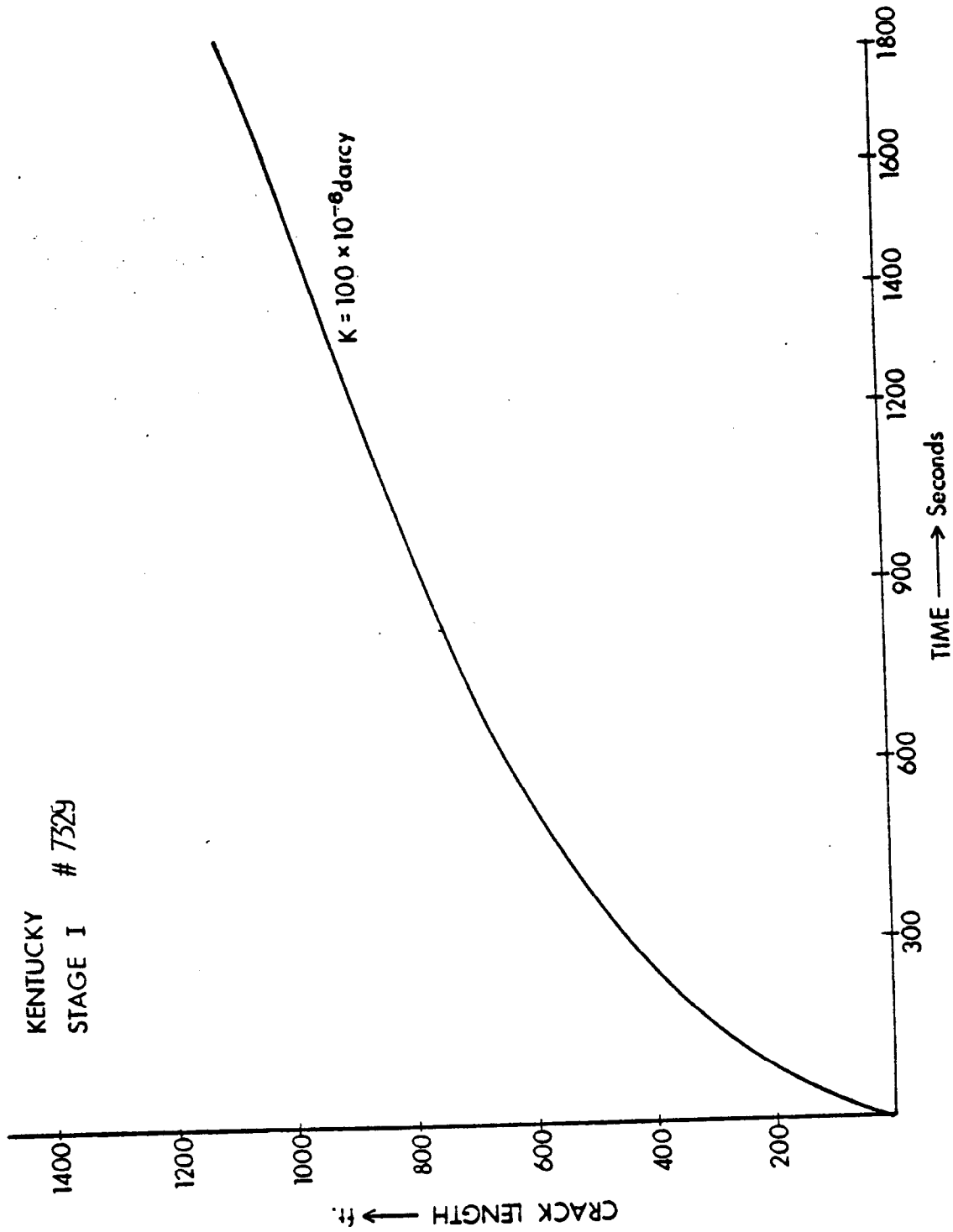

Figure A-5. Crack Length vs. Time of Kentucky Stage I #7329

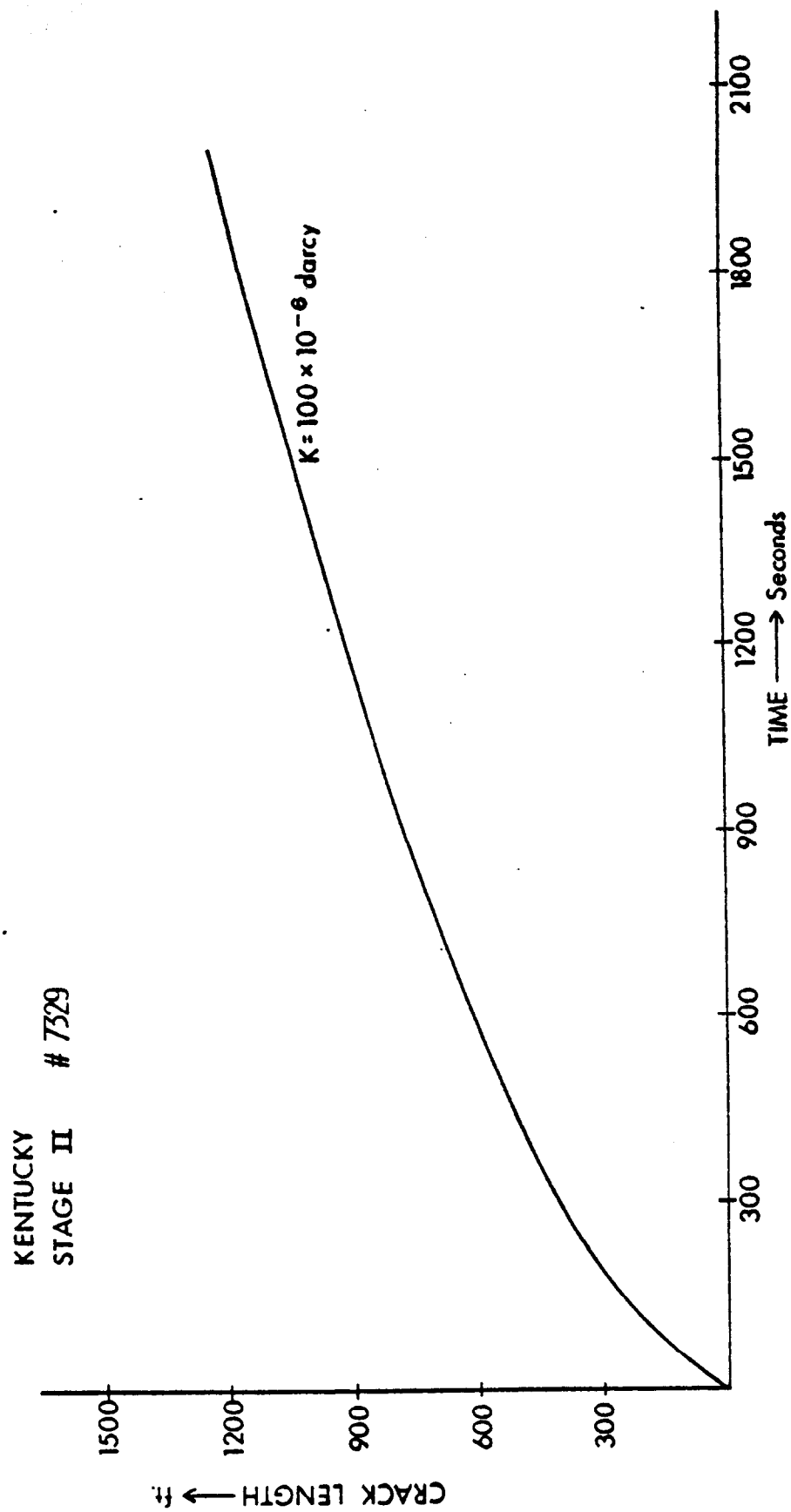

A-6. Crack Length vs. Time of Kentucky Stage II #7329

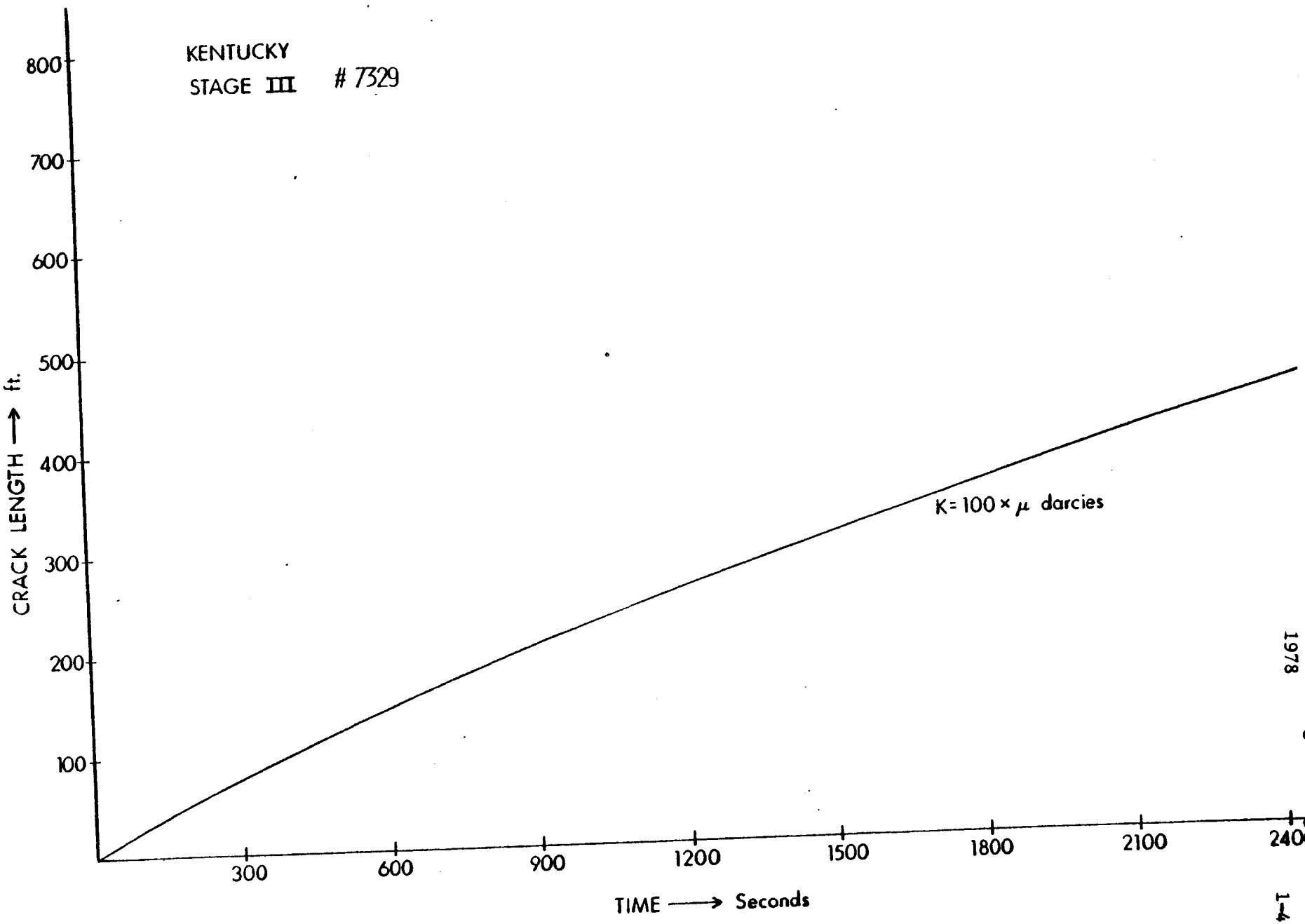

Figure A-7. Crack Length vs. Time of Kentucky Stage III #7329

WVU College of Engr.
1978
1-45

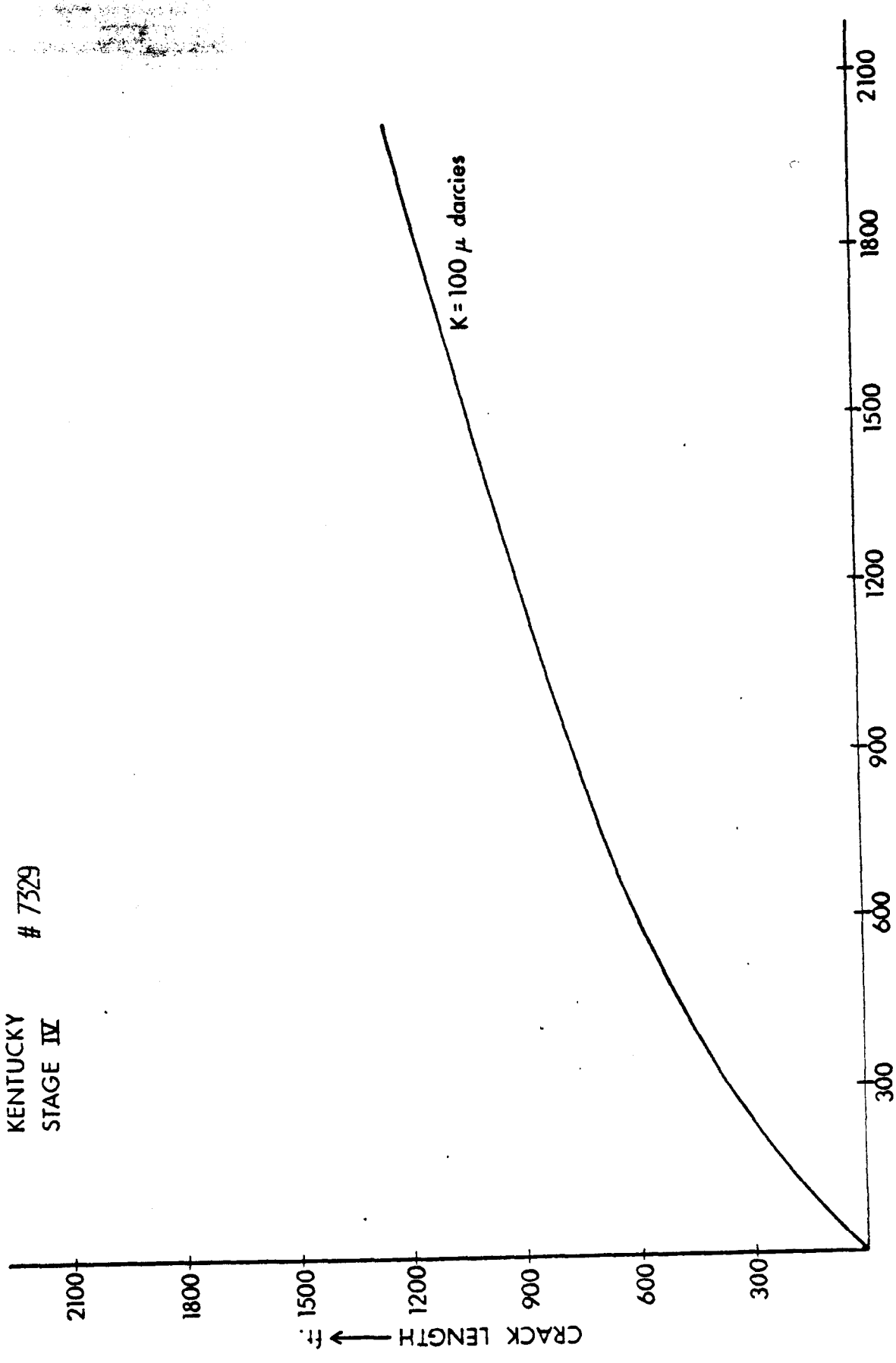

Figure A-8. Crack Length vs. Time of Kentucky Stage IV #7329

UGR File #125
WVU College of Eng.
1978

PART II

IN-SITU STRESS DETERMINATION BASED ON FRACTURE RESPONSES ASSOCIATED WITH CORING OPERATIONS

By

H.V.S. GangaRao, S. H. Advani, P. S. Chang and S. C. Lee

College of Engineering
West Virginia University
Morgantown, WV 26506

UGR File #125
WVU College of Eng.
1978

PART II
IN-SITU STRESS DETERMINATION BASED ON FRACTURE RESPONSES ASSOCIATED WITH CORING OPERATIONS

ABSTRACT

The classical theories of elasticity, finite element methods, fracture mechanics and failure criteria (Mohr-Coulomb Theory) are applied in understanding the crack formations in the drilled-out cores, simulating of coring induced stresses, and consequently evaluating the ranges of in-situ stresses at great depths. Herein, fracture angles on the core are measured to find the internal friction angles which in turn have been used to determine the in-situ tectonic stresses.

The effects of drill bit loading, overburden pressure, tectonic stresses, foam pressure and pore pressure on the crack formation are systematically studied by using the Potential Function Theory as well as the finite element techniques. Two and three dimensional finite element modeling is conducted for isotropic as well as anisotropic material properties.

The results show that the relative effect of bit load on local stresses in comparison with other loadings is negligible. However, Mohr-Coulomb's shear failure theory associated with the other loads indicates that the failure occured on the periphery of the core and slightly ahead of the bit load. Based on the trial and error procedure with two constraints (neither of the in-situ stresses can exceed the overburden pressure and the in-situ stress ratio is between 0.5 to 2 on the basis of field observations) a range of in-situ stresses,

S_1 = 2550 to 2650 psi and S_2 = 1950 to 2950 psi for 3000 ft depth in the Devonian Shales, is obtained. Also, Sih' strain energy density concept is employed to verify the in-situ stresses obtained from the above approach. The derived values of in-situ stresses are not widely scattered and compared well with some of the existing information.

Finally, it is recommended that refined failure criteria, three-dimensional non-linear material properties, special finite elements with crack tip effects, etc. be employed to arrive at more meaningful and accurate in-situ stresses.

1·0 INTRODUCTION

Accurate prediction of in-situ stresses is very important in the selection and design of stimulation treatments to maximize gas production and minimize the adverse environmental effects, such as ground subsidence, stability of underground excavation during the underground mining of coal gasification process. In addition, accurate prediction of in-situ stresses is esential to arrive at optimal interconnection between the wells in terms of their location and spacing. Hence the principal objective of this study is to examine the feasibility of determining the magnitudes of the horizontal in-situ stresses and/or in-situ stress ranges at great depths (3000'-7000') from the induced fracture patterns observed in Devonian Shale cores. The typical fracture patterns are the petal fracture, centerline fracture and discing which are shown in Fig.1·1. Three distinct fracture regimes are identified: 1) The fracture initiation stage where 3-D Mohr-Coulomb criterion is used to identify fracture initiation: 2) The fracture extension stage where strain energy density concept for a line crack subjected to internal pressure is employed; and 3) The center line fracture where a simple vertical fracture criterion similar to hydraulic fracturing is used.

The analysis of coring mechanisms, associated induced stress fields and fracture responses involve utilization of concepts in geology, fluid mechanics and solid mechanics. In the stress response analysis of the core, numerous ill-defined variables such as natural fracture systems, material inhomogenities and pore pressure effects contribute to the structural and constitutive complexities. The stresses

around the base of the well for a semi-infinite inhomogeneous medium are obtained from theories of elasticity by idealizing it as a two demensional medium with a linear, homogeneous, isotropic material properties. Also, the medium is analyzed with the aid of finite element techniques by considering two and three demensional elements and assuming the anisotropic material properties. The analysis is conducted by properly accounting for the drill bit loading, overburden, foam pressure, pore pressure and a wide range of horizontal in-situ stresses. Suitable rock mechanics failure criteria and fracture theories are applied to obtain fracture initiation sites and extension characteristics prior to the evaluation of horizontal in-situ stresses.

The proposed approach is different from other methods in which in-situ stresses very close to earth' surface, are measured. These methods are summarized in Appendix A.

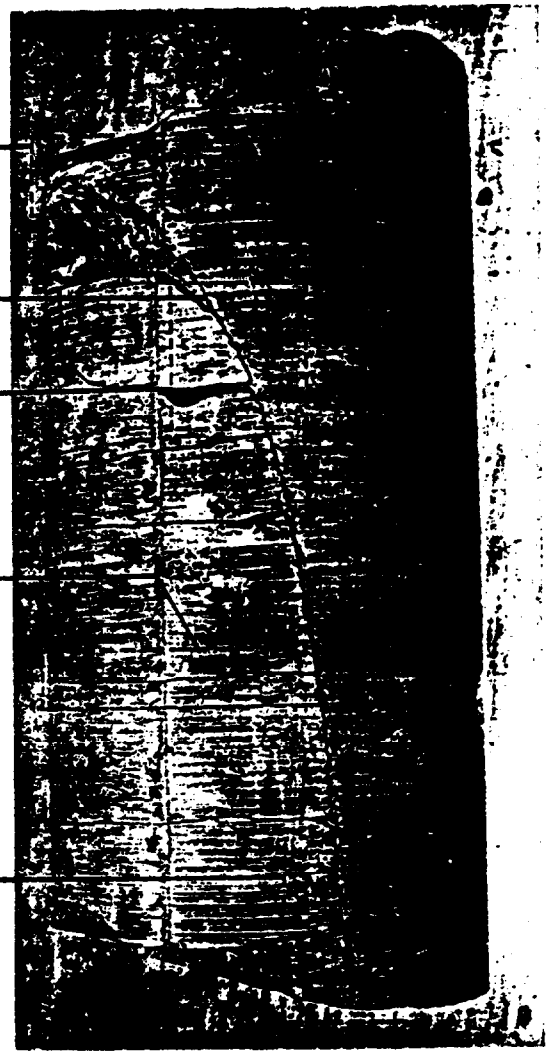

Figure 1·1

Typical Fracture Patterns of Core

2. IN-SITU STRESS DETERMINATION BASED ON THEORIES OF ELASTICITY AND FRACTURE

The analysis of coring-induced stress fields and associated fracture formation aspects involves utilization of concepts in solid mechanics, geology and fluid mechanics. The in-situ stress computations presented in this chapter correspond to cores from Devonian shales with linear, homogeneous, isotropic material properties and subjected to drill bit load, foam pressure, pore pressure and in situ stresses. However, the shear stress caused by bit rotation is neglected in our computations. Also, for varying in situ stress values, suitable failure theories and fracture criteria are applied to understand the fracture initiation and extension phenomenon.

2.1 Stress Analysis of Cores Under Different Loads

2.1.1 Drill Bit Loading

Closed form solutions for equilibrium equations of linear, isotropic materials subjected to the uniformly distributed circular loading, i.e., drill bit load of 15,000 lbs or equivalent pressure of 474.5 psi, on a semi-infinite space are obtained in the Papkovich and Neuber solution form. Additional details regarding this can be obtained from Reference 11.

2.1.2 Foam Pressure

Stress fields due to the horizontal pressure on the bore hole wall and the vertical pressure on the bore hole base are induced from the foam circulation. Once again the elastic solution in the Papkovich and Neuber form is applied for the vertical foam pressure while the horizontal

foam pressure on the surface is considered to be acting as a thin layer around the circular hole. The pumping pressure, according to the Christensen Co., is taken as 333 psi for 3,000 ft.

2.1.3 Overburden Pressure

After coring of formation, the stress field around the cored zone is altered because of the removal of the extracted material. Horizontal stresses of magnitude $(\nu/1-\nu)\sigma_v$ are produced for a horizontally confined cube of element that has a Poisson' ratio of ν and stress σ_v along the vertical direction. Once again, the Papkovich and Neuber form of solution is applied to obtain the stresses due to overburden pressure in the vicinity of the cored out region. A value of 1.0 psi per foot depth is taken as the overburden pressure for our investigations, herein.

2.1.4 Tectonic Stresses

The unknown tectonic stresses A_x and B_y induce the following stress distribution (7) on the coring surface.

$$\left.\begin{aligned}
\sigma_\rho &= \left(\frac{A_x + B_y}{2}\right)\left(1 - \frac{r_w^2}{\rho^2}\right) + \left(\frac{A_x - B_y}{2}\right)\left(1 + \frac{3r_w^4}{\rho^4} - 4\frac{r_w^2}{\rho^2}\right)\cos 2\psi \\
\sigma_\psi &= \left(\frac{A_x + B_y}{2}\right)\left(1 + \frac{r_w^2}{\rho^2}\right) - \left(\frac{A_x - B_y}{2}\right)\left(1 + \frac{3r_w^4}{\rho^4}\right)\cos 2\psi \\
\sigma_{\rho\psi} &= \left(\frac{B_y - A_x}{2}\right)\left(1 - \frac{3r_w^4}{\rho} + \frac{2r_w^2}{\rho^2}\right)\sin 2\psi
\end{aligned}\right\} \quad (2.1)$$

where σ_ρ, σ_ψ and $\sigma_{\rho\psi}$ are the radial, circumferential and shear stresses, respectively;

r_w = bore hole radius and ρ = distance from the vertical axis of the core

2.1.5 Resultant State of Stress

The resultant state of stress can be obtained by superimposing the stress fields corresponding to the above loading conditions.

$$S_{total} = S_b + S_f + S_o + S_{Ax} + S_{By} \tag{2.2}$$

where S_b are the stresses due to the drill bit loading

S_f are the stresses due to the foam pressure

S_o are the stresses due to the overburden pressure

and S_{Ax} and S_{By} are the stresses due to tectonic stresses in the x- and y-directions.

The maximum and minimum horizontal stresses are

$$S_1 = \frac{\nu}{1+\nu}\sigma_v + A_x \text{ and } S_2 = \frac{\nu}{1+\nu}\sigma_v + B_y \tag{2.3}$$

The three-dimensional Mohr's circle representation related with the fracture angle and the internal friction coefficient is used to predict the allowable range of stresses for fracture initiation in the core. Assuming the validity of the Coulomb-Navier theory of failure, a radius is drawn at the angle 2θ on the circle to the point B (Figure 2.1); the projection of this point on the σ and τ axes gives the magnitude of normal and shear stresses acting on the failure plane. The angle of

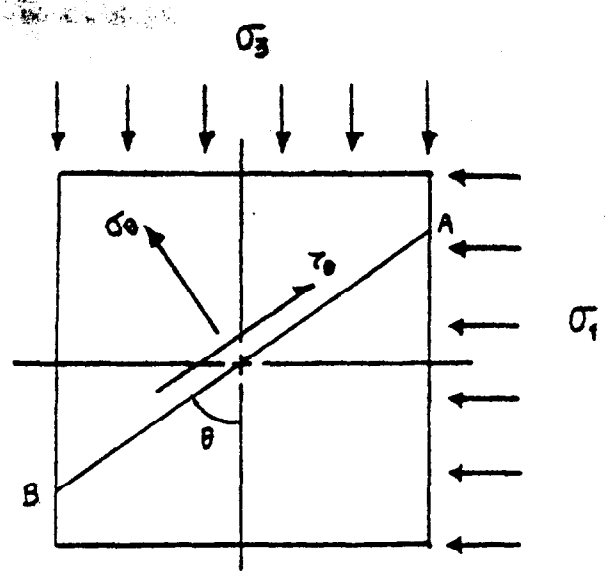

a) $\overline{AB}$ = Fracture Plane

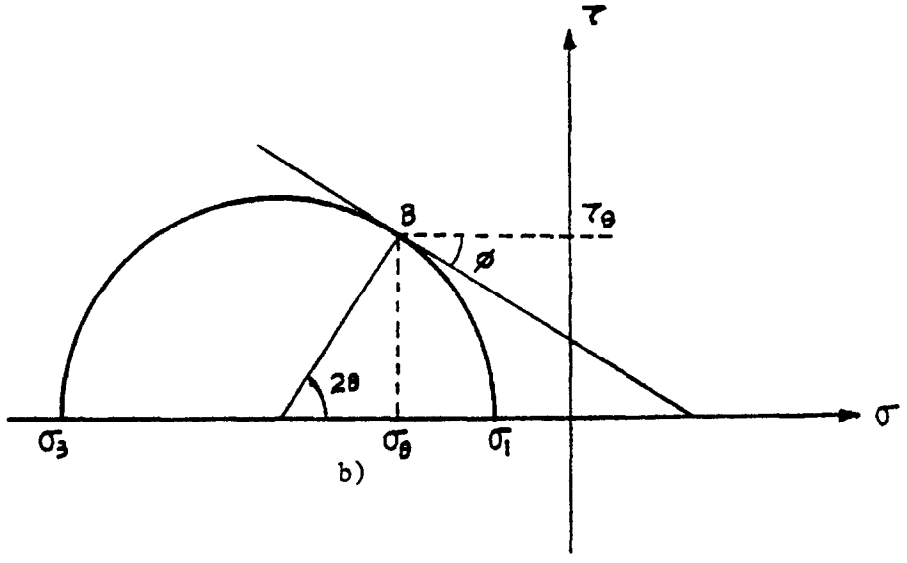

b)

Figure 2.1

a) Principal Stresses Acting on an Element
b) Three Dimensional Mohr's Circle Representation

internal friction ϕ is formed by the tangent to the circle at B and the direction of the σ axis, and the coefficient of internal friction μ can be calculated from $\tan 2\theta = \frac{1}{\mu}$

$$\text{where } \phi = 90^{\circ} - 2\theta \text{ or } \tan 2\theta = \cot \phi \qquad (2.4)$$

The range of the internal friction coefficient for rocks has been reported by Brace (3). He indicated two different ranges of μ, namely, 0.9 to 1.5, which coincides with the modified Griffith theory, and a range of 0.6 to 1.2 with Jaeger's experiments (9). The range of μ between 0.6 and 1.5 is employed herein to investigate the sensitivity of the possible tectonic stress combinations.

Therefore, combinations of tectonic stresses or in situ stresses which satisfy the above conditions can be determined by selecting different values of A_x and B_y under the following constraints: (1) the ratio of the in situ stresses varies between 0.5 and 2; (2) the in situ stresses can not be more than the overburden pressure.

2.1.6 Effect of Pore Pressure

The mechanical and transport properties of Devonian shale are strongly affected by the cavities and natural fissures in the shale. There is some evidence that these voids may have been interconnected and persist to a considerable depth. The cavities found in rock have been termed as cracks or pores depending on their shape.

A number of investigations on rocks have shown that fracture strength, frictional resistance and increase of strength with confining pressure depend on the effective stress or effective pressure, defined as the difference between total stress and pore pressure. It has been shown (11)

that the pore pressure reduces the principal stresses so that the effective principal stresses σ_1' and σ_3' are

$$\sigma_3' = \sigma_3 - P_o$$

$$\sigma_1' = \sigma_1 - P_o \qquad (2.5)$$

2.2 Coring-Induced Fractures

In distinguishing the natural fractures from the coring-induced fractures, various fractography techniques are applied. Careful observations of existing cores reveal that the induced fractures appear to propagate in discrete steps as evidenced by the concave downward marks on the fracture plane. Hence, it is deduced that the fracture is driven ahead of the coring bit. The discing of core seems to be occurring after the petal and centerline fractures. A discussion of the phenomena of discing fractures is given by Obert and Duvall (14).

2.2.1 Fracture Angle Measurements

About 20 cores revealing the typical petal and centerline fracture patterns were selected and the Goniometer F8424 type was used to measure the fracture inclination. The samples that show distinct concave marks maintain almost the same angle up to a third of the radius of the core; then the angle becomes very steep and finally the fracture aligns itself with the vertical plane bisecting the core. The data presented in Tables 2.1 and 2.2 represent the variation in petal fracture initiation angles with depth.

TABLE 2.1. Initial Petal Facture Angles of Cores in Devonian Shales Measured for this Study

DEPTH (feet)	#12041 COTTAGEVILLE CO. W.V. ANGLE	DEPTH (feet)	#20402 LINCOLN CO. W.V. ANGLE
3546-3549	31°	3479-3482	32°
3546-3549	34°	3479-3482	28°
3551-3553	38°	3486-3488	33°
3559-3562	40°	3486-3488	35°
3559-3562	42°	3486-3488	39°
3583-3586	42°	3506-3509	40°
3606-3608	41°	3509-3512	35°
3614-3617	39°	3512-3515	32°
3618-3622	41°	3512-3515	28°
AVERAGE	38.67°		33.55°

UGR File #..
WVU College of Eng.
1978

TABLE 2.2. Initial Petal Fracture Angles of Cores in Devonian Shales Measured by West Virginia Geological Survey

DEPTH (ft)	#12041 COTTAGEVILLE CO., WV ANGLE	DEPTH (ft)	#20402 LINCOLN CO., WV ANGLE
2500-3509	31.15°	3500-3509	26.92°
3510-3519	29.78°	3510-3519	31.14°
3520-3529	31.84°	3520-3529	30.56°
3530-3539	28.57°	3530-3539	26.92°
3540-3549	30.79°	3540-3549	33.40°
3550-3559	29.83°	3550-3559	33.00°
3560-3569	30.13°	3560-3569	28.68°
3570-3579	30.25°	3570-3579	29.69°
3580-3589	29.00°	3580-3589	30.00°
3590-3599	29.33°	3590-3599	--
Average	29.97°	Average	30.03°
DEPTH (ft)	**#20338 WISE CO., VA ANGLE**	**DEPTH (ft)**	**#20402 LINCOLN CO., WV ANGLE**
4900-4909	48.93°	3000-3009	36.67°
4910-4919	36.00°	3010-3019	35.00°
4920-4929	42.14°	3020-3029	32.03°
4930-4939	--	3030-3039	32.32°
4940-4949	52.22°	3040-3049	31.90°
4950-4959	47.44°	3050-3059	33.33°
4960-4969	45.00°	3060-3069	31.92°
4970-4979	48.50°	3070-3079	36.39°
4980-4989	45.00°	3080-3089	40.30°
4990-4999	--	3090-3099	32.91°
Average	45.65°	Average	34.28°

[illegible] Extension

[illegible]acture in solids is initiated by some flaw or imperfection such as microcrack which, like a notch, causes a high elevation of stress in that region. It has been shown that the crack tip stresses for plane stress or plane strain type problems can be expressed in terms of the stress intensity factors. These stress intensity factors are functions of crack dimensions and applied loads. This concept of stress intensity factors can also be associated with the idea of the strain energy release rate or crack extension force, which represents the loss of strain energy in cracked body as the crack advances by a short segment. While the determination of this energy release rate requires only the stress and displacement fields in a small zone around the crack tip, it can be related to the strain energy derivative v by the Griffith theory of energy balance which considers the system as a whole. The strain energy density approach advanced by Sih (17) is used, however, for this analysis. This method has been utilized by Advani et al. for hydraulic fracturing studies (1).

The two-dimensional model shown in Figure 2.2 is subjected to internal pressure, in situ stress and vertical stress. The strain energy density, S, for this model is expressed as a function of stress intensity factors k_1, k_2 and k_3.

The strain energy density factor S is expressed as a function of stress intensity factors k_1, k_2 and k_3.

$$S = a_{11}k_1^2 + 2a_{12}k_1k_2 + a_{22}k_2^2 \qquad (2.6)$$

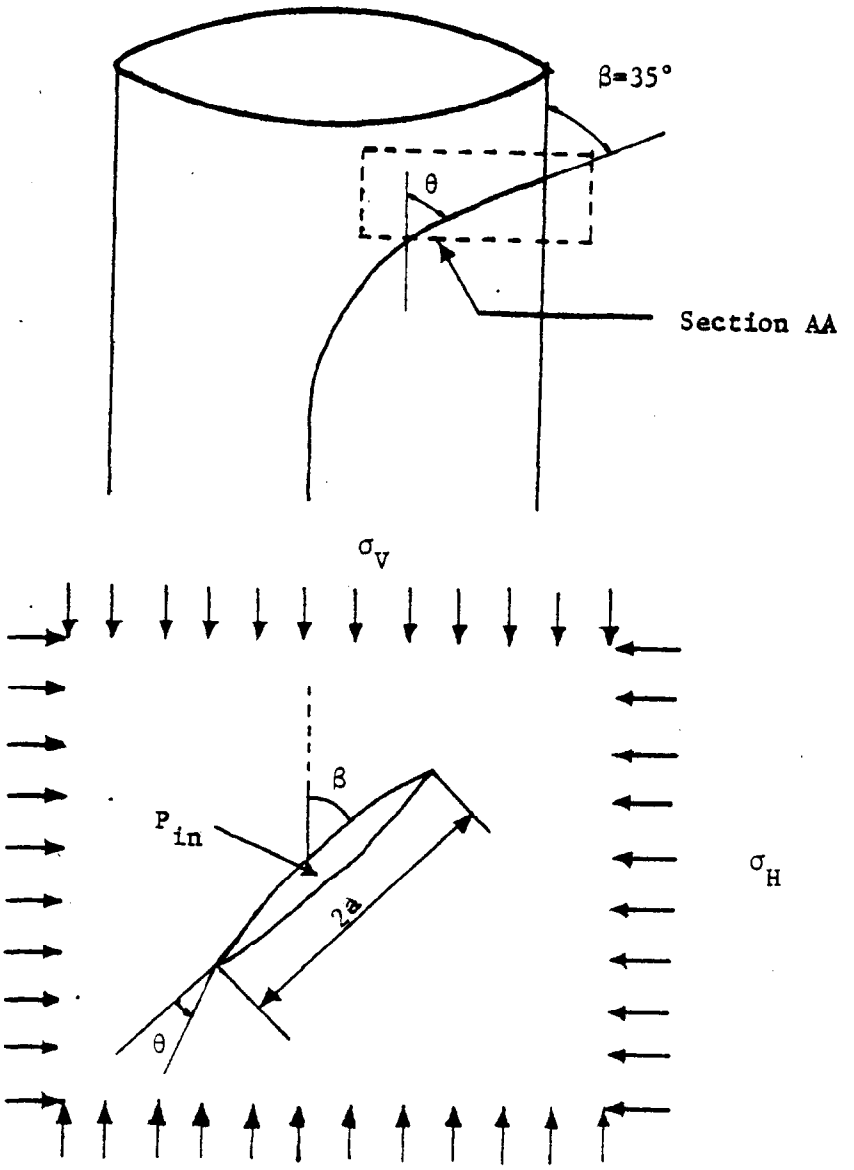

Figure 2.2

Two Dimensional Model With Inclined Crack

where $k_1 = (P_{IN} + \sigma_V \sin^2\beta + \sigma_H \cos^2\beta)\sqrt{A}$

$k_2 = (\sigma_V - \sigma_H) \sin\beta \cos\beta \sqrt{A}$

$a_{11} = \frac{1+\nu}{8E}(3 - 4\nu - \cos\theta)(1 + \cos\theta)$

$a_{12} = \frac{1+\nu}{4E} \sin\theta \, [\cos\theta - (1 - 2\nu)]$

$a_{22} = \frac{1+\nu}{8E} [4(1 - \nu)(1 - \cos\theta) + (1 + \cos\theta)(3\cos\theta - 1)]$

P_{IN} = internal pressure

σ_V = stress in vertical direction

σ_H = in situ stress

A = half length of crack

The crack starts to propagate with an angle θ (Figure 2.2). when

$$\frac{ds}{d\theta} = 0 \tag{2.7}$$

For stable crack growth, θ must satisfy

$$\frac{d^2S}{d\theta^2} \geq 0 \tag{2.8}$$

and

$$S \geq S_c \tag{2.9}$$

where $S_c = \frac{(1+\nu)(1-2\nu)}{2E} k_{1c}^2$ is the critical strain energy density,

and k_{1c} is the critical stress intensity factor which can be determined from experiments.

The critical pressure is obtained by setting $S = S_c$ in equation (2.6) and using equation (2.7) to obtain the fracture propagation angle θ_o by satisfying equation (2.8). For the centerline fracture stage, a simple vertical fracture criterion is used, i.e., the internal crack pressure is at least equal to the smallest compressive in situ stress for vertical fracture propagation.

2.2.3 Idealization of Fracture Patterns

A typical induced fracture of the extracted core is given in Figure 2.2. For analytical purposes, the actual fracture pattern is idealized by assuming two stages of fracture: (1) fracture initiation on the peripheral surface of the core at an angle β with the azimuth; and (2) subsequent downward propagation at an angle θ (less than β) and final termination in the vertical direction.

Having established the fracture patterns and magnitudes of initial angles (β), the Mohr-Coulomb theory for shear failure is applied in understanding the fracture initiation concepts. Also, stress intensity concepts are employed to predict the propagation angle θ for the second stage of fracture.

3. IN-SITU STRESS DETERMINATION BASED ON FINITE ELEMENT METHODS AND FRACTURE THEORY

The finite element method has become popular with the increasing use of high-speed electronic digital computers and growing emphasis of numerical methods for engineering analysis. Because of its broad applicability towards practical applications, the finite element method is employed herein, to solve the problem of stress distribution within rock formations. In-situ stresses are computed by utilizing the stress induced fracture angle (measured by goniometer) of the drilled-out core, the stresses obtained from the finite element analysis and the basic failure criteria. The details of this approach are described below.

3.1 Finite Element Modeling

Since the geometry of the field and the loadings is assumed to be symmetrical with respect to the horizontal axis x and y (Figure 3.1), only a quadrant of the model is analyzed to improve the computational efficiency and reduce the costs.

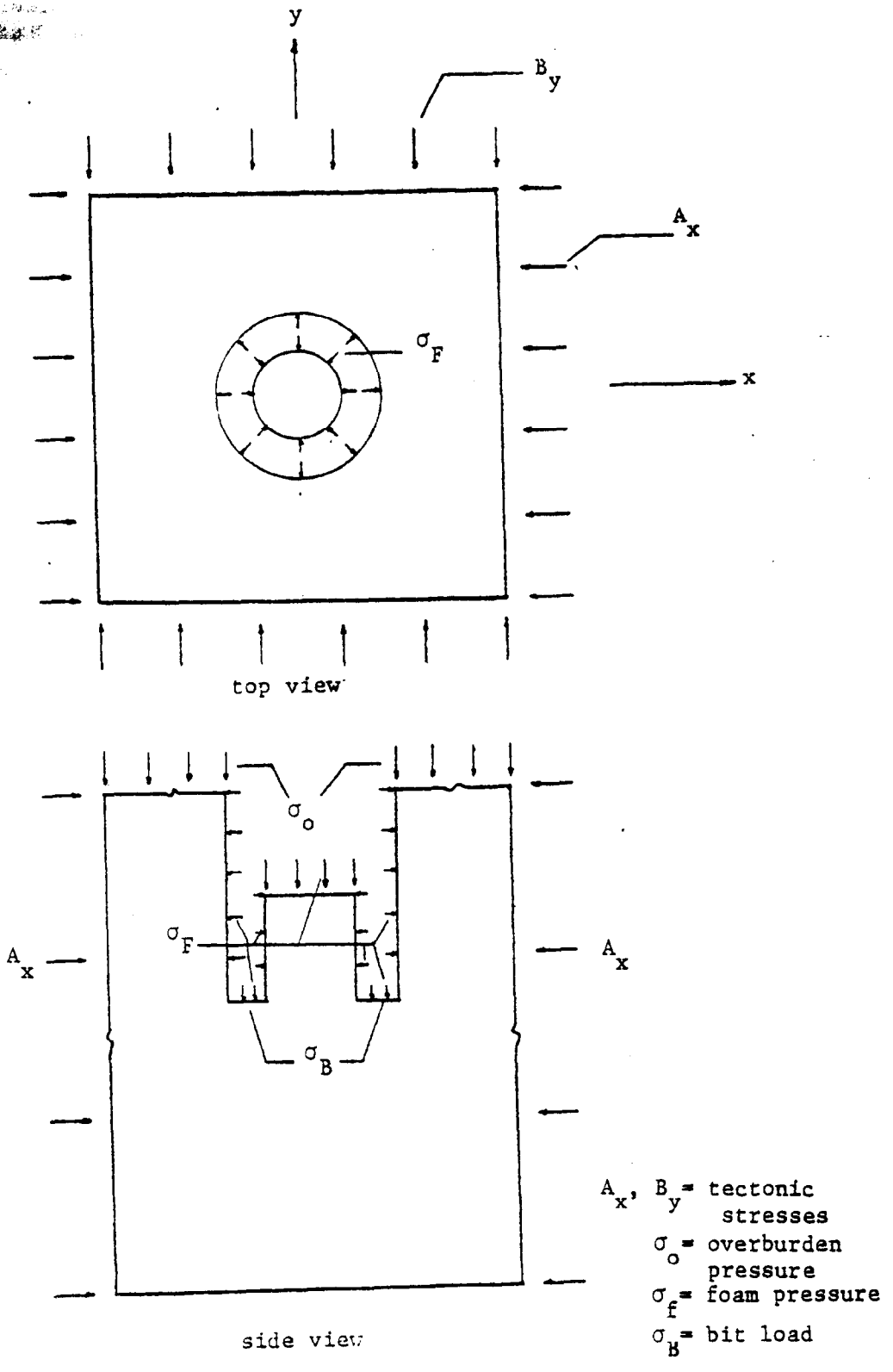

FIGURE 3.1. Different Stresses Acting on a Core Located in an Infinite Mass

By using the canned computer code (NASTRAN), 2 three-dimensional models, i.e., coarser and finer grid patterns (Model I in Figure 3.2 and Model II in Figure 3.3) are studied for linear isotropic and homogeneous material properties. Also, 2 two-dimensional models (Models III and IV in Figure 3.4) are investigated for transversely anisotropic and isotropic material conditions. The elastic constants for the three-dimensional isotropic models are taken as $E = 5 \times 10^6$ psi, $\nu = 0.2$. However, for Model III, i.e., transversely anisotropic model, the materials with mutually orthogonal planes of elastic symmetry have the following properties: $E_x = E_y = 5 \times 10^6$ psi; $G = 2.32 \times 10^6$ psi; $E_z/E_x = 1.3$ and $\nu = 0.2$. E_z is taken as constant, since the analysis is conducted within a given stratum (Devonian shale). Even though it is well known that the material properties of rocks vary somewhat in two mutually perpendicular directions (anisotropic in nature), it is assumed that both x and y axes are treated as the axes of symmetry, and further simplification is obtained by introducing that through each point of a body that passes a plane in which all directions are elastically equivalent.

The material properties and elastic constants used for each model are listed in Table 3.1. It should be noted that the tectonic stress in one of the two directions is ignored in the two-dimensional model.

From equation (2.3) and the constraints imposed on the magnitudes of tectonic stresses (A_x and B_y), their values are found to be less than 2250 psi at 3,000-ft depths for $\nu = 0.2$. The above statement is valid for conditions wherein the in situ stresses are smaller than the overburden pressure which is of the order of 3000 psi at 3,000-ft depths. By varying the values of A_x and B_x from 100 psi to 2200 psi with 100-psi increments, the stress distribution around the vicinity of the core is

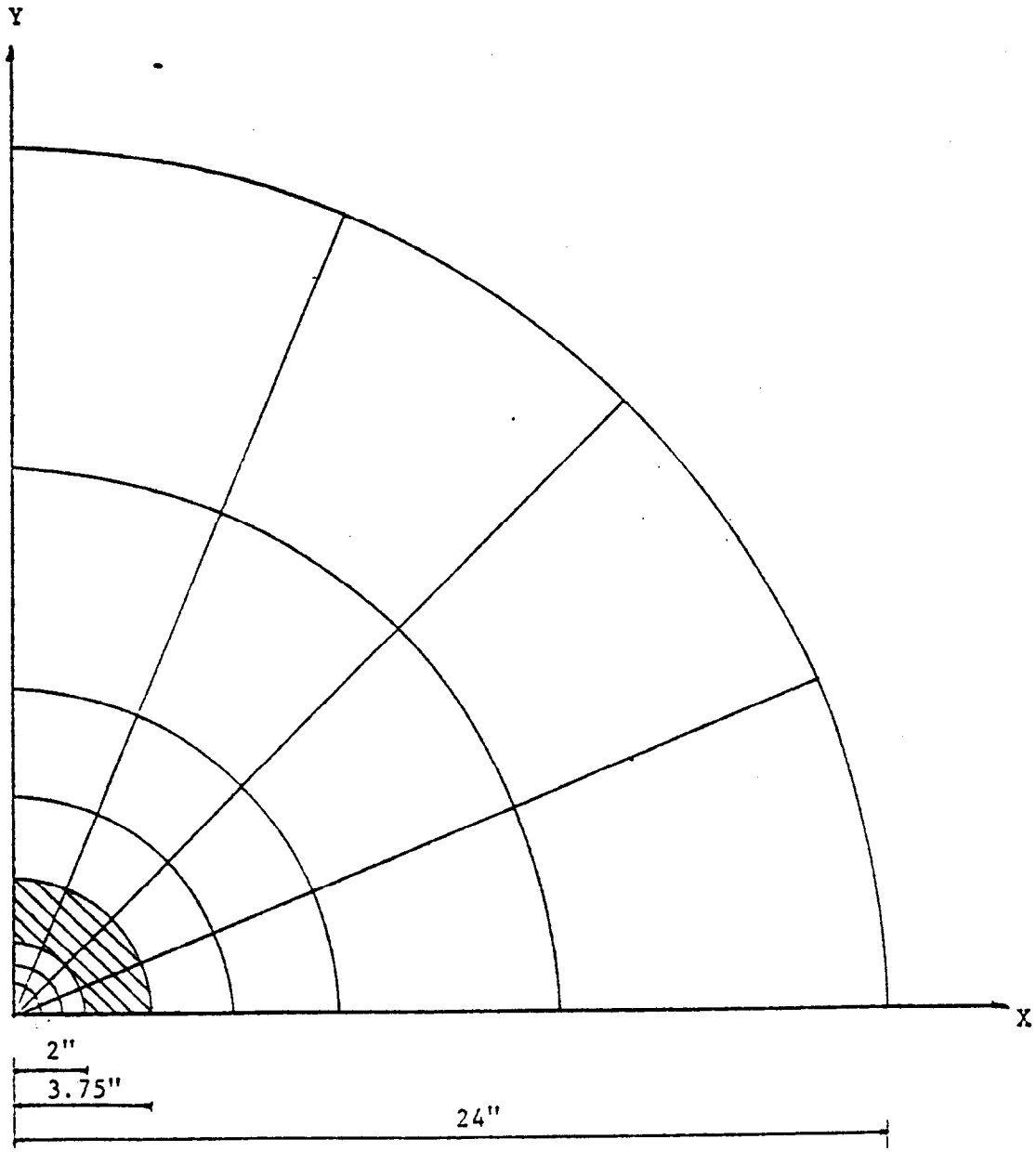

FIGURE 3.2 (a). Top View of Three-Dimensional Isotropic Model (I)

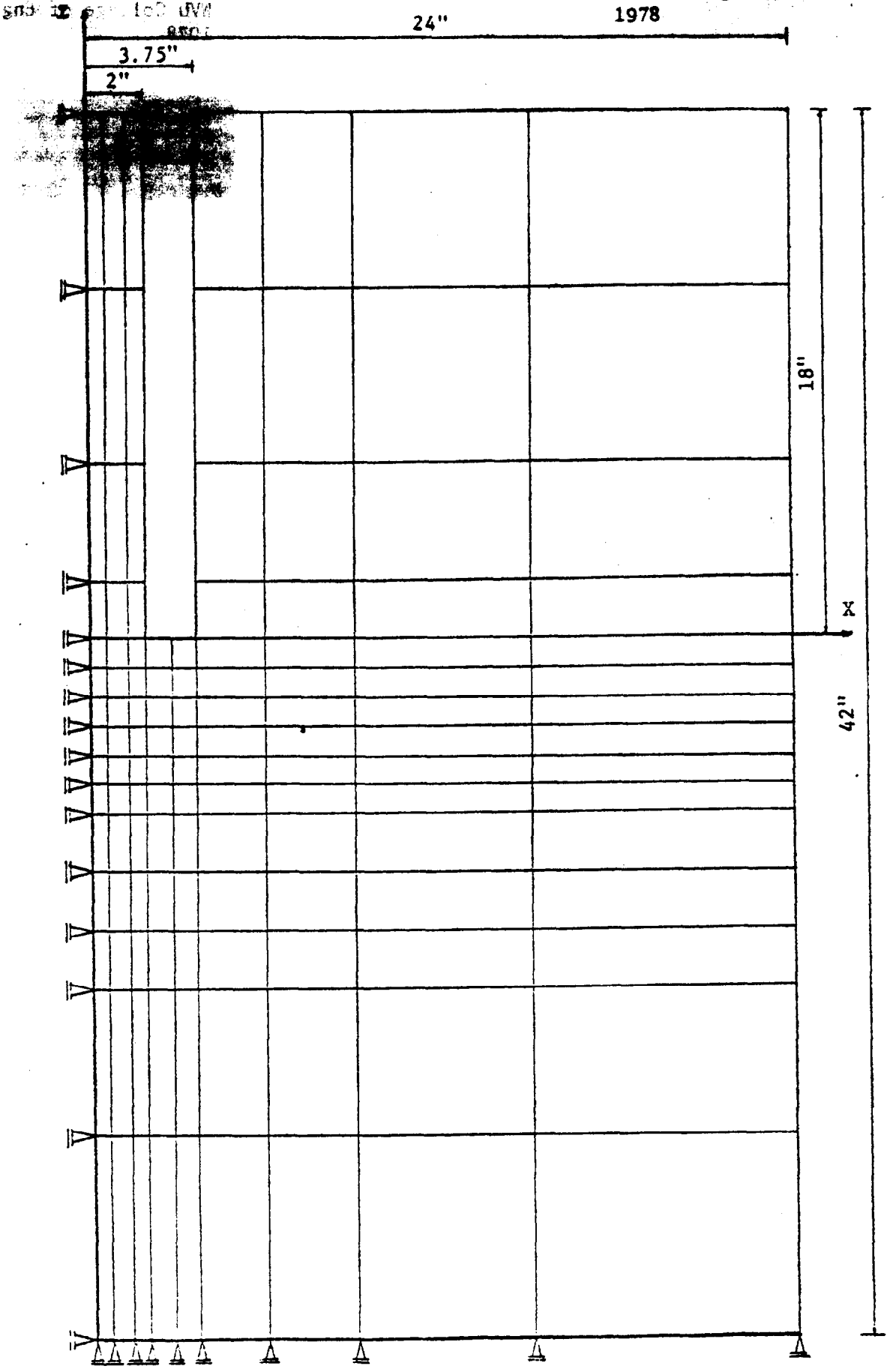

FIGURE 3.2 (b). Side View of Three-Dimensional Isotropic Model (I)

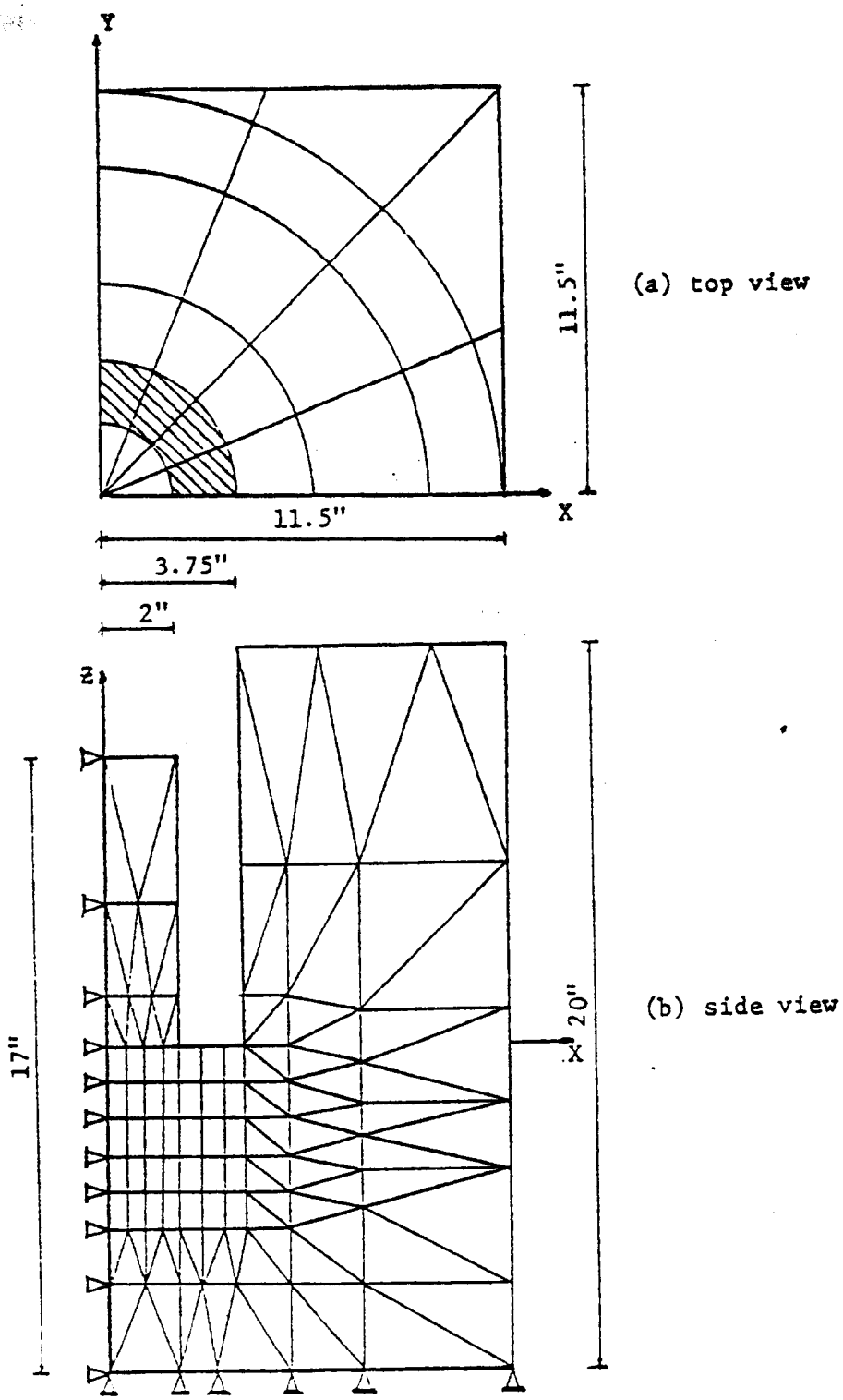

FIGURE 3.3. Three-Dimensional Isotropic Model (II)

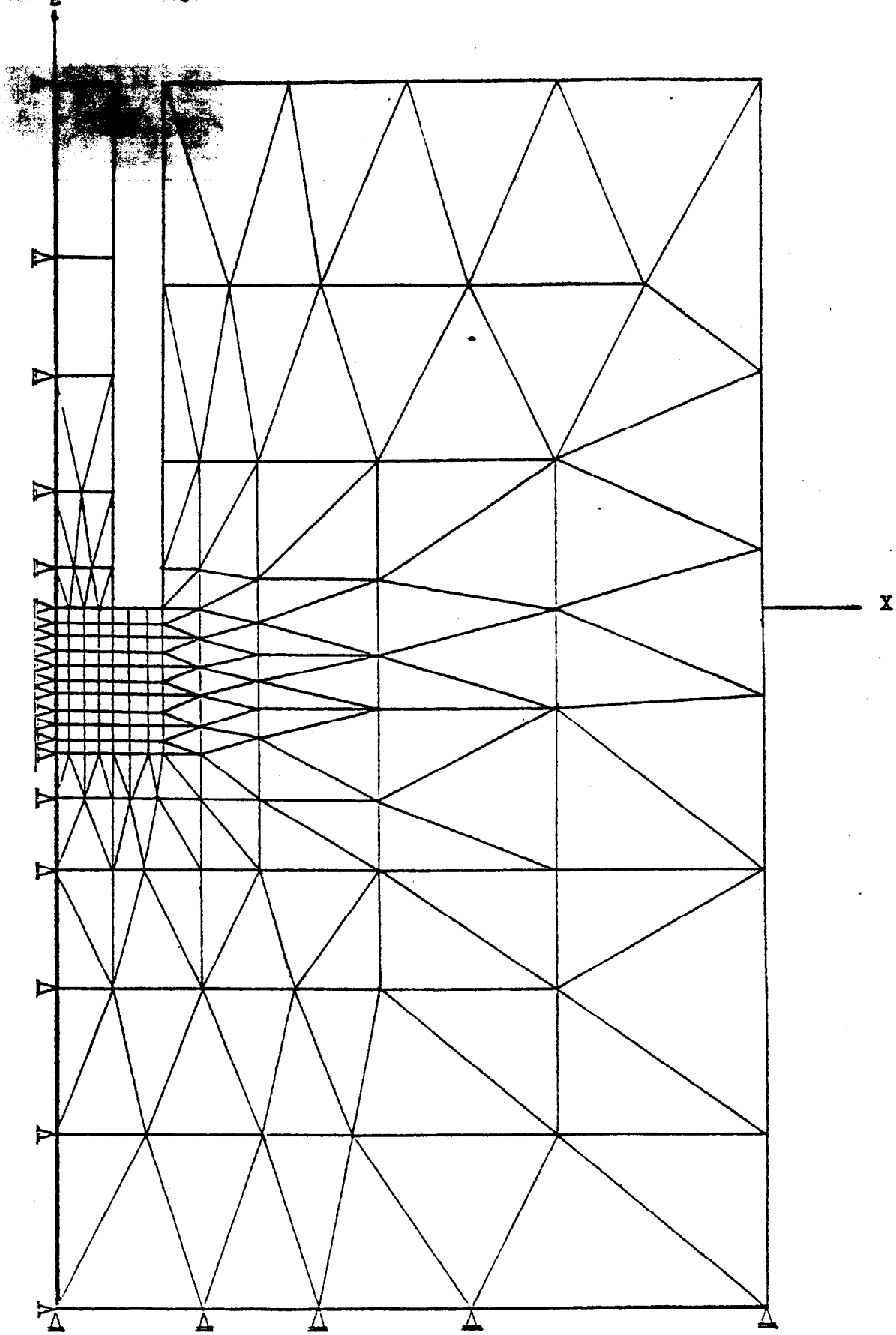

FIGURE 3.4. Two-Dimensional Anisotropic Model (III), Isotropic Model (IV)

TABLE 3.1. Characteristics of Finite Element Models

	MODEL I	MODEL II	MODEL III	MODEL IV
TYPE OF MODELS	3-D	3-D	2-D	2-D
MATERIAL PROPERTIES	LINEAR ISOTROPIC HOMOGENEOUS	LINEAR ISOTROPIC HOMOGENEOUS	LINEAR ANISOTROPIC HOMOGENEOUS	LINEAR ISOTROPIC HOMOGENEOUS
ELASTIC CONSTANTS	$E_x = E_y = E_z = 5 \times 10^6$ psi $\nu = 0.2$	$E_x = E_y = E_z = 5 \times 10^6$ psi $\nu = 0.2$	$E_z = 5 \times 10^6$ psi $E_x = E_y$ $\frac{E_z}{E_x} = 1.3$ $\nu = 0.2$	$E_z = 5 \times 10^6$ psi $E_x = E_y$ $\frac{E_z}{E_x} = 1.0$ $\nu = 0.2$
EXPECTED LOCATIONS OF INITIAL FAILURES	BETWEEN r = 2.4375" and r=1.667" Z = 0.5"	BETWEEN r = 2.293" and r = 1.75" Z = 0.5"	---	---

UGR File #125
WVU College of Eng.
1978

obtained for different values of A_x and B_y.

The final state of stresses (located at r = 0" - 3.75" and z = 0" - 6", where r is the distance measured from the centerline of the core and z is the downward depth measured from the base of the well) is computed by superposing the stresses obtained from bit loading, overburden, foam pressure and tectonic stresses in the two horizontal directions.

3.2 Determination of Initial Fracture Angle

Since the normal and shear stresses of each element for different loadings are computed from the finite element method, the principal stresses and initial fracture angle for each element in the finite element model can be calculated by constructing the Mohr's Circle. The initial fracture angle obtained from the computer results is compared with the measured angles.

Mohr-Coulomb's theory (13) of failure postulates that the critical stress has reached or exceeded that value for a state of stress wherein a Mohr's Circle is scraping or cutting a prescribed envelope. This envelope, usually a parabola, is idealized by fixing the tensile strength of rock T_o (400 psi is taken based on experimental data) and drawing a straight line with an internal friction angle α which is computed from $\mu = \tan\alpha$, (Figure 3.5). The values of α are varied from 31° to 56° based on the variable internal friction coefficient of rock which is taken as 0.6 to 1.5 (3). Based on the Mohr-Coulomb theory, i.e., the Mohr's Circle tangent to the envelope, it is found that the material fails in a plane which makes an angle ϕ with respect to the minimum (compressive) principal stress (refer to Figure 3.5). Mohr-Coulomb's theory further indicates that the intermediate principal stress, σ_2, has no influence on

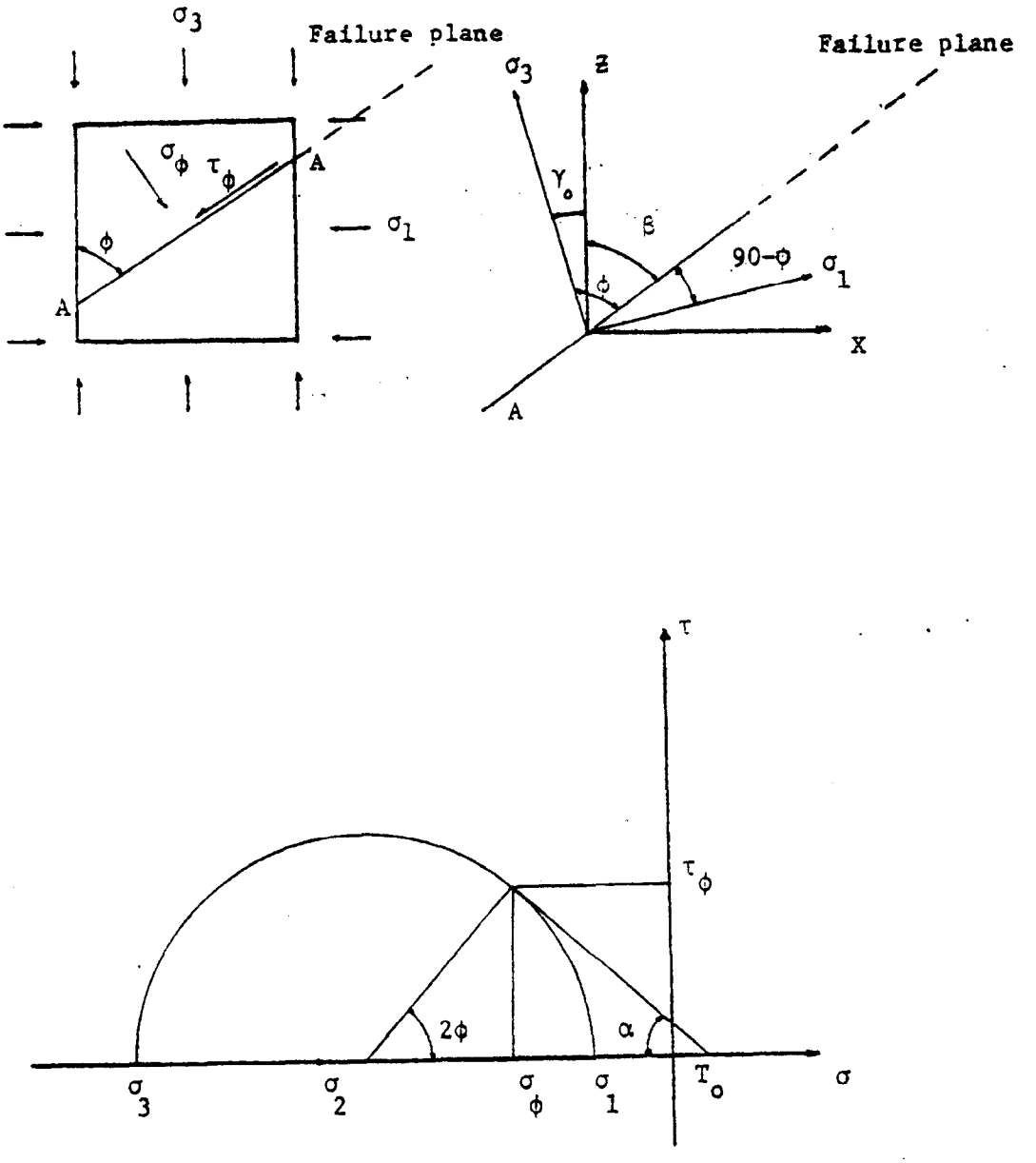

σ_2 lies between σ_1 and σ_3.

ϕ is measured normal to the failure plane. Hence $(90-\phi)$ is the angle between the failure plane and principal stress σ_1.

FIGURE 3.5. Mohr's Circle Indicating Mohr-Coulomb Criteria

failure.

The total stress that acts at any point on a plane of the saturated soil or rock can be divided into two parts, porewater pressure (neutral stress) and effective stress ($\sigma_1 - P_o$ and $\sigma_3 - P_o$, where P_o is the porewater pressure). It has been noted that the effective stresses can only induce changes in volume of a soil (or rock) mass (15). In other words, the effective stress can produce volume changes and hence create frictional resistance.

Since the principal stresses obtained in the above analysis correspond to total stresses, effective stresses can be obtained by subtracting the porewater pressure from total stresses. This implies that the revised Mohr's Circle will be shifted to the right. Hence, the maximum and the minimum effective stresses are given by $(\sigma_1 - P_o)$ and $(\sigma_3 - P_o)$ where P_o is taken as 500 psi. The fracture angles for different combinations of A_x and B_y are computed from the Mohr-Coulomb theory through an in-house computer program.

The following trial and error procedure is applied to find the tectonic stresses:

(1) As shown in Figure 3.5, for a given tensile strength of rock, T_o, draw two straight lines, one with α equal to 31° and the other with α equal to 56°, which covers a broad range of internal friction coefficient.

(2) For a given value of A_x (ranging from 100 psi to 2200 psi at 100-psi increments), B_y is varied from 100 psi to 2200 psi at 100-psi increments. This yields 22 x 22 (= 484) combinations of principal stresses which are functions of the other loading conditions (bit load, foam pressure and overburden pressure). The final state of stress is obtained as given in equation (2.2).

(3) The principal stresses and direction cosines are calculated for each of the above 484 combinations. Based on these principal stresses Mohr's Circles are constructed.

(4) If any one of the Mohr's Circles falls between $\alpha = 31°$ and $56°$ (item 1) or tangential to one of these lines, then that combination of A_x, B_y would fall within the correct tectonic stress range as long as the computed initial fracture angle, β, is approximately equal to the measured initial fracture angle β_m. The computed initial fracture angle, β, is obtained by subtracting the angle between σ_3 and azimuth directions (γ_o) from the failure angle ϕ which is measured between σ_3 direction and the failure plane.

(5) Because the measured initial fracture angle, β_m, is at the peripheral surface of the core, i.e., r = 2.0", and the analyzed fracture angle is obtained on the basis of stresses at r = 2.4375" for Model I and r = 2.293" for Model II, the latter (β) should be slightly greater (say 1° - 5°) than the former angle (β_m). If the analyzed fracture angle, β, for a given set of A_x and B_y is slightly greater than the measured fracture angle, β_m, that combination of A_x and B_y can be considered as the one that satisfies all the observed and theoretical constraints, and the corresponding S_1 and S_2 are the possible in situ stress values.

The computed fracture angles are given in Table 3.2. Those values with the asterisks (*) in the tables are chosen to be the in situ stresses, by correlating the measured and computed angles because more than one set of in situ stresses for a given set of problem parameters is obtained from this analysis. For example, the average measured fracture angles at 3,000-ft depths is 34.28° (Tables 2.1 and 2.2). However, the computed

TABLE 3.2. Computed Initial Fracture Angles and Corresponding In Situ Stresses at 3000 ft

MODEL I r = 2.4375" Z = 0.5"				MODEL II r = 2.293" Z = 0.5"			
S_1 psi	S_2 psi	μ	β	S_1 psi	S_2 psi	μ	β
2350	2950	0.8	30.0°	2250	2750-2950	1.1-1.4	30.1°-31.6°
2450	2450-2950	0.6-0.7	31.9°-32.4°	2350	1950-2950	0.6-1.1	30.3°-32.3°
2550*	2550-2950	0.6-0.7	34.5°-35.0°	2450	1950-2950	0.6-0.9	32.7°-33.9°
2650*	2650-2950	0.6	36.8°-37.3°	2550*	1950-2950	0.6-0.8	34.4°-36.5°
2750	2650-2950	0.6	39.2°-39.7°	2650	1950	0.6	34.1°
2850	2050	0.6	34.3°	2650*	2050-2950	0.6-0.7	37.6°-39.0°
2850	2150-2950	0.6	39.5°-42.0°	2750	1950	0.6	32.2°
2950	2050	0.6	33.5°	2750	2050-2950	0.6-0.7	39.6°-41.3°
2950	2150-2950	0.6	40.3°-43.9°	2850	2050-2950	0.6-0.7	40.1°-43.4°
				2950	2050	0.6	39.7°
				2950	2150-2950	0.6-0.7	44.0°-45.3°

*possible combinations of in situ stresses that satisfy the observed and theoretical constraints

UGR File #125
WVU College of Eng.
1978

TABLE 3.2. Computed Initial Fracture Angles and Corresponding In Situ Stresses at 3600 ft (cont.)

MODEL I r = 2.4375" Z = 0.5"				MODEL II r = 2.293" Z = 0.5"			
S_1 psi	S_2 psi	μ	β	S_1 psi	S_2 psi	μ	β
3000	2500-3600	0.6-0.7	35.8°-36.6°	2800	3500-3600	1.2-1.3	35.2°-35.7°
3100*	2400-3600	0.6-0.7	35.8°-38.5°	2900	2300-3600	0.7-1.1	35.0°-36.7°
3200*	2400	0.6	36.2°	3000*	2300-3600	0.7-1.0	36.6°-38.0°
3200*	2500-3600	0.6-0.7	38.9°-40.4°	3100*	2300-3600	0.7-0.9	37.1°-39.9°
3300*	2400	0.6	36.3°	3200*	2300	0.7	36.8°
3300	2500-3600	0.6-0.7	29.9°-42.1°	3200	2400-3600	0.7-0.8	40.6°-41.9°
3400	2400	0.7	36.0°	3300	2300	0.7	35.4°
3400	2500-3600	0.6-0.7	40.6°-43.6°	3300	2400-3600	0.7-0.8	41.4°-43.6°
3500	2400	0.7	35.5°	3400	2400-3600	0.7	41.7°-45.2°
3500	2500-3600	0.7	41.0-45.1°	3500	2400-3600	0.7	41.4°-46.7°
3600	2500-3600	0.7	41.3°-46.4°	3600	2400-3600	0.7	40.6°-48.1°

*possible combination of in situ stresses that satisfy the observed and theorectical constraints

UGR File #125
NVU College of Eng.
1978

TABLE 3.2. Computed Initial Fracture Angles and Corresponding In Situ Stresses at 5000 ft (cont)

MODEL I r = 2.4375" Z = 0.5"				MODEL II r = 2.293" Z = 0.5"			
S_1 psi	S_2 psi	μ	β	S_1 psi	S_2 psi	μ	β
4250	3350-4950	0.7-0.8	40.1-41.1	4250	3150-4950	0.8-1.0	41.4-42.9
4350	3350-4950	0.7-0.8	40.9-42.3	4350	3150-4950	0.8-1.0	41.8-44.2
4450	3350-4950	0.7-0.8	41.6-43.5	4450	3150-4950	0.8-0.9	41.9-45.3
4550	3350-4950	0.7-0.8	42.1-44.6	4550*	3150-4950	0.8-0.9	41.8-46.4
4650	3350-4950	0.7-0.8	42.6-45.6	4650	3150	0.8	41.3
4750*	3350-4950	0.7-0.8	42.9-46.6	4650*	3250-4950	0.8	44.9-47.5
4850*	3350-4950	0.7-0.8	43.2-47.5	4750*	3250-4950	0.8	45.0-48.5
4950*	3350-4950	0.7-0.8	43.3-48.3	4850*	3250-4950	0.8	45.0-49.4
				4950	3250	0.8	44.7
				4950*	3350-4950	0.8	47.8-50.3

*possible combinations of in situ stresses that satisfy the observed and theorectical constraints

NYU College of Eng.
1978

fracture angles (34.4° - 36.5° and 37.6° - 39.0° for Model II, Table 3.2) are slightly greater than 34.28°. The corresponding in situ stresses range from 2550 psi - 2650 psi for S_1 and 1950 psi - 2950 psi for S_2. The same procedure is applied to other depths.

3.3 Determination of Propagation Angle

Once the initial fracture angle (β) is determined from the Mohr-Coulomb theory, the propagation angle (θ) in the second stage of the fracture process can be determined (refer to Table 2.5 of Reference 5) from Sih's theory (17), which is briefly described in the following paragraphs.

The Griffith concept of instability in solids was the first study that predicted the fracture strength of solids. The basic idea behind his theory is that a crack will begin to propagate if the elastic energy released by its growth is greater than the energy required to create the fractured surfaces. This theory can only treat problems with the crack lying in a plane normal to the applied stress. Hence, Sih (17) has proposed a theory of fracture based on the strain-energy-density concept which requires no calculation on the energy release rate and thus possesses the inherent advantage of being able to treat all mixed mode crack extension problems.

In practice, many of the embedded cracks or flaws have irregular shapes, and they are three-dimensional in nature. Because of the mathematical tractability of the two-dimensional theory of elasticity, the majority of the literature on crack analysis has been limited to two-dimensional problems only. Here, Sih's theory for two-dimensional analysis is employed for the prediction of the propagation angle of an

[redacted] source crack. This analysis is conducted by applying the [redacted] density criteria that is described in Chapter 2.

Incorporating the following data, that is representative of Devonian shales, stable propagation angles, θ_o, are computed.

Young's modulus = $E = 5 \times 10^6$ psi

Poisson's ratio = $\nu = 0.2$

Horizontal stress = $\sigma_H = -2{,}000$ psi

Vertical stress = $\sigma_V = -100$ psi to $-2{,}900$ psi @ 100 psi increments

Internal pressure = $P_{IN} = 0$ psi to -500 psi @ 100 psi increments

Initial fracture angle = $\beta = 35°$ to $45°$ @ $1°$ increments

Stress intensity factor = $k_{1c} = \frac{2000}{\sqrt{\pi}}$ psi $\sqrt{\text{in.}}$

Crack length = $A = 0.125$ in. - 1.0 in.

From the numerous results (θ_o) obtained for several sets of problem parameters given above (particularly σ_H obtained from failure theory and given in Table 3.2), values of θ_o that converge toward the vertical fracture are chosen to represent the correct failure phenomenon. Numerical values of θ_o satisfying the above criteria are given in Table 2.5 of Reference 5. It is concluded from the numerical evaluation of θ_o that θ_o increases with the increase of P_{IN}, remains constant for varying crack lengths and decreases for increasing vertical stress.

Certain stable propagation angle, θ_o, can be determined from the results (β, σ_H, σ_V, and P_{IN}) obtained from the analysis in the first stage of failure. This angle is used as the β angle in Equations (2.7) through (2.9) to determine the stable propagation angle of the second stage. It is found that θ_o converges to the final vertical orientation for correct tectonic stress combinations. The results based on this procedure are shown in Table 3.3. However, by properly incorporating a finite element with crack tip effects in the proposed analysis (which could not be done in this study), the in situ stresses can be calculated without resorting to the trial-and-error procedure, wherein two constraint conditions can be directly introduced to solve for the two unknown in situ stresses.

4. DISCUSSION

4.1 In Situ Stresses Based on Elastic Analysis

The in situ stresses for various combinations of problem parameters with predicted propagation directions have been presented in Sections 3.1 and 3.2 of Reference 11. Also, these results are graphically represented in Figures 4.1 through 4.6.

For example, Figure 4.3 reveals the possible in situ stress combinations for different values of internal friction coefficients and fracture angles with P_o = 500 psi and T_o = 700 psi. The mean value of the measured fracture angles (i.e., $\beta = 38°$) in Table 2.1 was selected to determine the upper and lower bounds of in situ stresses. Figures 4.1 through 4.6 indicate that the computed magnitude of S_2 for a given value of S_1 is very sensitive with respect to the fracture angle β and the solution for a specified β is not necessarily unique. Therefore, accurate measurements

TABLE 3.3. The Convergence of Propagation Angle

$\sigma_{H(psi)}$	$\sigma_{V(psi)}$	$\beta_{(degree)}$	$\theta_{o(degree)}$
-2000	-1000	35	30
-2000	-1100	35	28
-2000	-1300	35	23
-2000	-1600	35	14
-2000	-1800	35	7
-2000	-1900	35	4
-1800	-1000	35	28
-1800	-1000	28	25
-1800	-1000	25	23
-1800	-1000	23	22
-1800	-1000	22	21
-1800	-1000	21	20
-1800	-1000	20	20
-1800	-1000	19	19

A = 0.125" P = 400 psi

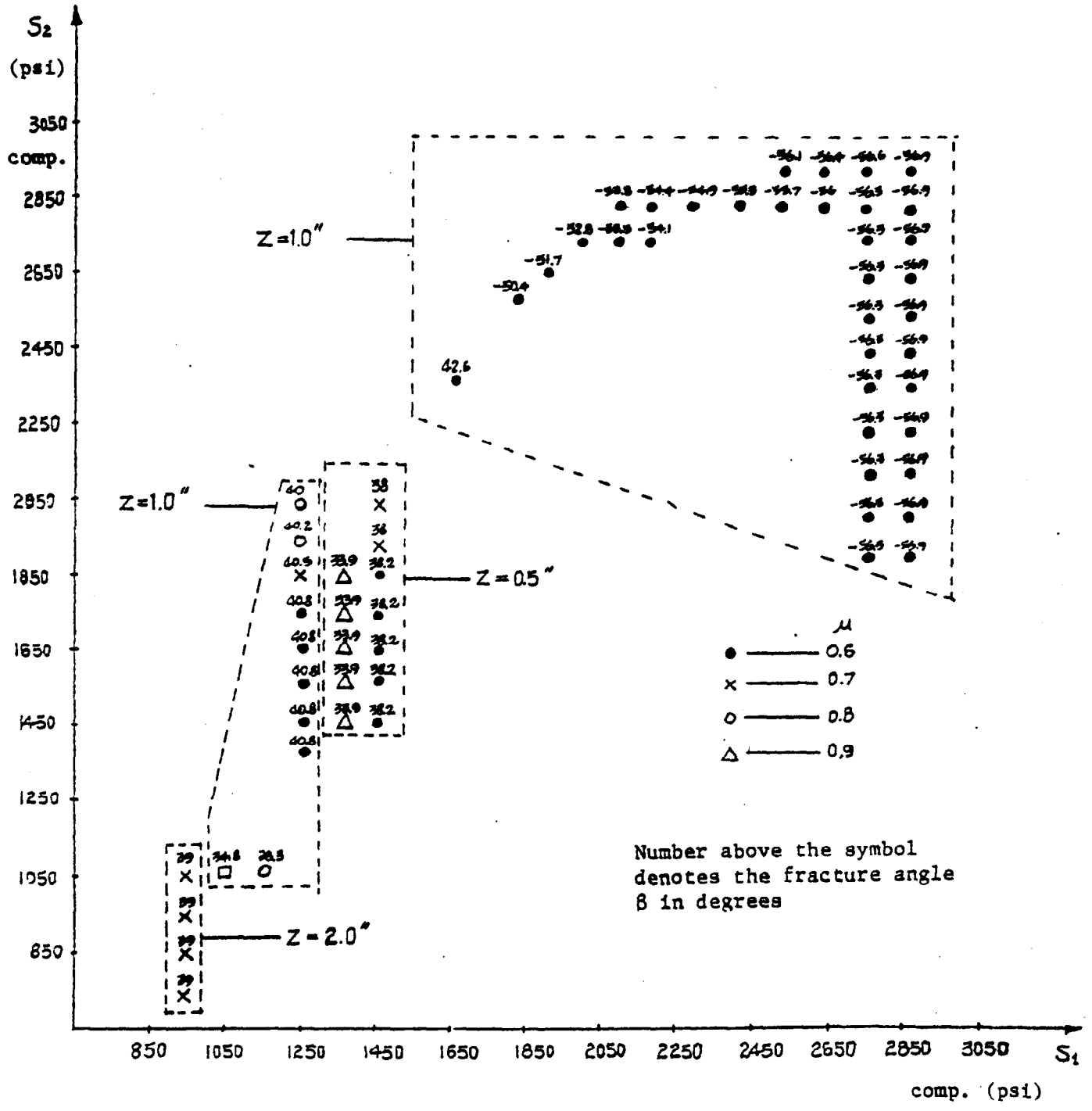

FIGURE 4.1. Possible In Situ Stress Combinations at Various Locations for P_o = 500 psi and T_o = 500 psi

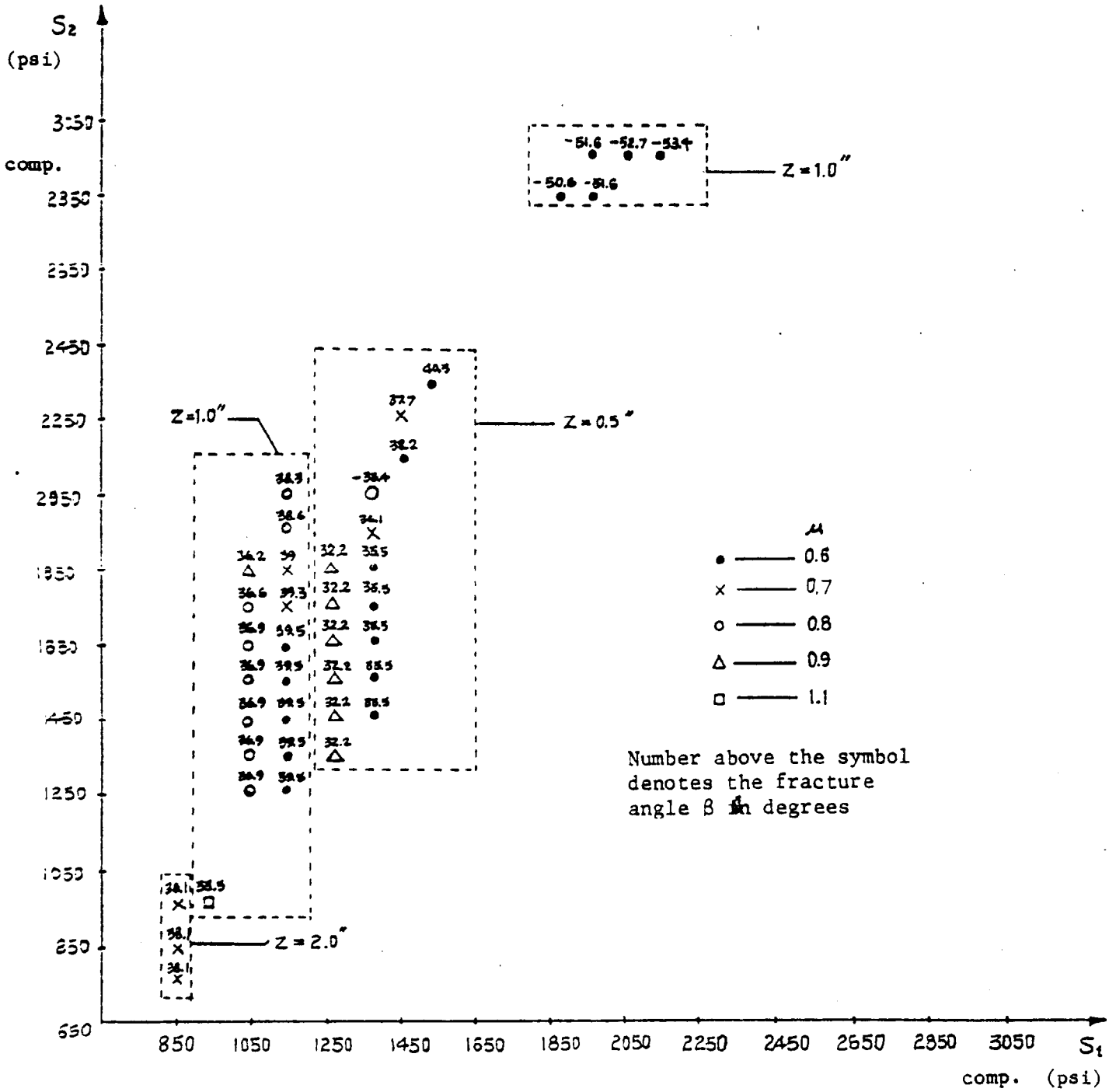

FIGURE 4.2. Possible In Situ Stress Combinations at Various Locations for P_o = 500 psi and T_o = 600 psi

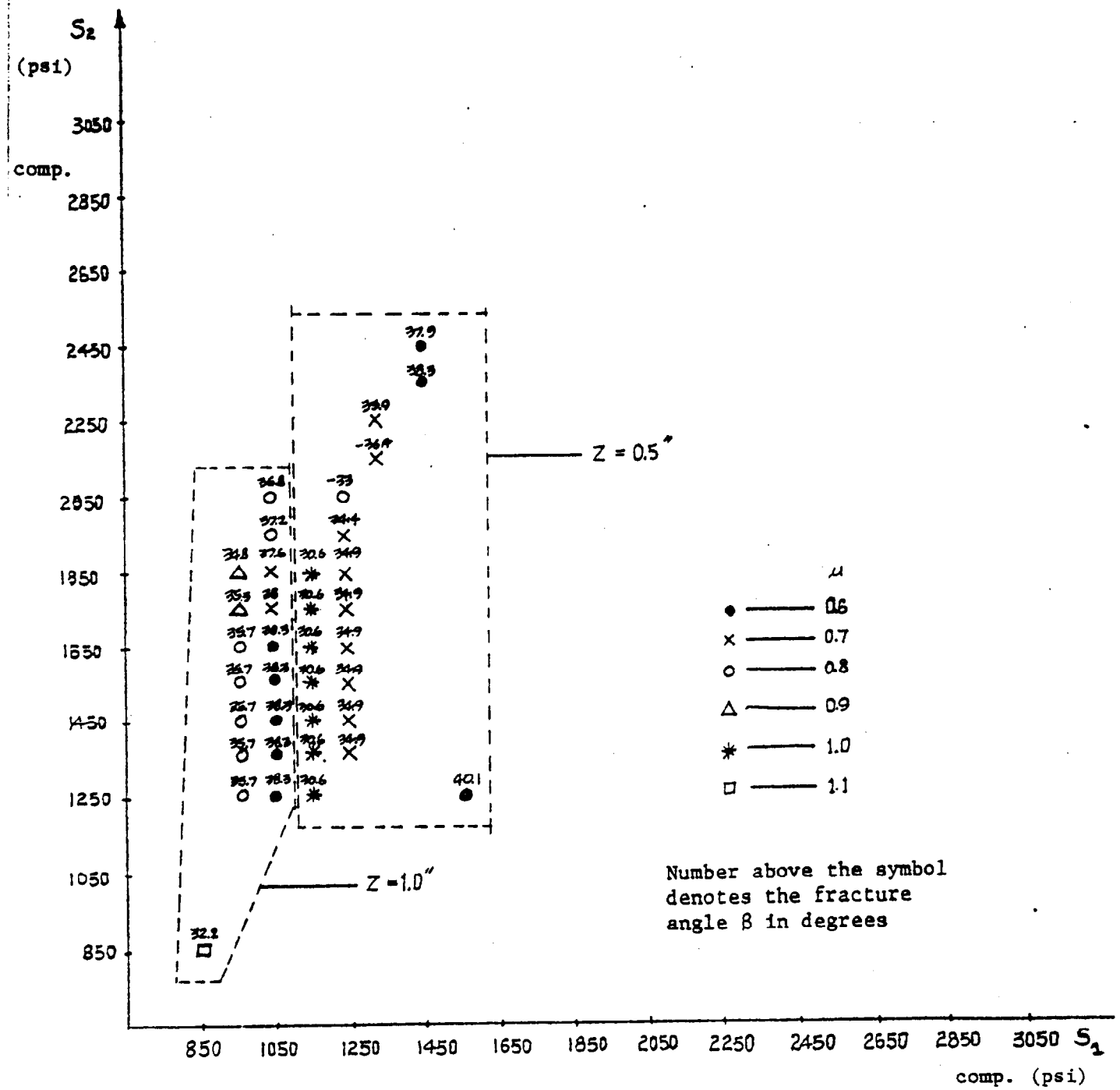

FIGURE 4.3. Possible In Situ Stress Combinations at Various Locations for P_o = 500 psi and T_o = 700 psi

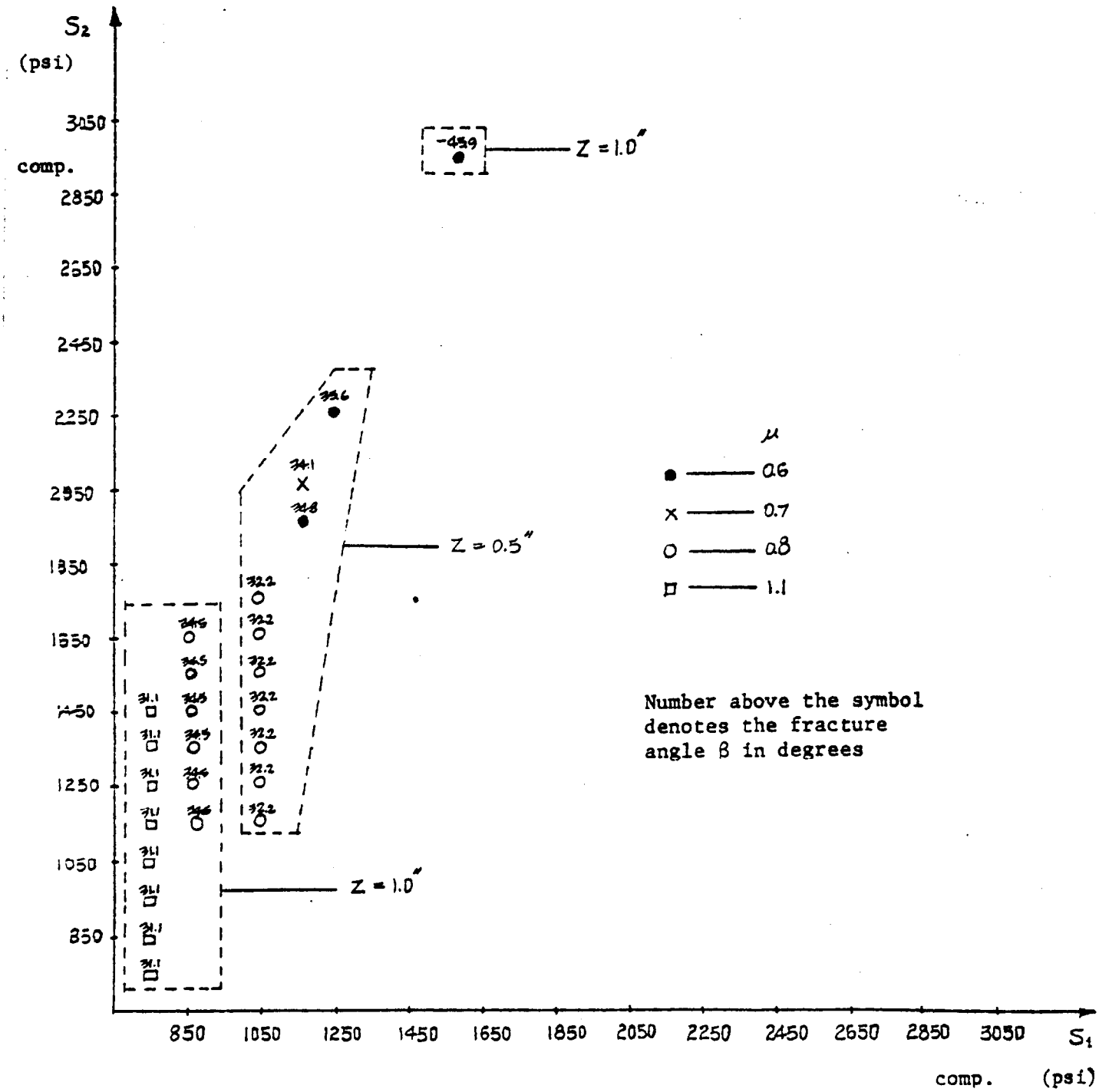

FIGURE 4.4. Possible In Situ Stress Combinations at Various Locations for P_o = 500 psi and T_o = 800 psi

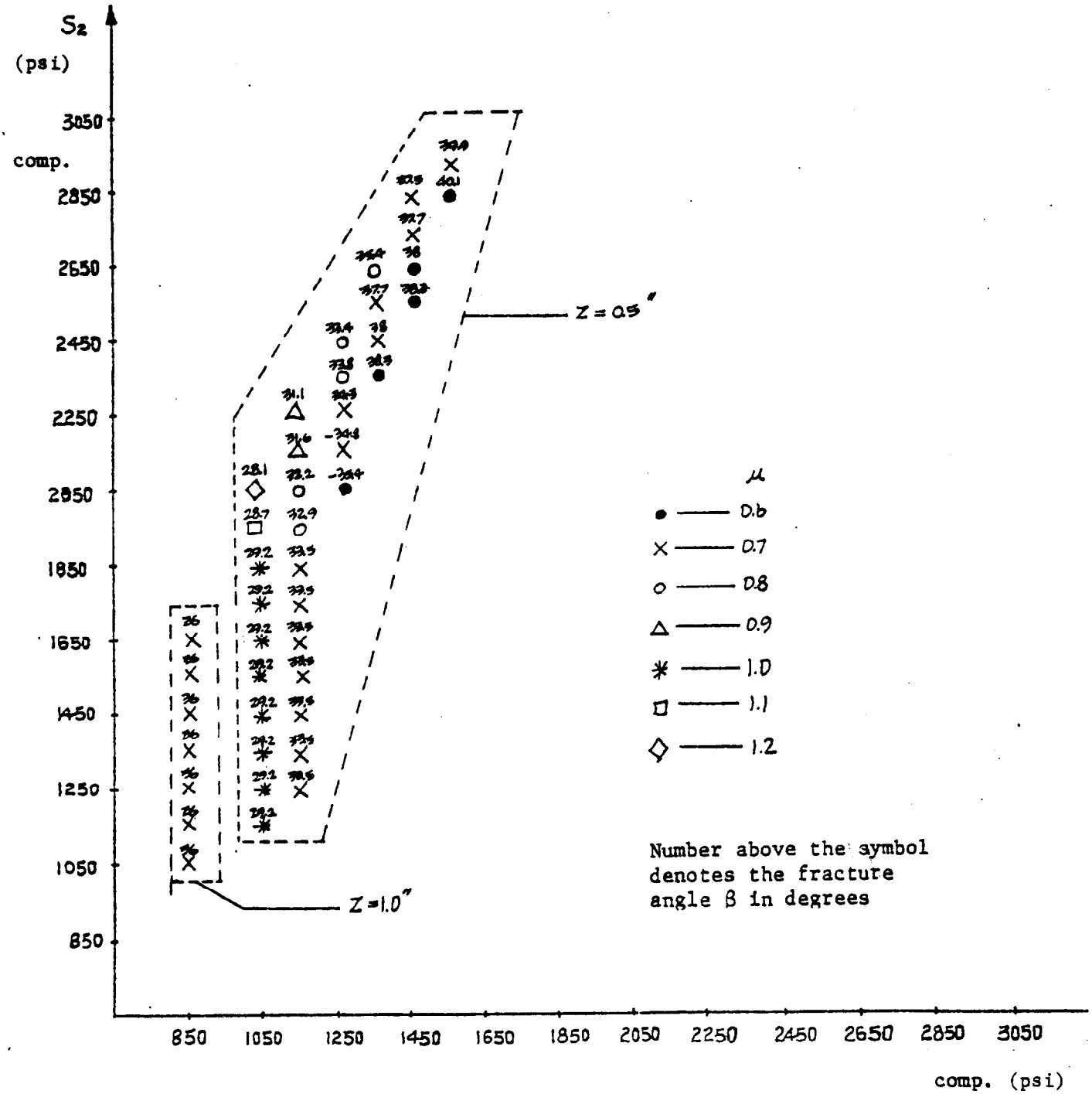

FIGURE 4.5. Possible In Situ Stress Combinations at Various Locations for P_o = 500 psi and T_o = 900 psi

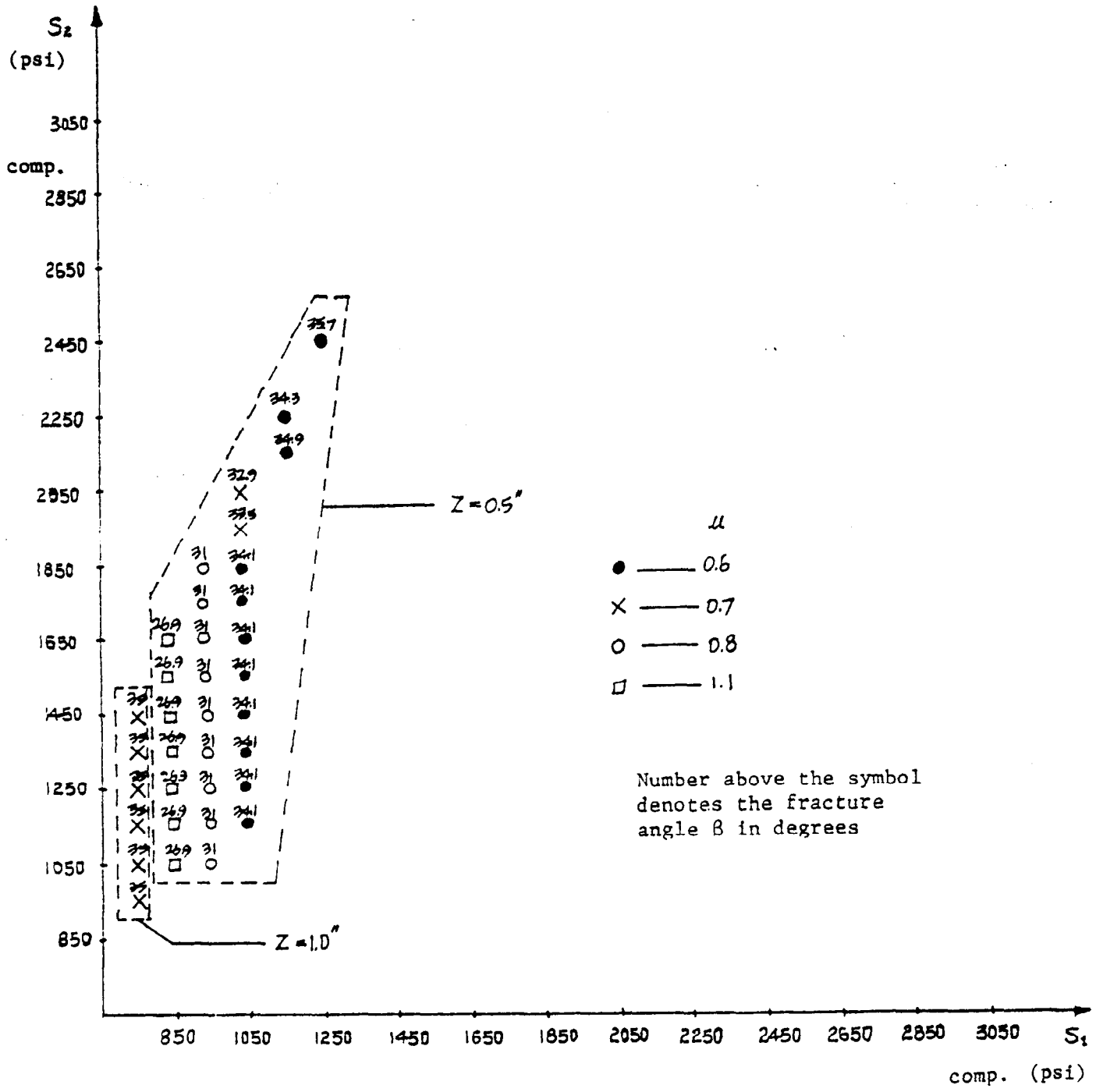

FIGURE 4.6. Possible In Situ Stress Combinations at Various Locations for P_o = 500 psi and T_o = 1000 psi

of the fracture initiation angles from the extracted cores and the appropriate selection of the in situ stress ratios provide reasonably good approximate in situ stress magnitudes.

Figure 4.7 reveals the fracture propagation direction and critical internal pressure for a line crack with $\beta = 38°$ and $A = 2$ in. as a typical case with the least compressive in situ stress $S_1 = -1450$ psi at $Z = 0.5$ in. and the corresponding value of $S_2 = -2450$ psi. This figure indicates that only for σ_v ranging from -250 to -1250, can realistic range of angle θ_o (i.e., $0 < \theta_o < \beta$) be predicted.
Also ,the fracture propagation angle θ_o tends to increase with the internal pressure. The vertical stresses are significantly altered by the induced loads, which indicates that the resulting vertical stresses are increasing faster than the other stresses as the depth increases. As a result, the analyses indicate that the vertical stress (σ_v) and the crack internal pressure, P_{IN}, are important factors in the fracture extension stage.

4.2 In Situ Stresses Based on Finite Element Methods

The analysis presented in Section 4.1 has considered the material as linear, isotropic and elastic medium. However, the geological formations, planes of weakness of rock, etc., have significant effects on the fracture responses. Hence, the finite element techniques are utilized to compute the stresses based on the anisotropic material properties.

4.2.1 Effect of Different Loadings on In Situ Stresses

The stress distributions under different loading conditions are computed through the finite element methods (NASTRAN) and are presented in Appendix C of Reference 5. It shows that the normal and shear stresses suddenly vary (jump) between r = 2.4375" and r = 3.3125" in Model I

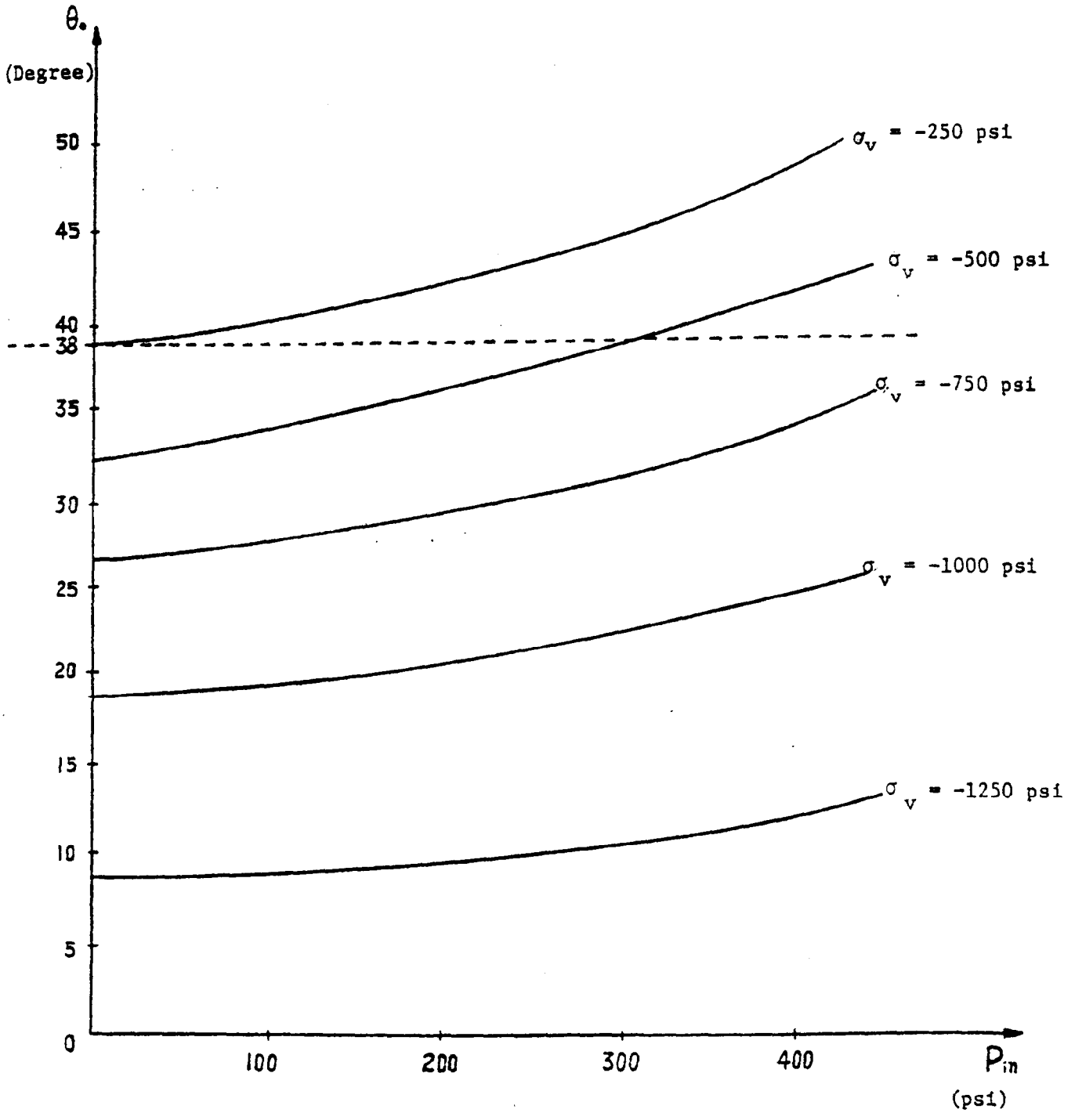

FIGURE 4.7. Fracture Extension Orientation for $\beta = 38°$ and $A = 2$ in.

(r = 2.293" and r = 2.875" of Model II) due to bit load. Besides, large tensile stresses are induced due to overburden, foam pressure and tectonic forces. Due to these induced tensile stresses of large magnitudes, the shear compression failure is more likely to take place because of the shift in the Mohr's Circle toward the right and its probability of intersecting the Mohr-Coulomb envelope becomes higher. Although no tensile stress occurs at the base of the cored cavity due to bit loading, the compressive stress in the z direction, i.e., σ_z, is quite large. This increases the radius of the Mohr's Circle and increases its possibility of intersecting with the Mohr'Coulomb envelope even for relatively smaller internal friction coefficients.

Stress distributions, computed from the finite element methods for isotropic and anisotropic two-dimensional models, are plotted in Figures C-16 through C-27 of Reference 5. The distribution patterns clearly reveal that they are nearly identical in shape and magnitude for isotropic as well as anisotropic material properties that are given in Table 3.1. Obvious extension of this study is to investigate the rock mass with three-dimensional anisotropic material properties and compare their results with the isotropic conditions.

4.2.2 First Stage Failure

The observed fracture angles, computed fracture angles and the corresponding in situ stresses are shown in Tables 2.1, 2.2 and 3.2. Through the results given in these tables, one can conclude:

(a) β, ranging from 30° to 46° for depths of 3,000 ft to 5,000 ft, increases with depth;

(b) Tectonic forces (A_x and B_y) increase with depth. It is assumed in our analysis that σ_v is greater than S_1 and S_2 for the Appalachian plateau. Based on this, our results are closer to Heim's hypothesis ($\sigma_v = c\gamma \cdot h$ and $S_1 \neq S_2 \simeq \sigma_v$) than the Tazaghi or Pascal theory.

The initial crack in the core has been assumed to be shear compression failure in this analysis and the Mohr-Coulomb theory is applied. However, strain energy failure criteria have to be employed also in analyzing the initial fracture and check the results with the initial angles of actual core fractures.

4.2.3 Second Stage Failure

The significance of σ_V, σ_H, and P_{IN} on the propagation angle, θ, has been studied. The propagation angle, θ, is found to be very sensitive to moderate variations in σ_V, σ_H and P_{IN}, whereas crack length has very little effect on the propagation angle.

It has been expected that the propagation angle, θ, in the second stage would converge from a certain magnitude of the initial fracture angle, β, towards the vertical fracture, $\theta = 0°$. Table 3.3 shows that the propagation angle, θ, does converge with increasing vertical stress, σ_V, while other variables are fixed. It also shows that, under certain conditions, θ converges from the initial value of 35°, to a final value of 20°. The angle does not converge any further while other variables remain constant. The possible explanation for this phenomenon is:

The vertical stress (σ_V) at the point in question before the fracture occurs (without crack) was obtained from the finite element analysis. This value has been used through the subsequent stages of fracture

propagation. However, the vertical stress would be much higher than the initial σ_V because of the stress concentration at the crack tip. Since the propagation angle converges to zero only for higher magnitudes of σ_V, a more realistic convergence of the propagation angle can be expected only by refining (increasing) σ_V at every stage through proper consideration of stress concentration effects. Also, it is likely that the magnitude of propagation angle, under certain field conditions, may never reach zero degrees even after meeting the above requirements. This phenomenon is being observed extensively in recent coring operations, i.e., θ may be of the order of 15° to 20° and never attained a perfect vertical failure.

Herein, the final check is to utilize the initial fracture angle and in situ stresses (or tectonic forces) obtained from the analysis of the first stage of fracture for the analysis of the second stage of fracture and determine the convergence of the propagating angle. If the propagating angle starts converging in the subsequent stages, it is concluded that the initially assumed stresses are considered as the practical tectonic stresses for the Appalachian region. It should be emphasized that this approach gives a certain range of stresses. However, our results indicate that the in situ stress range is <u>not</u> widely scattered and compares well with some of the existing information obtained from other techniques (4).

5. CONCLUSIONS AND RECOMMENDATIONS

5.1 Conclusions

A general approximate technique of determining in situ stresses by an easy, fast and economical approach has been presented, herein. Since

the rock cores are routinely extracted, no additional field work is needed in determining the in situ stresses. Hence, the associated costs of such operations are minimal. Also, difficulties related to the field instrumentations and measurements can be avoided.

The initial fracture angles of drilled-out cores at different depths, i.e., 3,000 ft to 5,000 ft, were measured toward this study. Those angles measured by the West Virginia Geological Survey were taken into account during this analysis. One of the most important observations of the initial fracture angle measurements indicates an increase in their magnitudes (30° - 45°) with the increasing depths.

The results of this study have established that the linear elastic theory and suitable fracture criterion can be applied to give possible estimates for in situ stresses from observed fracture patterns and initiation angles in Devonian shale cores. In particular, the three-dimensional Mohr's Circle representation with selected Coulomb internal friction coefficient yields reasonable fracture angle correlations with the field data.

Two three-dimensional finite element models (both isotropic, with different mesh sizes) and 2 two-dimensional finite element models (one isotropic and anisotropic) were developed to find the stress distributions and the effect of different loadings for a linear, homogeneous media. The results show that the relative effect of bit load on local stresses in comparison with the other loadings is negligible. However, Mohr-Coulomb's shear failure theory associated with the other loads indicates that the failure occurred on the periphery of the core and slightly ahead of the bit load. This may be due to the effect of stress concentration of the bit load, foam pressure and the presence of the drilling well.

A range of in situ stresses (S_1 = 2250 psi to 2650 psi and S_2 = 1950 psi to 2950 psi for 3,000-ft depths) is obtained by using the proposed approach as stated in Section 3. Also, Sih's strain energy density concept is employed to verify the in situ stresses obtained by Mohr-Coulomb failure criteria. However, this could not be successfully employed because the stress concentration effects at the crack tip are not accurately accounted for in our analysis because of the absence of built-in singularity element in the NASTRAN program. Obviously, high stresses near the crack tip influence the crack propagation. However, the derived values of in situ stresses are not widely scattered and compared well with some of the existing information (4).

5.2 Recommendations

To obtain more accurate results, the following aspects have to be carefully evaluated:

(1) Accurate measurement of initial fracture angles from the cores;

(2) Determination of dependable material property constants (Young's modulus, Poisson's ratio, Tensile Strength, Internal Friction Coefficient, Fracture Toughness and Porewater Pressure);

(3) Applications of exact loading conditions during the modeling;

(4) Refined failure criteria (example, parabolic) may be used in place of the specialized straight line envelope;

(5) Three-dimensional nonlinear, anisotropic material conditions;

(6) Property modeling based on finite element methods including special finite elements consisting of crack tip effects such as the approach developed by Wilson (16);

(7) Three-dimensional fracture theory for those source cracks with irregular shape.

6.0 REFERENCES

1. Advani, S. H., GangaRao, H.V.S., Shuck, L. Z. and Chang, H. Y., "Structural Response Governing Hydraulic Fracturing Operations in Rock Media," West Virginia University, 1975, pp. 3-21.

2. Bonnechere, F., "A Comparative Study of In-Situ Rock Stress Measuring Techniques," M.S. Thesis, U. of Minn., 1967.

3. Brace, W. F., "Brittle Failure of Rocks," International Conference on State of Stress in Earth's Crust, Santa Monica, Cal., 1963, pp. 111-174.

4. Brechtel, C. E., Abou-Sayed, A. S., and Clifton, R. J., "In-Situ Stress Determination in the Devonian Shales (IRA McCoy 20402) Within the Rome Basin," Terra Tek Report TR-77-36, 1976.

5. Chang, Patrick, "Determination of In-Situ Stresses Based on Finite Element Modeling," M.S. Thesis, Wet Virginia University, Morgantown, WV, Dec. 1978.

6. Fairhurst, C., "Methods of Determining In-Situ Rock Stresses at Great Depth," Technical Report No. 1-68 AD 665 994, U.S. Corps of Engineers, Missouri River Division, 1968, pp. 19-53.

7. Hamison, B. and Fairhurst C., "Initiation and Extension of Hydraulic Fractures in Rocks," Society of Petroleum Engineers Journal, V. 7, No. 3, September, 1977, pp. 310-318.

8. Hubbert, M. K. and Willis, D. G., "Measurement of Hydraulic Fracturing," Petroleum Transaction, Shell Development Co., 1957.

9. Jaeger, C., "Rock Mechanics and Engineering," Cambridge [Eng.] University Press, 1972, pp. 82-84.

10. Kehle, R. O., "The Determination of Tectonic Stresses Through Analysis of Hydraulic Well Fracturing," J. Geophysical Res. V. 69, No. 2, 1964, pp. 259-273.

11. Lee, Seong-Chul, "Investigation of Stress and Fracture Responses Associated with Coring Operations," M.S. Thesis, West Virginia University, Morgantown, WV, August 1978.

12. Leeman, E. R., "The Measurement of Stress in Rock," South African Inst. Min. & Met.-J V. 65 no. 2, 1964, pp. 45-114.

13. Liebowitz, H., "Fracture," V. VII, Academic Press, New York, 1972, pp. 123-129.

14. Obert, Leonard and Duvall, Wilbur I., "Rock Mechanics and the Design of Structure in Rock," John Wiley and Sons, Inc., New York, 1967, pp. 275-317.

REFERENCES (continued)

15. Peck, R. B., Hanson, W. E., and Thornburn, T. H., "Foundation Engineering," 2nd Edition, Wiley, New York, 1973, p. 44.

16. Potts, E. L. J., "Stress Distribution, Rock Pressures and Support Loads," Iron & Coal Trades Rev. V. 169 No. 4506, 1954, pp. 333-339.

17. Sih, G. C., "Methods of Analysis and Solution of Crack Problems," V. 1, Noordhoff International Pub., Leyden, 1973, pp. XXIII-XLIV.

18. Timenshenko, S. P. and Goodier, J. N., "Theory of Elasticity," McGraw-Hill Book Co. Inc., 1951, pp. 78-83.

APPENDIX A: METHODS OF DETERMINING IN-SITU ROCK STRESSES

Accurate methods for determining the state of stress at depth are not fully developed yet, even though the instruments for measurements are located at a distance away from the point being examined. A borehole has to be drilled nearer to the point in question to house the instruments. Before the introduction of the borehole, the state of stress is assumed to be the same at all points within a certain region, i.e. homogeneous. This is considered acceptable because of the absence of large geological inhomogeneities over a small region. This assumption leads to easier computation of the state of stress. Fairhurst classified the major methods (or instruments) of determining in-situ stress into five general categories: (6)

(1) Borehole deformation cells

(2) Borehole inclusion stress meters

(3) Borehole strain gauge devices

(4) Hydraulic jack method

(5) Hydraulic fracturing

In the following section, the first four methods are briefly stated. The hydraulic fracturing method is described in more detail, since it is considered to be the most readily adaptable method for the estimation of stress at great depths directly from the cells.

A.1 Borehole Deformation Cells (12,14)

A concentric cylindrical slot around the borehole is cut to remove the regional stresses. From the observation of the diametric deformation of the borehole, the stresses are calculated by using formulae

derived from the theory of elasticity.

The three usual assumptions are:

(1) The rock is isotropic and linearly elastic. Berry and Fairhurst[1] show that in some cases an error as much as 50% could be found due to the assumption of isotropy for those rocks (e.g. shale) which are, essentially, transversely anisotropic.

(2) The regional shear stresses parallel and normal to the axis of the hole have no influence on the diametric deformation of the hole. Leeman's suggestion that the regional shear stresses parallel and normal to the axis of the hole are zero, lacks adequate evidence from measurements made at depth.

(3) The borehole is drilled into the linearly elastic rocks before the regional stresses are applied, and a condition of plane stress or plane strain is sustained throughout the loading process. It is obviously not true that the stress parallel to the borehole is zero at depth. Besides, the horizontal stresses would certainly produce some strain in vertical plane. A more realistic assumption (6) is to consider simply that the independent regional principal stresses exist (no restriction is placed on their magnitudes, i.e. no plane stress or plane strain conditions are imposed) before the borehole is drilled.

This method is not suitable for deep hole stress determination due to the difficulty of inserting the tool, overcoring, recording the deformation, and removing the core intact from great depth.

A.2 Borehole Inclusion Stress Meters (12)

The feature which distinguishes a 'stressmeter' from a borehole deformation 'strain cell' is that the changes in strain in the former

are measured and expressed in terms of changes of stress in rock, while the latter measures actual deformations of the borehole in which the cell is installed.

Two kinds of inclusion stressmeters, high modulus meters and low modulus meters are being used today. The principle of the high modulus meters can be summarized as:

(1) If an elastic inclusion is 'welded' (no slight slip at all) into the rock, any change in stress in the rock will be accompanied by a proportional change of stress in the inclusion.

(2) As the ratio of the modulus of elasticity of inclusion to that of the rock exceeds 5, the stress in the inclusion is relatively unaffected by the changes in the modulus of the rock.

A lower value (relative to the rock) of modulus of elasticity of the inclusion is used for the so-called low modulus inclusion. Agarwal and Boshkov conclude that as the ratio E(i)/E(r) (the modulus of the inclusion E(i) to the modulus of the rock E(r)) approaches zero, the deformation of the inclusion upon overcoring will be the same as that of the open hole. This is true as long as it remains in contact with the hole without slipping.

The practical difficulties of achieving the 'welded' boundary conditions visualized in a stressmeter installed at the end of a long borehole drilled in rock, are very obvious. Therefore, it is not applicable to deep hole stress determination.

A.3 Borehole Strain Gauge Devices (12)

Instead of measuring the deformation of the wall of the borehole, the radial deformation of the surface of the flattened end of the hole

is measured. This enables overcoring to be carried out in the same hole without the expense of drilling a larger diameter (overcoring) hole.

Leeman has concluded for his experiment that the principal stresses in the rock surrounding the flattened end of the borehole are 1/1.53 of the principal stresses present at the end of the borehole. He also claims to have made successful measurements in a borehole to depths of around 200 feet. However, Bonnechere (2) has shown that due to the neglect of the stress acting parallel to the axis of the borehole (assumed to be one of the three principal stresses), very significant errors (100% or more) may be introduced. He suggests a value of 1.25, instead of 1.53, be used.

A.4 Hydraulic Jack Method (6)

Like those methods stated above, this method is also based on the measurement of changes of strain which is produced by a stress relieving technique using hydraulic jacks. Flat jacks as well as curved jacks have been used for this purpose.

Two plugs are cemented into the sidewalls of the excavation with a vertical distance X. Then a horizontal slot above the two plugs is cut into the rock which distresses the rock above the slot. The distance between the two plugs now becomes $X + \Delta X$. A flatjack is installed into the slot and pressure is applied until the distance between two plugs is again X. The pressure of the hydraulic fluid in the jack is the vertical compressive stress in the sidewall of the excavation.

We can only obtain the information about the magnitude of the stress acting normal to the plane of the flatjack by using flatjack.

It is not possible to use it to measure stresses at great distance inside the rock mass. Another method using curved jacks can obtain more information than the values from flatjacks. The curved jack technique(16) makes it possible to determine the stresses for greater distances inside the rock.

A.5 Hydraulic Fracturing (14)

Hydraulic fracturing is a procedure employed by the petroleum industry to enhance well production. Stress measurements are routinely made by adopting this technique even at great depths. Unlike the other techniques, it is not necessary to core the rock for instrumentation to determine the regional stresses.

The hydraulic fracturing is carried out by sealing the section of well with packers, at the places where the stresses of sidewall are to be measured (as in Fig. A.1), and applying the fluid pressure until the surrounding rock is fractured. The resulting stress in the wall of the well due to the injected fluid pressure is shown in Fig. A.2. It can be seen that for an applied pressure F at the ends of the packed-off section

$$\sigma_\theta = 0 \qquad \sigma_z = 0.94\ F \tag{1}$$

Along the central part of the section

$$\sigma_\theta = F \qquad \sigma_z = 0 \tag{2}$$

where σ_θ is the tangential stress

σ_z is the axial stress (stress parallel to the axis of the hole)

and $\sigma_r = -F$ (compression) is the radial stress which can be neglected

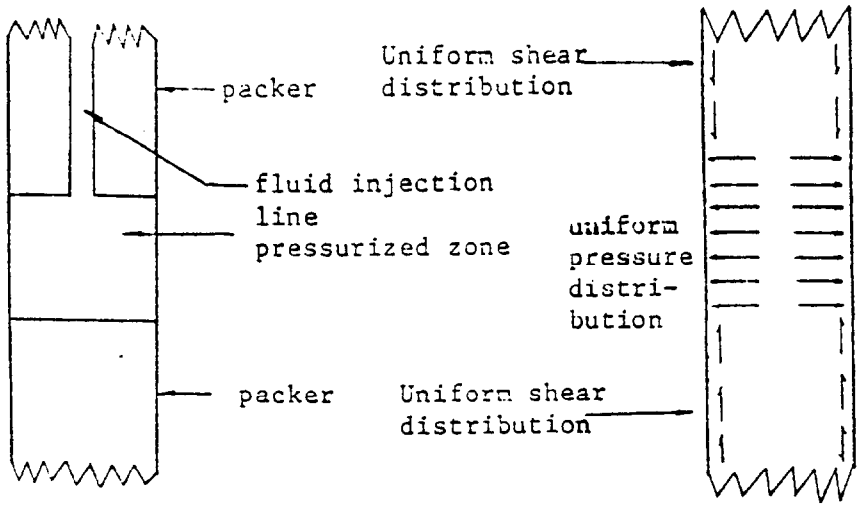

Fig. A.1 Schematic diagram of (a) Hydraulic fracture set-up (b) associated boundary stresses assumed by Kehle(10)

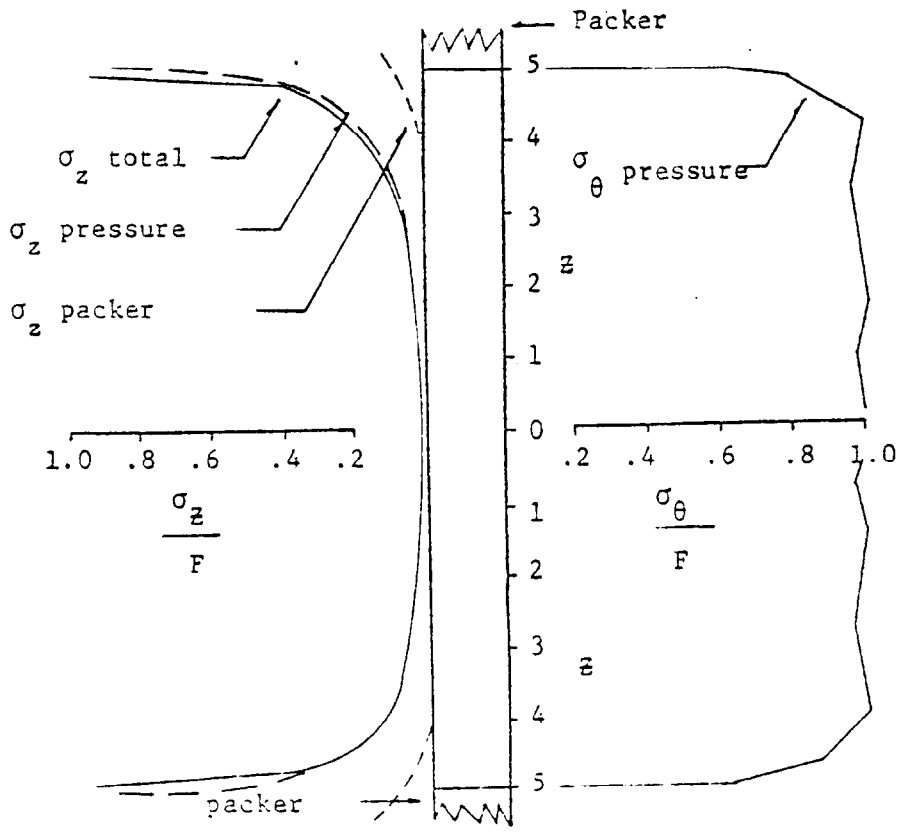

Figure A.2 Axial and tangential stresses induced at the wall of the hole due to stresses in Fig. A.1 (b)

since the well fracture is initiated in tension. (Mohr's tensile failure criterion is assumed to be valid here, namely, fracture will take place if the final tensile stress is greater than the tensile strength of the rock).

The preexisting state of stress on the wall of the well, due to the combined gravitational and tectonic stresses, can be assumed to be equivalent to that on the boundary of a hole in an infinite plate subjected to biaxial (plane) stress. This is true provided that the principal stresses are parallel and normal to the axis of the well. The state of stress around the hole can be determined and expressed in terms of three principal stresses based on this assumption. R is the vertical stress, P and Q (assuming P>Q) are the horizontal stresses.

Referring to Fig. A.3, the maximum value of the tangential stress $\sigma'_{\theta(max)}$ is[7]

$$\sigma'_{\theta(max)} = 3P - Q \qquad (3)$$

The axial stress due to field stresses is

$$\sigma'_z = R \qquad (4)$$

where R can be approximated for the overburden load, that is, $R = -\rho h$. The final maximum stress can be ascertained by superpositioning the stresses due to fluid pressure and field stresses, respectively. Thus, at the end of the packed-off section

$$\sigma_{\theta(total)} = 3P - Q$$
$$\sigma_{z(total)} = R + 0.94F \qquad (5)$$

along the central part of this section

$$\sigma_{\theta(total)} = 3P - Q + F$$
$$\sigma_{z(total)} = R \qquad (6)$$

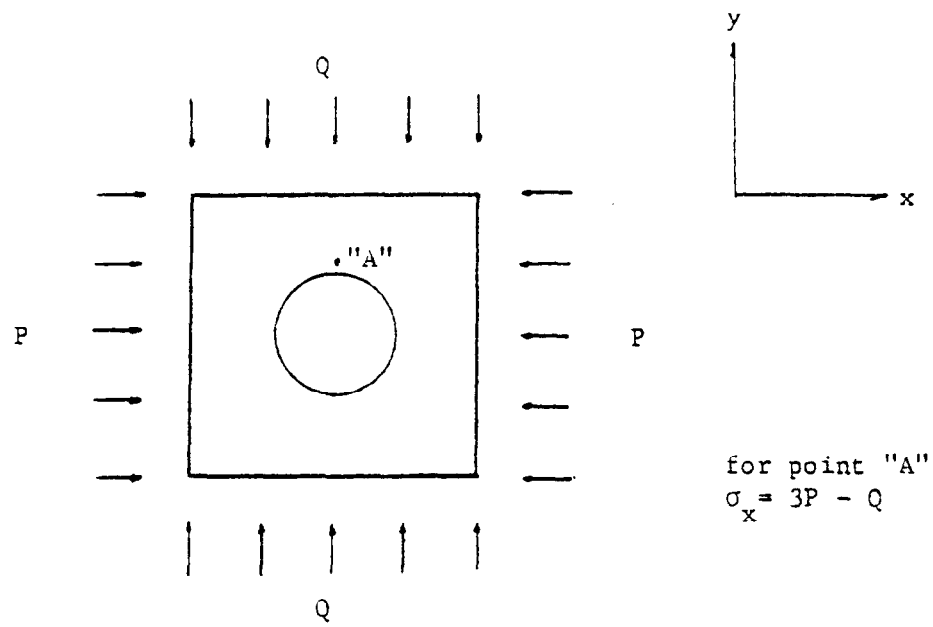

Fig. A.3 Stress concentration around a hole

In consideration of the effect of porewater pressure p_o, which increases the applied principal stresses and decreases the effective pressure in the packed-off section; P, Q, R, and F will be replaced by $P + p_o$, $Q + p_o$, $R + p_o$, and $F - p_o$ respectively in Eq. (5) and (6). By applying Mohr's tensile failure criterion, and superposition, we have two possible fracture conditions:

(a) The fracture will initiate in the central part of the packed-off section and propagate in the vertical plane, if

$$\sigma_{z(total)} = (R + p_o) + 0.94(F_c - p_o) < T_o$$

and (7)

$$\sigma_{\theta(total)} = 3(P + p_o) - (Q + p_o)\ (F_c - p_o) \geq T_o$$

(b) The fracture will initiate at the end and propagate in the horizontal plane, if

$$\sigma_{\theta(total)} = 3(P + p_o) - (Q + p_o) + (F_c - p_o) < T_o$$

$$\sigma_{z(total)} = (R + p_o) + 0.94(F_c - p_o) \geq T_o \qquad (8)$$

The pressure necessary to sustain propagation in the vertical plane remains

$$-p_s = P \tag{9}$$

and in the horizontal plane

$$-p_s = R \tag{10}$$

where F_c is the value of F at which the stress given by either Eq. (7) or (8) is greater than the tensile strength of the rock T_o, and p_s is referred to as the shut-in pressure.

A certain range of the principal stresses can now be determined from well fracturing data (F_c, p_o, p_s, T_o, ρ, h) that satisfy the following conditions:

(1) if $0.94(F_c - p_o) < |R + p_o| + T_o$ and $p_s < |R|$

the fracture should initiate in the central part and propagate in a vertical plane, where

$$R = -\rho h$$

$$P = -p_s$$

$$Q = 3P + p_o + F_c - T_o$$

$$\text{or } Q = -3p_s + p_o + F_c - T_o$$

(2) If $0.94(F_c - p_o) > |R + p_o| + T_o$ and $p_s > |R|$

the fracture will initiate at the end and propagate in a horizontal plane.

(3) If $0.94(F_c - p_o) > |R + p_o| + T_o$ and $p_s > |R|$

the fracture will initiate in a horizontal plane at the end and the final fracture will be vertical.

Since the position and orientation of the fracture in the hole can be observed by a borehole TV camera, it is easy to decide the criteria (1,2 & 3 given above) that governs the failure.

Besides its applicability at great depths, this method has another advantage, namely, that it is not necessary to know any mechanical properties of the rock which do not appear in the above analysis.

A.6 Miscellaneous Methods

A number of other methods have been used to ascertain the information about in-situ stresses. Some such methods are the photostress method, the sonic method, the sensitivity method, core discing method, static equilibrium method, and a kind of method based on the changes in density in the rock produced by corresponding changes in stress. These methods are not fully developed. Yet the validity of these for a particular situation or as a supplement to other methods can not be dismissed.

APPENDIX B CORE DRILLING PROCESS

A general idea of core drilling process can be obtained from the operation of Christensen Rubber Sleeve Core Barrel: (Fig. B.1). The barrel is rotated by the rotary table. The source of weight for cutting the core is provided by the circulating fluid which exerts pressure on the nozzlehole (E). Weight is controlled by the flowrate and the number and size of nozzles open in the nozzle plate.

Barrel is advanced to the bottom and the fluid is circulated to condition mud. Expansion joint (A) is held in an extended position by the stripper tube latch (B). This latch also restricts the stripper tube (G) from any upward movement. The stripper tube is prevented from moving down through the barrel by the lower stripper tube ratchet spring (F). This spring works on the same principle as does a core spring. Any downward movement of the tube causes the constriction of the spring.

The stripper tube release plug (J) has been dropped through the drill string to its seat in the top of the stripper tube (G). The barrel has been set on bottom and the expansion joint (A) is collapsed until it shoulders on the top sub (D), a distance of two feet. As coring commences, the upper stripper tube ratchet spring (C) holds the tube and prevents its downward movement. As the lower barrel advances into the formation, it releases the tension of the lower ratchet spring (F) and carries it down the stripper tube.

Two feet of core is usually cut and the expansion joint (A) is again extended. Notice that rubber sleeve (H) and the core (I) being held by the stripper tube (G) have entered the core barrel.

The expansion joint may again be collapsed, but the lower stripper ratchet spring (F) will again prevent downward movement of the tube while the upper ratchet spring (C) is carried down with the expansion joint.

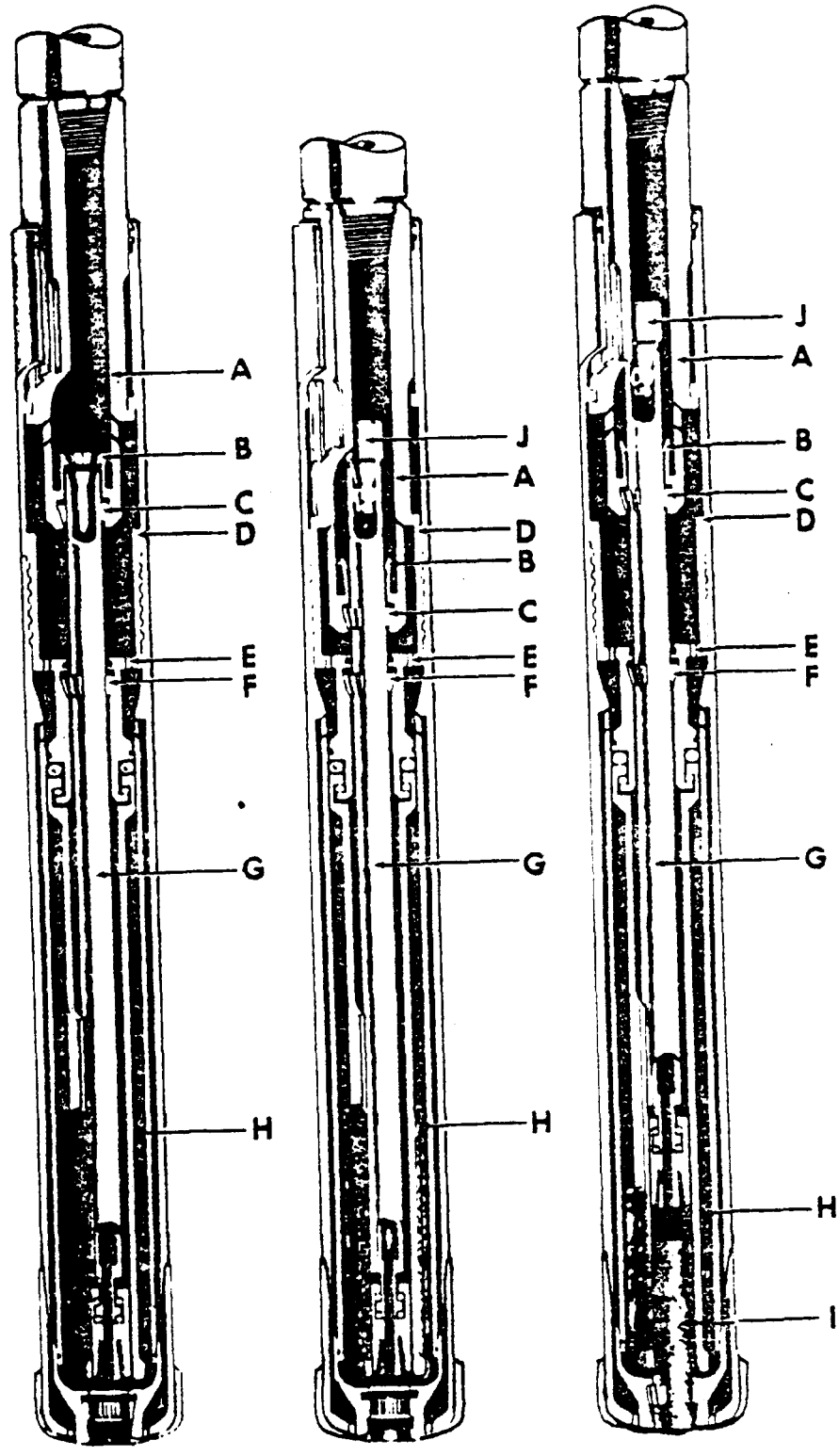

A B C

Figure B-1

Coring Process of Rubber Sleeve Core Barrel